Titre: Title:	Fabrication of Arrays of Ferromagnetic Multilayer Nanowires in Alumina Templates and Modelling the Magnetic Anisotropy Using Effective Field Model
Auteur: Author:	Mehran Yazdizadeh
Date:	2020
Type:	Mémoire ou thèse / Dissertation or Thesis
Référence: Citation:	Yazdizadeh, M. (2020). Fabrication of Arrays of Ferromagnetic Multilayer Nanowires in Alumina Templates and Modelling the Magnetic Anisotropy Using Effective Field Model [Ph.D. thesis, Polytechnique Montréal]. PolyPublie. https://publications.polymtl.ca/5491/

POLYTECHNIQUE MONTRÉAL
affiliée à l'Université de Montréal

Fabrication of arrays of ferromagnetic multilayer nanowires in alumina templates and modelling the magnetic anisotropy using effective field model

MEHRAN YAZDIZADEH
Département de génie physique

Thèse présentée en vue de l'obtention du diplôme de *Philosophiæ Doctor*
Génie physique

août 2020

POLYTECHNIQUE MONTRÉAL
affiliée à l'Université de Montréal

Cette thèse intitulée :

Fabrication of arrays of ferromagnetic multilayer nanowires in alumina templates and modelling the magnetic anisotropy using effective field model

présentée par **Mehran YAZDIZADEH**
en vue de l'obtention du diplôme de *Philosophiæ Doctor*
a été dûment acceptée par le jury d'examen constitué de :

Clara SANTATO, présidente
Arthur YELON, membre et directeur de recherche
David MÉNARD, membre et codirecteur de recherche
Frédéric SIROIS, membre
Fanny BÉRON , membre externe

To whom it may concern

ACKNOWLEDGMENT

I am so thankful to my supervisors, Prof. Arthur Yelon and Prof. David Ménard who have supported me in this journey. They have provided me the best possible research environment during my research career at Polytechnique de Montreal.
I am thankful to all my office mates including Dr. Amir Roohi Noozadi, Dr. Nima Nateghi and Nicolas Teyssedou. In particular, I am very thankful to Dr. Antoin Morin who has co-operate me in FMR and VSM measurement while I was away from the lab and performed careful and through measurement and data analysis of my fabricated samples.
I thank Dr. Aref Pourzadi for helpful discussions on simulations in MATLAB.
I am very thankful to Dr. Louis-Philippe Carignan for helpful discussions and suggestions specially at the beginning of my research while I had a hard time to keep my research on track and use some sophisticated instrument in our labs.
I am very thankful to Dr. Jonathan Bellemare for the time he spent to train me in many steps of the fabrications and for helpful discussions.
My special thanks to Dr. Omid Salehzadeh who performed many measurements on my samples including Zygo and Auger spectroscopy as well as tons of constructive discussions about fabrication process.
My most special thanks to my dear wife, Bahar Ehsani, who was with me in tough times.

RÉSUMÉ

Les réseaux de nanofils magnétiques suscitent beaucoup d'intérêt pour un large éventail d'applications, incluant les milieux d'enregistrement magnétique haute densité, les cristaux magnoniques et les capteurs magnéto-résistifs. Parmi les exigences de base pour un déploiement commercial de ces nouveaux matériaux, on retrouve la facilité et les faibles coûts de fabrication, la reproductibilité des propriétés physiques et des caractéristiques magnétiques ajustables telles que la coercivité, anisotropie et la stabilité thermique.

Dans des études précédentes, un modèle de champ équivalent basé sur une approche de champ moyen pur a été développé pour décrire l'anisotropie magnétique de systèmes constitués de réseaux de nanofils magnétiques multicouches. Cependant, ce modèle n'était pas toujours en accord avec l'expérience, en raison d'une simplification excessive de l'interaction dipolaire entre les couches magnétiques, ainsi que des imperfections dans les échantillons, notamment du mauvais contrôle de l'épaisseur des couches de nanofils multicouches et de la pureté chimique de chaque couche. De plus, le l'estimation de la porosité des matrices nanoporeuses manquait de précision, causant des erreurs dans la prédiction du modèle de l'anisotropie. Ces problèmes sont particulièrement marqués pour les géométries spécifiques de nanofils multicouches, dans lesquelles les couches magnétiques sont rapprochés les unes des autres, produisant des interactions dipolaires inhomogènes.

Dans cette thèse, nous abordons d'abord les problèmes liés à la fabrication des échantillons. Nous avons proposé une méthode coulométrique, afin d'améliorer notre contrôle sur l'épaisseur des couche lors de la fabrication. Nous avons également atteint une pureté relativement plus élevée dans nos échantillons en ajustant la quantité de matériau non magnétique dans la solution électrolytique pour l'électrodéposition des couches. Aussi, une nouvelle méthode a été proposée pour mesurer la porosité effective de l'alumine nanoporeuse utilisée comme matrice pour l'électrodéposition. Enfin, une approche systématique a été proposée afin d'améliorer la régularité des pores dans les matrices d'alumine, une exigence importante pour certaines applications. Nous avons ensuite considéré les limites du modèle de champ moyen. Un nouveau modèle a été développé pour mieux prédire la champ d'anisotropie, en moyennant l'interaction dipolaire exacte des disques magnétiques jusqu'à 5 disques voisins dans un fil multicouche.

Un prétraitement de l'alumine par électropolissage est nécessaire avant le processus d'anodisation. Afin de mesurer quantitativement la rugosité de surface de l'alumine électropolie et montrer la corrélation entre la rugosité de surface et la régularité des pores, nous avons collecté les données de rugosité de surface à l'aide d'un microscope optique appelé Zygo. Ces données ont été traitées à l'aide d'une analyse statistique dite de passage à niveau (level

crossing ou LC), qui de quantifier la rugosité de la surface. L'aluminium électropoli a ensuite été anodisé sous divers tensions, températures et durées. Une méthode de traitement d'image a également été développée pour quantifier la régularité des pores de matrices d'alumine anodiques nanoporeuses. Grâce à cette méthode de traitement originale, nous avons pu améliorer les paramètres expérimentaux pour obtenir des pores mieux ordonnés et de façon plus reproductibles pour les membranes d'oxyde d'aluminium anodique (AAO). Un côté des membranes a par la suite été plaqué d'une mince couche d'or déposée par évaporation. Comme nous l'expliquons au chapitre 2, la technique est appliquée de façon à minimiser la diffusion de l'or dans les pores. Une couche ultra-mince de titane a également été plaquée avant l'évaporation de l'or pour améliorer l'adhésivité.

La membrane plaquée a été utilisée par la suite comme électrode dans un bain d'électrolytes magnétiques et non magnétiques des matériaux à déposer. Des tensions alternatives ont été appliquées pour l'électrodéposition alternative de matériaux magnétiques et non magnétiques, puisque la tension d'électrodéposition pour chaque métal est différente. Au cours de ce processus, les ions du métal noble (qui est Cu dans ce cas) ont été dilués autant que possible, afin d'éviter le co-dépôt pendant le dépôt des couches du métal ferromagnétique moins noble. La coulométrie a été utilisée afin de contrôler l'épaisseur des matériaux déposés en comptant les électrons pendant le processus de dépôt. Enfin, la spectroscopie électronique Auger a été utilisée pour effectuer l'analyse chimique de nanofils individuels. Encore une fois, nous avons constaté une amélioration notable dans la pureté de chaque couche bien que certaines impuretés soient encore présentes, surtout dans les couches magnétiques.

Un modèle de champ moyen a été utilisé pour prédire le champ effectif d'anisotropie magnétique. Étant donné que l'approche usuelle du champ moyen ne parvient pas à expliquer le champ équivalent de certains échantillons, dans lesquels la couche non magnétique d'espacement est mince, nous avons considéré la contribution exacte du champ dipolaire des couches voisines, jusqu'à cinq voisins. Il s'agit d'un facteur important pour déterminer l'énergie libre totale dans chaque disque magnétique. Cela a été fait en calculant numériquement la contribution de l'interaction dipôle-dipôle pour les disques magnétiques voisins en supposant les échantillons possèdent une configuration magnétique rigide. Le champ effectif a ensuite été mesuré expérimentalement par des techniques de résonance ferromagnétique (FMR) et de magnétométrie d'échantillons vibrants (VSM). Bien que les prédictions du modèle ne montrent pas un accord parfait avec les données, elles démontrent néanmoins une amélioration significative. À ce stade, nous ne sommes pas certains que l'écart soit dû à l'imperfection des échantillons ou à la simplification du modèle ou une combinaison des deux. Cependant, certains facteurs, comme l'ignorance des différentes distributions de longueurs de nanofils lors de l'électrodéposition, l'omission de fils manquants dans certains pores, les couches d'épaisseur

non uniformes sont toutes des sources possibles de divergence.

ABSTRACT

Arrays of magnetic nanowires have gained significant interest for a broad range of applications, including high density magnetic storage media, magnonic crystals and magnetoresistive sensors. Basic requirements for successful commercial deployments are ease of manufacturing, low cost, reproducibility and superior magnetic properties such as coercivity, anisotropy and thermal stability.

In previous studies, an effective field model based on a pure mean field approach was developed to describe the magnetic anisotropy of a system of arrays of magnetic nanowires. However, this model was not in agreement with experiment due to over simplification of dipolar interaction between magnetic layers as well as imperfections in samples, namely poor control over layer thickness of multilayer nanowires and purity of each layer. Moreover, the estimation of porosity was not precise causing more error in model prediction of anisotropy field. These issues are more serious for specific geometries of multilayer nanowires where the magnetic disks are close to each other and their dipolar interaction can not be assumed to be homogeneous.

Here, we first address the issues related to samples. We proposed a so called Coulometry method to have more control over layer thickness. We also achieved relatively higher purity in our samples by adjusting the amount of non-magnetic material inside the electolyte bath before electrodeposition. A new method was also proposed to measure the effective porosity of the porous alumina which is used as a template for electrodeposition. A systematic process is also proposed in order to improve the pore regularity in alumina templates which is necessary in some applications. Finally, a new model was developed to better predict the anisotropy field by considering the exact dipolar interaction of magnetic disks up to 5 nearest neighbor disks within a wire.

Preprocessing of the alumina i.e. electropolishing is necessary before the anodization process. In order to quantitatively measure the surface roughness of electropolished alumina and show the correlation between surface roughness and pore regularity, we have collected the surface roughness data using an optical microscope called Zygo. The surface data was then processed using a so called Level Crossing (LC) statistical analysis in order to assign a number to the surface roughness. The electropolished aluminum was then anodized under various voltages, temperatures and time lengths. An Image processing method was then developed to quantitatively measure the pore regularity of porous anodic alumina. Using this image processing method originally developed by our research team, we were able to optimize the experimental operational conditions to get the best possible pore ordering and reproducibility

in our membrane fabrication of anodic aluminum oxide (AAO). The membrane was then gold plated at the bottom using metal evaporation technique. This technique, as we explain in chapter 2, will make sure the gold diffusion into pores are minimized. A very thin titanium was also plated prior to gold evaporation to enhance the adhesiveness. Then the AAO membrane was used as working electrode in a bath of magnetic and nonmagnetic electrolytes of all the materials we wanted to deposit. Alternating voltages were applied to electrodeposit magnetic and nonmagnetic materials since the electrodeposition voltage for each metal is different. During this process the noble metal (which is Cu in this case) was kept as dilute as possible to avoid co-deposition while the less noble metal is being deposited. Coulometry was used in order to control the thickness of deposited materials by counting the transferred electrons during the deposition process. Finally, Auger electron spectroscopy was used to perform the chemical analysis of our samples. Again, one can notice an huge improvement in our fabrication results regarding the purity of each layer although some impurities still were observe especially in the magnetic layers.

The mean field model was used to predict the effective field, and thus the magnetic anisotropy. Since the standard mean field approach fails to explain the effective field in samples in which the nonmagnetic (spacer) layer is thin, we have considered the exact contribution of dipolar interaction of the first five nearest neighbours, since this is the leading factor to determine the total free energy in each magnetic disk. This was done by numerically calculating the contribution of dipole-dipole interaction for neighbouring magnetic disks assuming the samples follows the rigid magnetization model. The effective field was then experimentally measured using Ferromagnetic Resonance (FMR) and Vibrating Sample Magnetometry (VSM) techniques. Although our model predictions do not show a perfect agreement with the experimental data, they exhibit a significant improvement. At this point we are not certain that whether the discrepancy is due to imperfection of samples or the simplification of model or both. However, some possible reasons, such as ignoring the various length distributions of nanowires during the electrodeposition, missing wires in some pores, non uniform layer thickness are discussed as possible sources of discrepancies.

TABLE OF CONTENTS

LIST OF TABLES

LIST OF FIGURES

LIST OF ACRONYMS AND SYMBOLS

Symbols

$2a$	wire (pore) diameter
$\boldsymbol{A}$	exchange constant
A	exchange stiffness
$\mathcal{A}$	area of deposition
α	size of steps in level crossing analysis
$\mathbf{B}$	magnetic field
γ	gyromagnetic ratio
d	thickness
D_{sw}	spin-wave stiffness
ϵ_{tot}	total free energy
ϵ_a	magneto crystalline anisotropy energy
ϵ_d	demagnetizing energy
ϵ_{ms}	magnetostriction energy
ϵ_{stress}	applied stress energy
ϵ_{ex}	exchange interaction energy
E	electric potential
E°	reduction potential vs standard hydrogen electrode
f	filling factor
F	Faraday constant
g	Landé factor
h_m	thickness of magnetic disk
h_n	thickness of non-magnetic disk
h	$= h_m + h_n$
$\hbar$	reduced Planck
H	height of the first peak in FFT
H_d	demagnetizing field
H_{eff}	effective field
K	anisotropy constant
M	magnetization
$\mathcal{M}$	molar mass
m	magnetic moment
M_s	saturation magnetization

μ_0	vacuum permeability
μ_B	Bohr magneton
n_α^+	number of upcrossings
n	number of pores
N	total number of data points in a signal
N_d	demagnetizing factor
N_α^+	ensemble average of upcrossings in level crossing analysis
ν_α^+	average frequency of positive upcrossings in level crossing analysis
N_{tot}^+	total number of upcrossings
$\overline{N}$	dipolar interaction tensor
$\overline{N}_d$	demagnetizing tensor
$\overline{N}$	total demagnetizing tensor
N_{ip}	in-plane shape demagnetization factor
N_{oop}	out-of-plane shape demagnetizing factor
$\overline{N}_{inter}$	interwire shape demagnetizing factor
$\overline{N}_{intra}$	intrawire shape demagnetizing factor
P	porosity
Q	total charge
$\mathcal{R}$	resolution of a signal
R	regularity ratio
ρ	density
$\vec{S}$	spin
S	surface area
θ_H	direction of applied field
Θ	size of the signal
U	dipolar energy density
V	volume
W	full width at half maximum
ω_0	angular frequency
Z	number of electrons

Abreviations

AAO	anodic aluminum oxide
FORC	first order reversal curve
FFT	fast Fourier transform
FMR	ferromagnetic resonance

IP	in plane
LCA	level crossing analysis
LC	level crossing
MF	mean field
MRAM	magnetic random access memory
NN	nearest neighbor
1-x NN	first x nearest neighbors
OOP	out of plane
OOMMF	object oriented micro magnetic framework
PAA	porous anodic alumina
SEM	scanning electron microscopy
TEM	transmission electron microscopy
VSM	vibrating sample magnetometer

LIST OF APPENDICES

CHAPTER 1 INTRODUCTION

Owing to their small dimensions, nano materials exhibit properties different from those of their bulk counterparts (Sun *et al.*, 2005; Béron *et al.*, 2010). Magnetic nanowires offer more degrees of freedom for manipulating their magnetic properties in comparison with bulk magnetic materials. As an example, one can adjust the magnetic anisotropy of magnetic nanowires via tailoring their aspect ratio (Yang *et al.*, 2000). Further, engineering the thickness ratio of the magnetic to non-magnetic layers in multilayer nanowires provides another degree of freedom to tune their magnetic properties (Fert and Piraux, 1999; Peng *et al.*, 2007; Tang *et al.*, 2007).

To fully exploit these nanostructures as, for example, magnetic metamaterials or magnonic crystals, we must be able to perfectly control their geometrical parameters. However, the precise control of layer thicknesses and stochiometry within the wires or the regular distribution of pores in the alumina matrix remains a challenge to this day. Also, the methods used to characterize regularity of the pore distribution have their limits. Finally, the mean field model, used to predict its effective magnetic anisotropy, is not fully justified for some sets of parameters.

In this thesis we explore some characterization tools and fabrication techniques to improve the quality of arrays of multilayer nanowires and refine the mean field model to better predictability of their magnetic properties.

1.1 Preliminary definitions

Before we proceed, let us illustrate and describe some terms frequently used. Figure 1.1 (a) shows a schematic view of an array of multilayer nanowire system. Figure 1.1 (b) shows some of the most important geometrical parameters of these systems. A typical range for nanowire diameter, $2a$, is 30 to 250 nm and for interpore distance, D_p, is 60 to 300. Magnetic thickness, h_m, and non-magnetic thickness, h_{nm} are usually between 5 to 200 nm. Layer thickness, as shown in this figure, is the thickness of each magnetic or non-magnetic layer within a wire.

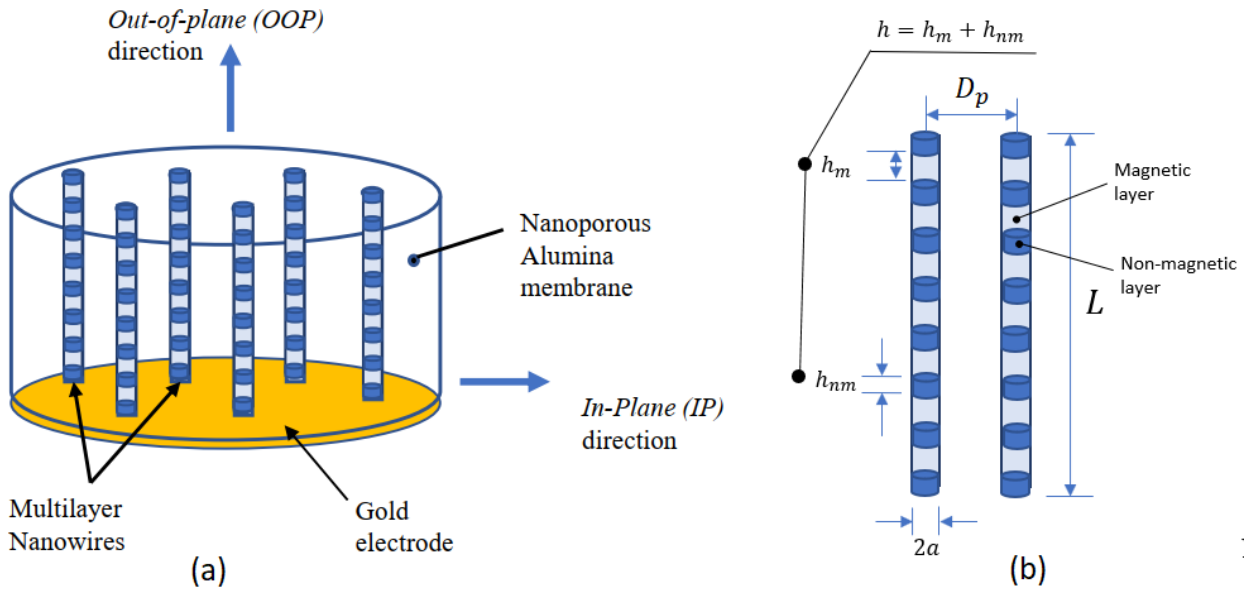

Figure 1.1 (a) Schematic view on an array of multilayer nanowire. (b) D_p is the distance between two adjacent wires, h_m is the thickness of magnetic layer, h_{nm} is the thickness of non-magnetic layer, $2a$ is the wire diameter.

Another term which is used frequently is the porosity. Essentially the porosity (or effective porosity as we will see in chapter 3) is the ratio of area of deposition to total area of the sample. The reason we call it effective porosity is that if there is a pore which has not been filled by any material is not considered as part of area of deposition. Fig. 1.2 demonstrate this concept.

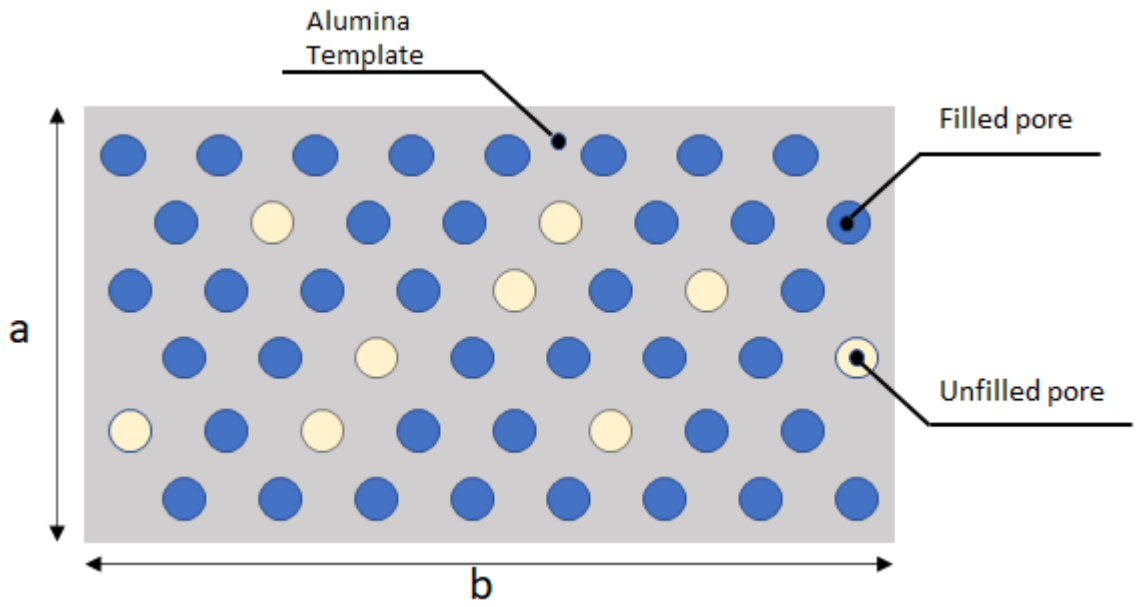

Figure 1.2 Effective porosity is defined as the ratio of sum of the area of the filled pores (blue pores) to the total area that is $a \times b$.

Regularity ratio is another term which is used frequently in this thesis. This term generally defines how the pores match the hexagonality pattern. In particular, we label a pore as "ordered" if there are 6 pores around if within a specific range of distance and angle. Regularity ratio is then defined as the number of ordered pores to the total number of pores.
When we deposit magnetic and non-magnetic materials layer by layer into the template, some non-magnetic material co-deposits with magnetic material. This creates impurity in our magnetic materials. By purity, we mostly refer to the matching of the stochiometry of the deposited layers with the expected ones which is not perfect due to impurities caused by non-magnetic material.
Last, when we talk about "nearest neighbor", we refer to the nearest neighbor magnetic layers above and below a specific magnetic layer. A schematic view of nears neighbors is presented in Fig.1.3.

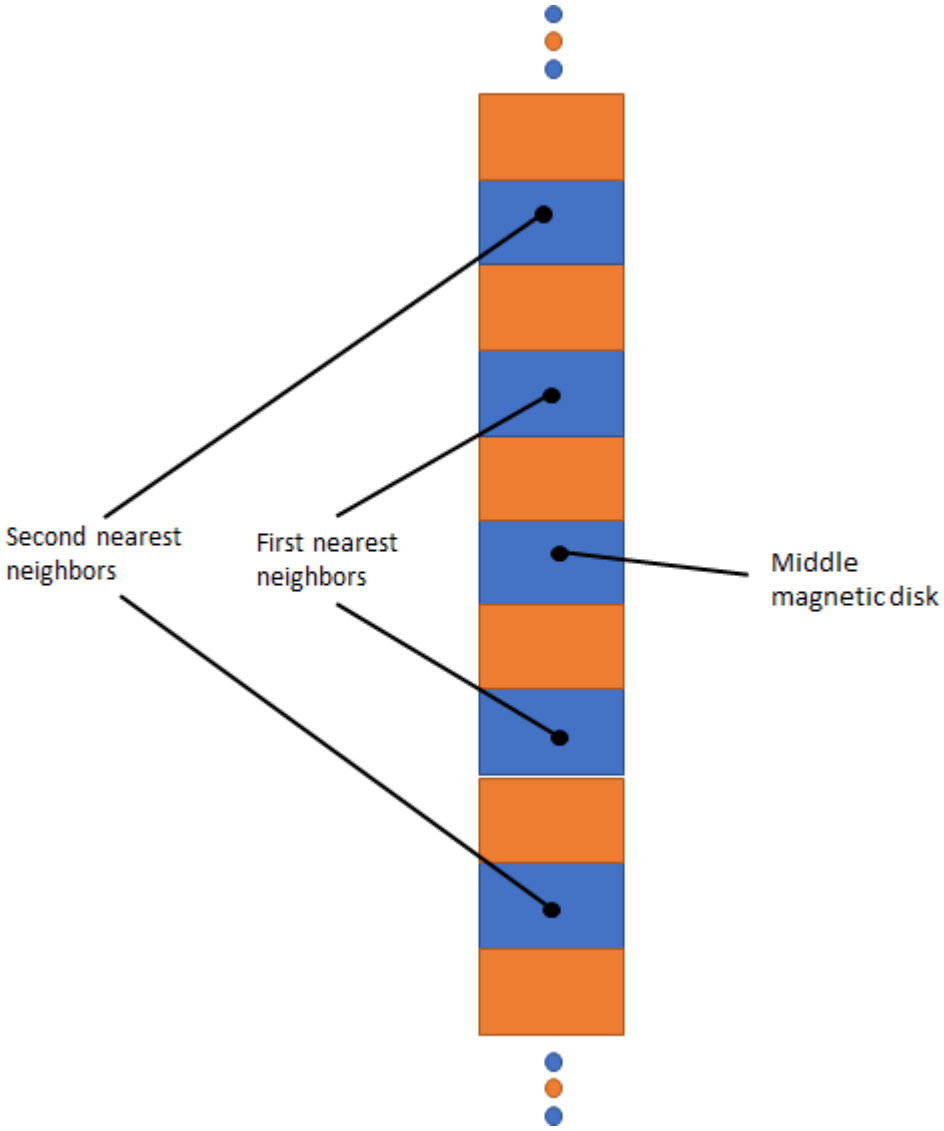

Figure 1.3 Definition of nearest neighbors magnetic disks. Blue disks represent magnetic layers and orange disks represent non-magnetic layers.

1.2 Arrays of multilayer ferromagnetic nanowires

Here, we briefly review the studies which has been done previously related to the subject of this thesis with a short report of their results. Further specific reviews will be presented at the beginning of each chapters.

Ordered arrays of ferromagnetic nanowires are particularly interesting due to their potential applications in magnetic random access memories (MRAM), recording media and magnetic sensors (Piraux *et al.*, 1994; Cowburn and Welland, 2000; Chou, 1997; Nordquist *et al.*, 1997).

There are two major approaches to fabricate magnetic nanowires : top-down, and bottom-up methods (Biswas *et al.*, 2012). In the top-down methods, the base material is first grown on a template-free substrate. Then, a technique such as lithography is used to pattern the sample and etch it to form the desired structure. In the bottom-up method, the deposition happens inside the nano-holes pre-patterned on a template.
Using the bottom-up method to fabricate arrays of magnetic multilayer nanowires requires good control over the fabrication of the template and the deposition process. The deposition process must be fine-tuned to alternately deposit the ferromagnetic and nonmagnetic layers into the pores, without any unwanted incorporation of non-magnetic materials into the magnetic layers or vice-versa.
Anodic aluminum oxide (AAO) is one of the most widely used templates, due to the simple fabrication process and the ability to provide a geometric structure with good flexibility. AAO is capable of providing an extremely high aspect ratio, which is impossible to achieve employing other methods such as track etched membrane or lithography. One of the challenges with AAOs however, is the reproducibility of the pore regularity when compared to other methods such as lithography.

AAO attracted increased attention since 1995, after Masuda and Fukuda introduced the so called "two-step anodization" method (Masuda and Fukuda, 1995).This method enables us to fabricate highly ordered porous templates with very high aspect ratios, introducing new opportunities in nano technology. They first anodize the aluminum by applying a voltage in an acidic electrolyte which produces porous anodic alumina. These initial pores are randomly distributed on the surface, and slowly move into order as they grow deeper. Then, they remove the top anodized layer, leaving behind ordered pores with concave shape on the surface. Then, they perform the second anodization step to achieve the required depth, starting with the ordered shallow concave ordered pattern from the first step.
The problem, however, is that the pore regularity is not sustainable and reproducible employing this method. Regularity is of great importance in many applications such as magnetic recording media and magnonic crystals.
Electrodeposition (electroplating) is the most widely used method to alternately deposit the ferromagnetic and non-magnetic layers into the pores. Although electrodeposition is relatively simple, inexpensive and flexible, it has several limitations. For example, achieving an accurate and uniform layer thickness along the nanowire is challenging. Another issue is the ability to achieve high purity in magnetic layers. The impurities in the magnetic layers is typically caused by the co-deposition of the non-magnetic species used to form the spacer layers, such as copper layers.

In multilayer nanowires, the magnetic properties strongly depends on magnetic anisotropy. Sun *et al.* showed that in high aspect ratio structures, the easy axis, which shows the direction in which a relatively small applied field can saturate the magnetization, will align perpendicular to the magnetic layers (along the wire direction) (Sun *et al.*, 2005). However, this is not the only factor which controls the anisotropy. In fact, the thickness of non-magnetic layers plays an important role as well, as reported by Chen *et al.* (Chen *et al.*, 2006).
In the mean field model developed here, a rigid magnetization state is assumed. Basically, we have assumed that all dipoles are parallel to each other in all stages of the experiment. In order to justify this assumption in our model, we have applied a high enough external field during the ferromagnetic resonance (FMR) measurements to guarantee that the rigid magnetization assumption is reasonably valid. Co, Fe and Ni are frequently used for fabrication of multilayered nanowires. Here we have mainly used Ni.

Previous studies at the Laboratoire de magnétisme

Extensive research has been carried out on magnetic nanowires to understand and engineer their magnetic properties. In the following, a brief review is presented of the results obtained in the previous studies, relevant to this work. These include the first-order reversal curve (FORC) method, electron holography and effective field model. A brief review of the work by Bellemare *et al.* (2014) on the fabrication of alumina template is also presented.

Béron *et al.*(2007) used the FORC method to study the magnetic behavior of arrays of Ni/Cu multilayer nanowires. They were able to shed light on the magnetic properties of magnetic disks in an individual nanowire. They have reported that as the thickness ratio of Cu to Ni layer increases, there is a cross-over in the out of plane (OOP) direction from the easy axis to the hard axis (Béron *et al.*, 2008). Béron *et al.* showed that FORC can be used to estimate the length distribution of the nanowires in a sample (Béron *et al.*, 2006). Information regarding the length distribution can help to improve the predictions of the effective field model.

Akhtari-Zavareh *et al.*(2014) conducted extensive electron holography studies to determine the local magnetic behavior of individual CoFeB/Cu multilayer nanowires. They concluded that the magnetic behavior of an individual nanowire depends strongly upon the ratio of the magnetic to non-magnetic layer thicknesses, in agreement with the results reported by Béron *et al.* using the FORC method as discussed above. A notable conclusion in their study was that the layer thicknesses of the individual nanowires were significantly different from the va-

lues expected from the fabrication parameters and the expected growth rate of the nanowires with a uniform composition. Also, a significant amount of Cu was found in the magnetic layers (up to 50%) making their chemical composition far from ideal. They also predicted the presence of magnetic vortices at the ends of the nanowires. As discussed in chapter 3, we have developed a model using the object oriented micro magnetic framework (OOMMF), (Donahue, 1999) which correctly predicts the presence of magnetic vortices. Here, we have adopted Coulometry method to address the layer thickness issue. In this method, we count the number of charges deposited for each material so we can control the thickness of deposited material as we grow the nanowires. Once a desired amount of charge is deposited for one layer, we terminate the deposition for that specific material and start depositing the other material for the next layer. Repeating this process, we can achieve multilayer nanowires with desired thickness for each layer. Also we have estimated the required amount of Cu for the entire sample so that we can optimally dilute the electrolyte bath to minimize the co-deposition of Cu into Ni.

Carignan *et al.* (2007) made a significant contribution in understanding the behavior of magnetic nanowires, and in correlating their findings with the fabrication process and the design parameters. They conducted extensive research to understand the magnetic anisotropy in arrays of Ni, CoFeB and Ni/Cu nanowires , via developing an effective field model. They showed that the effective field can be estimated via a mean field method by calculating the effective demagnetizing factor. It depends upon the geometry of the system, namely the porosity and the thickness ratio of the magnetic to non-magnetic layers (also see Encinas-Oropesa *et al.*, 2001). They also showed that the effective field is a function of the magnetic to non-magnetic layer thickness ratio in agreement with the results reported by Béron *et al.* and Akhtari-Zavareh *et al.* as discussed above.

Therefore, one could engineer the thickness ratio of magnetic to non-magnetic layers to control the effective anisotropy field, which in turn could control the magnetic response of the system (also see Sun *et al.*, 2005). However, due to simplification in the model, it failed in the case where the non-magnetic (spacer) layer was quite thin because in this case the dipolar interaction between nearest neighbor magnetic layers are not quite homogeneous so a pure mean field is not a good estimation. These issues are addressed in detail in this thesis. We adopted the approach firs introduced by Ogouchi (Oguchi, 1955) to deal with nearest neighbor interactions. We calculate the exact dipolar interaction for the nearest neighbor magnetic layers and then treat the rest of the array with mean field model. the predictions will better match the experimental results ; however, there are still opportunities to reduce the discrepancy between the model and the experimental results by better understanding and controlling the fabrication process. In other words, one must make sure that the parameters being fed into

the model are not distorted by the imperfections introduced by the fabrication process.

During the fabrication of a porous anodic alumina (PAA) membrane, the anodization process results in the formation of a thin barrier oxide layer at the bottom of the pores (Lillo and Losic, 2009). The electrodeposition process requires the removal of this thin layer to create a through-hole membrane. However, any effort to remove this barrier layer, through a wet etch process, will also etch the pores and will disturb the size distribution of the pores. Bellemare *et al.* have conducted extensive research on the fabrication of the alumina template, and have developed a method to calculate the optimal experimental conditions to etch the oxide barrier layer (Bellemare *et al.*, 2015). The method proposed by Bellemare *et al.* provides more control over the fabrication of alumina templates. In this method, they applied a decreasing step voltage at the end of the anodization process, leading to the formation of pore branches at the bottom of the major pores. This, in turn, increased the surface exposed to the etch solution, accelerating the etch rate of the oxide barrier. The increase of the etch rate at the bottom of the pores is expected to reduce the destructive effects of the removal of the barrier layer. Here we have adopted a different approach which eliminates the need of removing the barrier layer. In another publication (Bellemare *et al.*, 2014), Bellemare *et al.* have investigated the optimum voltage as a function of the acid concentration in order to improve the pore ordering of the fabricated porous alumina. They concluded that for a given acid concentration, there is a burning point. Beyond that voltage the aluminum will burn during the anodization process. They showed that the best results were achieved just below this burning voltage. We have developed a quantitative method to determine the pore regularity. This method is based on an image processing algorithm in which we systematically detect the hexagonal patterns in pores and then calculate the regularity of pores. We have considered, not only the optimum voltage, but also the acid temperature and the time duration of the anodization process to achieve better pore regularity. We have also studied the correlation of the surface roughness with pore regularity(Yazdizadeh *et al.*, 2020). To our knowledge, this has not been addressed in any previous research.

1.3 Objectives and organization of the thesis

Objectives

The topic of electrodeposition of magnetic nanowires in alumina templates and their properties is not a new subject. However, some aspects of these systems regarding their fabrication process and analysis are still not fully under control or understood. In this thesis, our objec-

tive is to push some of these challenges and limitations. Figure 1.4 illustrates the challenges that we are trying to address in this thesis. As shown in this figure, we have classified these challenges into two main categories : Fabrication and Modeling.

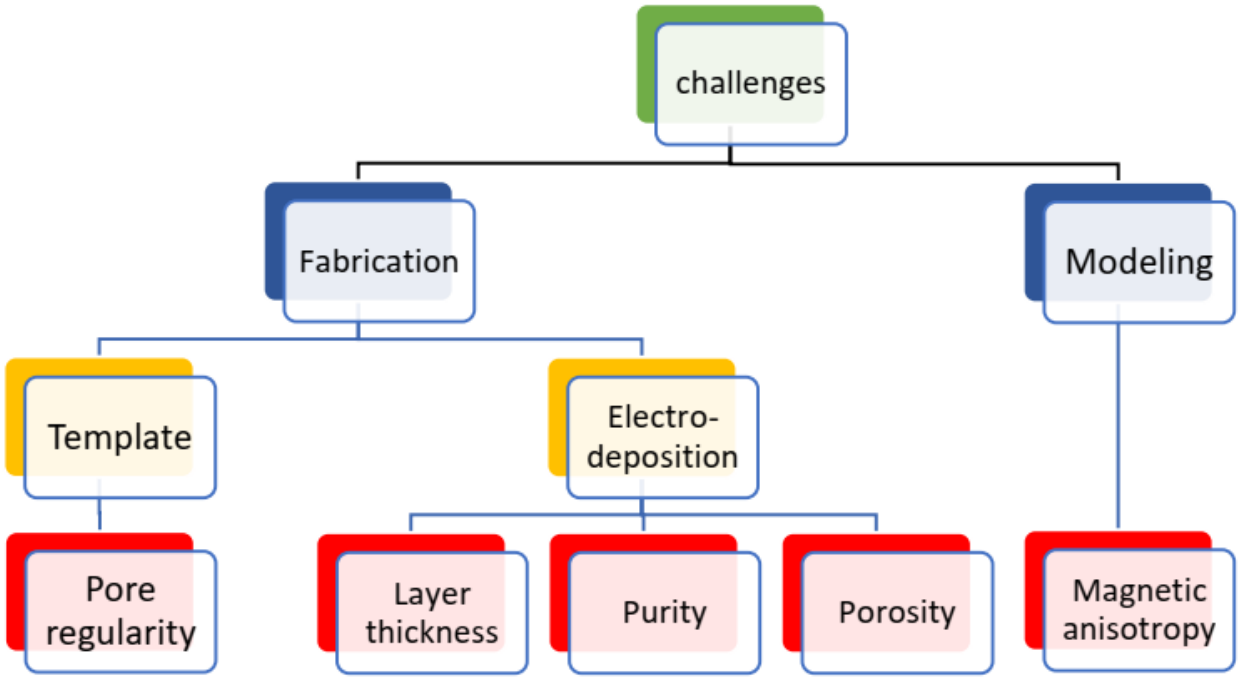

Figure 1.4 Organization of objectives of this thesis.

In fabrication process we have to first make a template and then deposit the magnetic nanowires into that template.

Our first objective is to improve the fabrication process of the templates. A great number of studies from many research groups have been done to address many challenges about alumina templates. However, to our knowledge, one challenge has not been systematically addressed so far which is pore regularity of these templates. Here we have developed a method to properly measure the pore regularity and then optimize the experimental conditions to obtain the best possible pore regularity.

Second, we address three main issues about the deposition of nanowires into alumina template : layer thickness, purity and porosity. In previous studies, it was shown that the layer thickness of magnetic and non-magnetic layers are not as expected. Also, during the electrodeposition process, there is always significant amount of non-magnetic material found in magnetic layers which is not what we want. Finally, the porosity, that is the ratio of deposition area to the total area, is not precisely measured which results in inaccuracy of our

subsequent calculations. We have also address these issues here.
Third, once we have our arrays of multilayer nanowires, we are interested in calculating (predicting) the magnetic anisotropy of these systems. In previous studies, a model was developed which can predict the magnetic anisotropy for some samples but unable to predict a range of samples with specific geometry. Here, we have extended this model so that it can cover a wider range of samples.
In what follows we first provide a review of previous studies and methods regarding the issues mentioned above and briefly explain our methodology for each challenge.

Organization of the thesis

In chapter 2 we first explain how the aluminium should be prepared before anodization to get the best pore regularity. Then, a high throughput method to fabricate alumina is introduced. Then we explain the gold coating process and why evaporation was preferred over sputtering method. This chapter is finished by explaining the Coulometry method and how we used this method to better control the layer thickness of deposited material into pores of alumina template.
In chapter 3, we introduce a method, level crossing analysis, to show how we quantitatively measure the surface roughness of aluminium. Then, we introduce an image processing method to measure the pore regularity (hexagonality) of our templates and to show the correlation between surface roughness and pore regularity. A new experimental method, overflow method, was then introduced to measure the effective porosity of samples by taking into account the fact that some pores during the electrodeposition will remain unfilled or partially filled. Next we show how we measure the layer thickness of our samples.
Chapter 4 is dedicated to the mean field model. In this chapter we first explain how the previous model was used to describe the magnetic anisotropy and then we explain our new model and we compare the two model. Some OOMMF simulations were shown at the end of this chapter to shed light into magnetization distribution of some structures.
Chapter 5 wraps up the experimental results namely the morphology of alumina templates, chemical analysis of samples, experimental measurement of the effective field using VSM and FMR and finally the comparison of these measurements with our new model is presented.
Last chapter, chapter 6, provides a conclusion of the project as well as some suggestions for future works.

CHAPTER 2 FABRICATION OF ARRAYS OF MULTILAYER NANOWIRES

2.1 Introduction

Here, we explain in detail all steps and procedures of fabricating arrays of multilayer nanowires, from cutting and pre-treatment of Al to electrodepositing of magnetic materials in alumina templates. The procedure might be slightly different in the first steps depending upon what type and shape of Al one is using. Some authors reported the use of Al rods to make the alumina templates but most authors use Al sheets (Sulka, 2008; Poinern *et al.*, 2011). We are using (and explaining) the treatment for Al sheets in this chapter. Fig. 2.1 shows the steps to fabricate a sample from beginning to end.

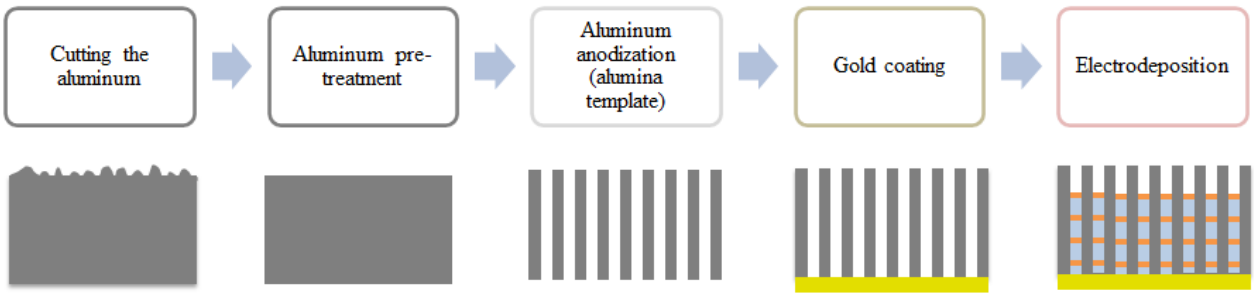

Figure 2.1 Main steps to fabricate an array of magnetic/non-magnetic multilayer nanowires.

In section 2.2 we first explain what types of pre-treatment are required before we can anodize Al. Then, in section 2.3 we provide detailed information about porous alumina formation. In section 2.4 we propose a simple solution to suppress gold diffusion into the alumina during the gold sputtering process (the gold is sputtered at the backside of the alumina to serve as cathode in electrodeposition process). Then in section 2.5 we propose a systematic coulometry method for electrodeposition, in order to achieve higher quality samples with more control over the thickness of deposited wires (having control over deposited thickness was an issue in our previous samples).

2.2 Aluminium preparation

The first, and very important step, in the fabrication of porous alumina is the surface pre-treatment, that is polishing and smoothing of the surface. It has a major influence on the quality of the self-organized anodization (Wu *et al.*, 2002). Pore nucleation is a random process. If the surface of the Al is perfectly smooth and polished, it will lead us to a hexagonal form as the pores grow deeper. Jessensky *et al.* (1998) has proposed that there is a correlation between mechanical stress at the metal/oxide interface and the formation of ordered hexagonal pore arrays due to the repulsive forces between the neighbouring pores. Nielsch *et al.* (2002) also proposed that the self ordering occurs due to the volume expansion of about 1.2 time during the formation of alumina from Al. However, if the Al surface has scratches or any surface fault before anodization process, the pores will be created at surface faults leading to disorganized pores. This is because at surface defects the field strength will show local variations. This non-uniform current distribution over the surface of the Al will lead to an enhanced field-assisted dissolution of oxide and a local thickening of the film. The higher current produces a thicker oxide layer (Sulka, 2008).

2.2.1 Pre-annealing effect on pore order

In general, pre-annealing can reduce the stress of the Al and increase the grain size of its crystals (Wu *et al.*, 2000; Jessensky *et al.*, 1998). This helps produce large areas of organized porous alumina. Moreover, a proper heat treatment can improve the thermal stability and resistance against acid, base, and other corrosive chemicals allowing them to be useful in a harsh environment (Lee and Park, 2014). A usual setting for pre-annealing the Al is applying $400 - 500^{\circ}$ C for $3 - 5$ hours under a non-oxidizing environment such as argon or nitrogen. It is very important not to anneal the Al while it is exposed to air or oxygen because the oxide layer which will be formed on the surface under this condition will be very thick, making further anodization impossible.

2.2.2 Mechanical polishing

As discussed above, the polishing of the Al surface is very important as the first step in pre-treatment of the Al surface. Some researchers have used only mechanical polishing before anodization, for example (Nakamura *et al.*, 1992; Zhang *et al.*, 1998). However, Da Silva *et al.* (1995) showed that it is almost impossible to achieve a microscopically smooth and undeformed surface using only mechanical polishing, even with a great care. For those reasons, people

usually combine mechanical polishing with either chemical or electrochemical polishing methods. However, based on our experience, we conclude that mechanical polishing can improve the results only if the original Al sheet is very rough. In that case, using only electropolishing will not provide a flat surface, rather it will smooth the surface of the mountains on the sheet. Therefore, in the case that the surface is so rough that you can see the roughness with naked eye or even feel the roughness with your finger, then mechanical polishing in order to achieve a reasonably smooth surface prior to electrochemical polishing is required. The electropolishing process is discussed in the next section.

2.2.3 Electropolishing

The general concept of electropolishing is simple. As illustrated schematically in Fig. 2.2, a piece of Al sheet of high purity (99.999%) and a graphite (or platinum) are placed in an acidic electrolyte, usually oxalic, sulfuric or phosphoric acid as they provide the best ordered porous alumina. By applying an electric field between electrodes, the positive ions (H^+) and negative ions (e.g. $X - O^-$ and $X - O^{(2-)}$) accelerate due to the applied field. Positive hydrogen ions travel to the cathode (Graphite or Platinum) and negative ions travels toward the anode (Al). The reactions

$$2Al^{3+} + 3O^{2-} \rightarrow Al_2O_3 \tag{2.1a}$$

$$Al_2O_3 + 6H^+ \rightarrow 2Al^{3+}(aq) + 3H_2O \tag{2.1b}$$

take place at the anode. Equation 2.1a represents formation and equation 2.1b represents dissolution of Al oxide (Aramesh and Cervenka, 2014). These reactions are the same during anodization and electropolishing. What determines which process is taking place (electropolishing or anodization) is the condition under which the reaction occurs. If the formation rate is higher, then anodization takes place and if the dissolution rate is higher, electropolishing take place. The main factors to be considered are applied voltage, acid pH and concentration, current density and temperature. For example, in a mixture of $H_2SO_4 + H_3PO_3 + H_2O(2 : 2 : 1v/v)$ at 80° C applying 12 V will electropolish the Al while applying 15 V and higher voltage in exactly the same condition will anodize and pore formation will occur.

2.2.4 Experimental process

The first step is to cut the Al sheets to correct size. Usually the area of the Al which will be in contact with the electrolyte should not exceed 1 cm^2. If the area is too big, the distance

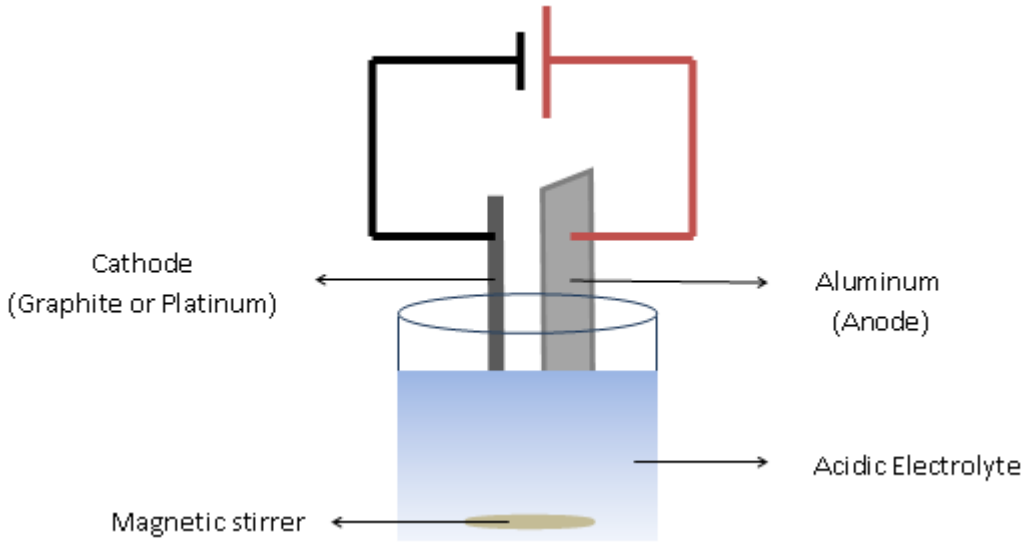

Figure 2.2 Schematic view of a simple setup for electropolishing the Al.

between the Al and the cathode would vary too much across the entire area of the Al. This causes varying current flow throughout the Al sheet and results in uneven polishing. Larger area means we need greater current flow, which increases unevenness. We cut our Al sheets in coupons of 0.5 cm × 10 cm and immerse only around 1 cm into the electropolishing solution. The Al should be placed on a flat and solid surface for the purpose of cutting (such as a thick glass). Otherwise there will be a curved surface along the cut lines. If the Al sheet is too thick, a rotary cutting tool with a diamond blade is recommended.

The second step is degreasing of the Al. We have used a solution of 1 M NaOH and allowed the Al coupons to rest in the solution for 2 minutes at room temperature. Then, they are immersed in distilled water to remove the NaOH. The immersion of samples in 5%NaOH at 60° C for 30 s or 1 min and subsequent neutralization in a $(1:1\ \ HNO_3H_2O)$ solution for several seconds was also proposed for Al degreasing and cleaning(Li *et al.*, 1998b). A mixed solution of $(HF + HNO_3 + HCl + H_2O(1:10:20:69))$ was also proposed for degreasing and cleaning of the Al surface, leading to a highly ordered, self organized nanopore array (Li *et al.*, 1998a)

The third step is preparing the electrolyte for electropolishing. For example, $60\%HClO_4 + C_2H_5OH(1:4, v/v)$ at 10° C and 500 mA cm^{-2} for 1 min is commonly used by many groups (for a full list of possible solutions see Sulka, 2008). What we have used here is $H_2SO_4 + H_3PO_3 + H_2O(2:$

2 : 1v/v) at 12 V for 6 min at 80° C which is the optimum condition as shown in table 3.1 in chapter 3. To bring the solution to the desired temperature it is important to cover the top of the acid container in order to avoid vaporizing the solutions, otherwise the relative mixture of the solutions will be changed. After 6 min, we immerse the polished Al in distilled water to remove the residual acids. It is important to make sure that the electropolish acid is completely removed from the samples. Even a single drop will destroy the samples during the anodization. It is also very important to stir the electrolyte properly and evenly in order to remove the heat which is created around the samples due to applied field and high current.

As mentioned in the previous section, if the polishing condition is not set correctly the final result will be worse than unpolished Al. For example, high voltage will increase the formation rate (see previous section) and results in porous instead of polished Al . If the above conditions and steps are not followed carefully, for example if Al pieces are very large or the temperature is not set correctly or the electrolyte is not stirred properly, the final result looks muddy instead of shiny. Fig. 2.3 provides digital photo and scanning electron microscopy (SEM) of some polished samples. Three different results were compared : careless setting of parameter which results in muddy samples, Fig. 2.3(a), very high voltage applied results in porous instead of polished Al, Fig. 2.3(b), and fairly a good polished samples, Fig. 2.3(c). In the latter case we can see round shadows which are due to some imperfection of the polishing conditions. We will see in Chapter 3 that applying 9V for 6 min at 80° C results in a fairly good smoothness of surface. However, as demonstrated in Fig. 3.7, there is still some roughness. Bellemare *et al.* reviewed the optimum conditions for electropolishing and anodization (Bellemare *et al.*, 2014).

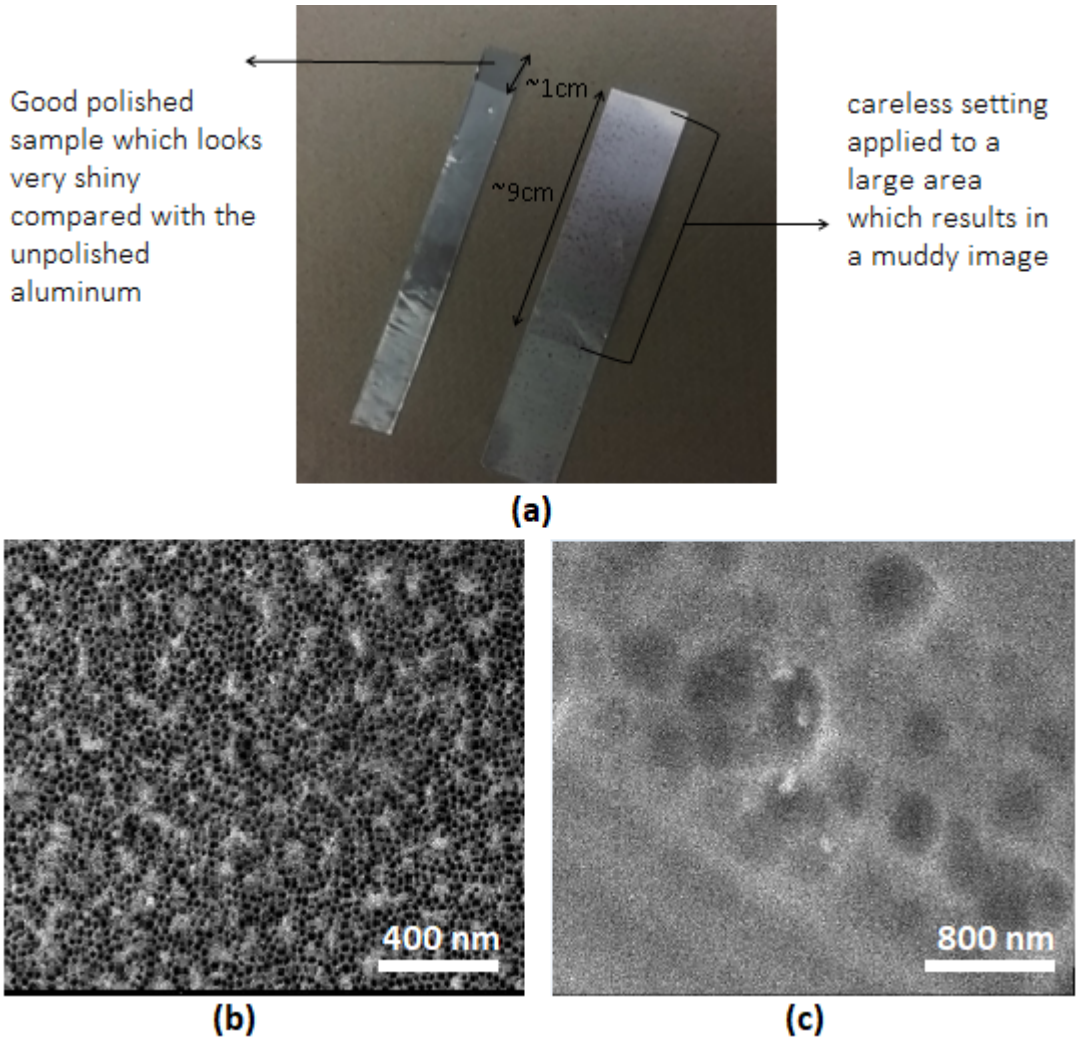

Figure 2.3 (a) Comparison of good polished with carelessly polished Al. (b) SEM image of a polished Al with high voltage and relatively long time (here 15 V and 3 min at 80° C) which results in pore formation instead of polishing. (c) fairly good results of polishing (here 9 V and 6 min at 80° C).

2.3 Anodization Procedure

After the Al is polished, we are ready to make our alumina templates. Alumina, or Anodic Al Oxide (AAO), is the template for our deposited nanowires. The special geometric feature of alumina (very high aspect ratio, good control over pore diameters and self organized property) makes it a good candidate for nanowire template. If fabricated under a certain condition (see Bellemare *et al.*, 2014), it provides hexagonally ordered pores with very high aspect ratio (length over diameter ratio in the order of 1000 or more). The hexagonality by

itself is not our concern, however it is important that they are ordered (in whatever manner) so we can make sure our model is consistent and our samples are reproducible. Moreover, since the self-ordered regime will naturally form if they are fabricated in a perfect condition, the regularity order also tells us how good is the quality of our membranes. Also, having a good and ordered template will help us with the calculation of coulometry (to be explained in following sections) in a more precise manner as in this method we need to know the total area of deposition in order to control the thickness of deposited layers. In what follows, we first explain the detailed steps of fabricating alumina. In Chapter 3, we develop an image processing analysis in the spatial domain in order to quantitatively evaluate the regularity of our membranes and compare with the widely used method of fast Fourier transform (FFT) which decomposes the image in its spectrum and analyses it in the the frequency domain (Stępniowski *et al.*, 2013).

2.3.1 Initial anodization steps

Anodization is a process in which the Al is the anode in an acidic electrolyte. Current passes through the surface of the Al, producing the oxide layer. Hydrogen is released at the surface of the cathode and oxygen at the anode surface (Al) creates Al oxide (Itaya *et al.*, 1984). The anodization of alumina has long been known. However, it was only in 1995 that Masuda and Fukuda first introduced the two-step anodization process in order to create self-ordered porous anodic alumina (Masuda and Fukuda, 1995). Depending on the conditions under which the Al is being anodized, one can obtain either ordered porous alumina or a solid oxide layer. A thorough review of anodic alumina formation has been provided in Poinern *et al.*, 2011 and Sulka, 2008.

Here, we explain the fabrication of alumina templates using the so called two-step anodization process. This process will introduce nano scale pores on the surface of anodized Al. However, the pore distribution in traditional methods is completely random. This makes the sample usable in limited applications, such as protection of surface and decoration, by improving the adhesivenss of the surface for painting and shining appearance. The two-step anodization method is based on the fact that the bottom of the pores becomes ordered in a hexagonal pattern as the pores grow deeper. After the first anodization, the first layer of alumina is removed, usually using a mixture of phosphoric and chromic acid, which leaves the surface of Al with hexagonal concave shapes that will serve as a starting point for the second anodization. The second anodization produces highly hexagonal ordered pores. A schematic picture of different steps is presented in Fig. 2.4.

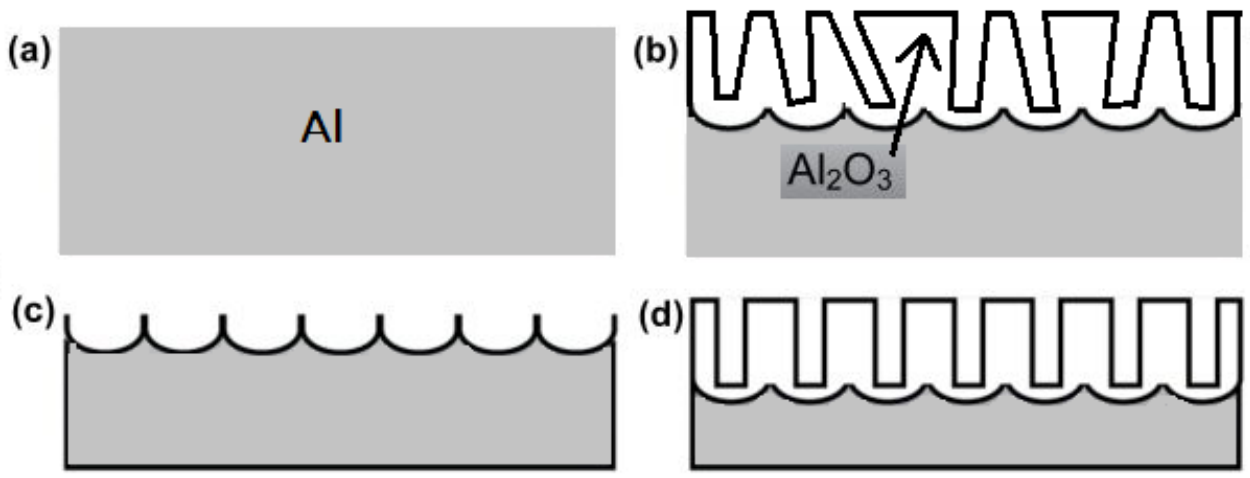

Figure 2.4 Schematic view of two-step anodization process (a) electropolished Al (b) first anodization with random pores (c) removing the first alumina layer (d) second anodization with hexagonal pore order.

There are different layers in anodized samples which are shown in Fig. 2.5.

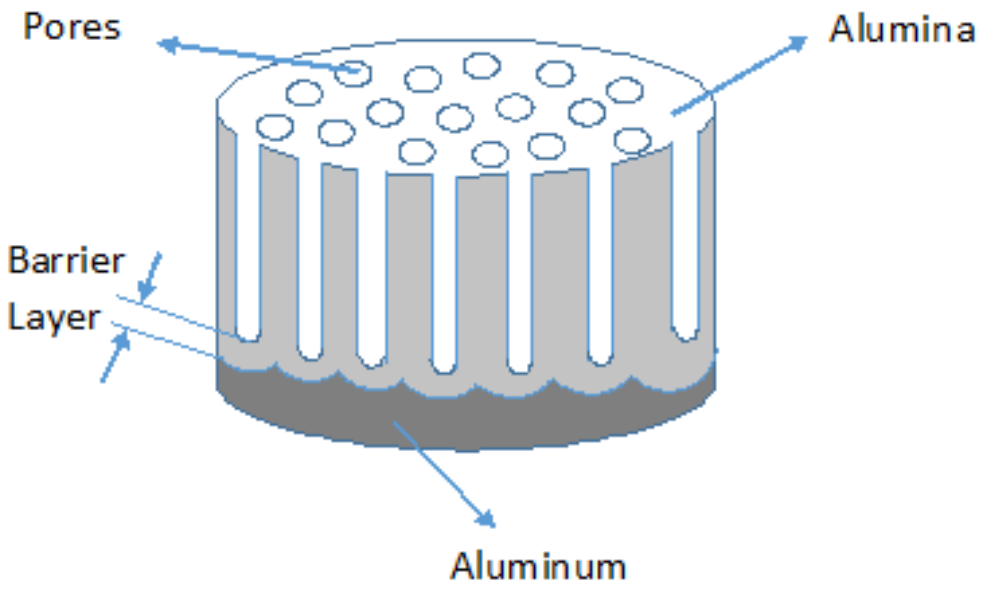

Figure 2.5 Different parts of alumina. Pores, barrier layer and Al base.

The most widely used fabrication process is :

After pretreatments, the Al is immersed in 0.3 M oxalic acid at 1° C as anode at constant

voltage of 40 V for about 2 hours. Then the first layer is completely removed using a mixture of 6 wt.% phosphoric acid and 1.8 wt.% of chromic acid at 75° C for about 2 hours. Then the sample is re-anodized under the same conditions as in the 1st anodization, to obtain ordered porous alumina. The growth rate of pores is approximately 2 μm/hour.

The Al base at the back of the sample is usually detached using a selective etchant, most commonly a solution of mercuric chloride, $HgCl_2$. The last step is then the barrier layer using phosphoric acid. The issue here is that phosphoric acid also affects the pores because not only the barrier is dissolved at this step, but the pore walls are also dissolved to some extent before the barrier layer is fully open. A careful study has been done by Bellemare *et al.* (2015) to address this issue and minimize this destructive step in the process of barrier opening. However, in order to completely eliminate this problem, Yanagishita and Masuda (2015) have proposed a high-throughput sample fabrication method, which we have adopted. In the next section we explain the differences between this method and the usual two-step anodization and explain its benefits. Throughout this thesis, we have fabricated our samples using 0.3 M oxalic acid at 1° C at constant voltage of 40 V which results in alumina templates with pores of about 50 nm in diameter and about 100 nm in interpore distance. To achieve other geometries one can use different acids with different concentrations, different temperature and different voltages. A through review of most common conditions is provided by Sulka (2008).

2.3.2 High throughput alumina fabrication method

After the second anodization, the samples are anodized in 12 M sulphuric acid for 20 minutes at 0° C and 40 V. This produces very soluble alumina at the bottom of the pores, while the pore arrangements are unchanged. Yanagishita and Masuda (2015) proposed that the high solubility of alumina produced in concentrated sulphuric acid is due to containment of sulphate anions in the alumina layer. Then, the samples are etched in a mixture of phosphoric and chromic acid, the same solution which was used to remove the first step of anodization, at 30° C for 15 minutes. This method has several benefits.

First, the detachment and barrier layer opening are implemented at the same time, very easily. Second, after detachment, the Al substrate retains the concave traces of the pores, ready for the equivalent of the second anodization step. This is very important because it saves time and resources, re-fabricating new alumina using the same Al sheet over and over, without repeating the electroplishing and first anodization steps. Moreover, a very large sheet of alumina can be obtained. This makes the next steps (gold coating) much easier. Third, the pores are almost unchanged during the detachment since it is done at a very low temperature and in only 15 minutes. Fourth, the use of toxic $HgCl_2$ is eliminated.

A digital photo of an alumina sample is provided in Fig. 2.6

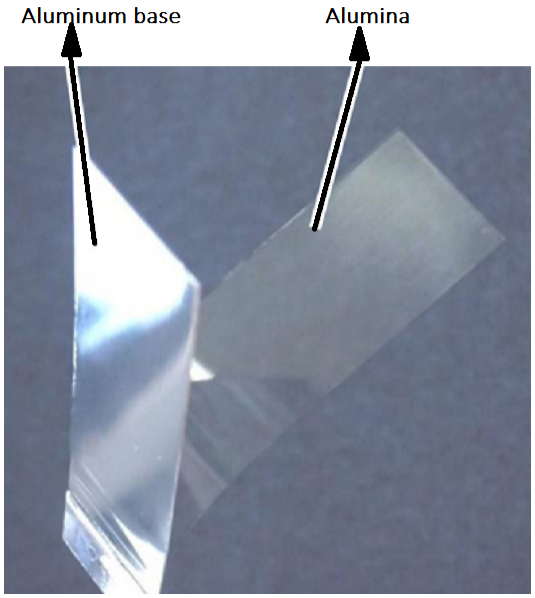

Figure 2.6 Digital photo of sample of an alumina made with high-throughput method. In this figure, the length and width of the alumina is 2 cm $\times$ 6 cm.

2.3.3 Controlling the geometry of alumina templates

Despite the many benefits of the two-step anodization method, one drawback is the limitation of our control over the geometry of the sample, mainly the interpore distance, D_p, and pore diameter, $2a$ (See Fig 1.1). These factors can be adjusted using different electrolytes and different voltages. However, control over those factors is limited, in comparison with electron beam lithography, for example. Different research groups have proposed different methods in order to gain control over interpore distance and diameter. These include using a mixture of different acids as electrolyte or increasing the viscosity of the electrolyte using some inert materials. We have listed the most common operational settings, using two-step anodization, in table 2.1. For a full review of different experimental settings in order to achieve different geometries, see Bocchetta *et al.* (2002) pages 64-66 and Bellemare *et al.* (2014).
A hypothesis testing was performed and is presented in chapter 5 to test the consistency of the geometrical parameters of our alumina templates, for a specific set of experimental settings. Regardless of our control over geometry of these samples, it is shown that there is no statistically significant difference between our samples.

Table 2.1 Most common operational settings for two-step anodization and the corresponding geometrical properties.

Electrolyte Acid	Concentration (M)	Temp (° C)	Potential (V)	$2a$ (nm)	D_p (nm)
H_2SO_4	0.18	10	25	24	66.3
$H_2C_2O_4$	0.3	1	40	31	105
H_3PO_4	0.1	3	195	158.4	501

2.4 Gold coating the alumina template

The porous alumina template is now used as working electrode for the electrodeposition of magnetic materials inside pores. We need a conductive surface at the bottom of the pores so that the elecrodeposition can take place properly. Usually, the porous alumina template is gold coated at the bottom. Sputtering and evaporation have served to gold coat the template. A thickness of 1μm was used in our samples.

Suppressing gold penetration into the alumina pores

There is one problem during the gold coating of the back side of the alumina, which will serve as the cathode later in magnetic deposition. The gold will penetrate into the pores during the coating process. Previously we have used sputtering to coat the back side of the alumina with gold. It is generally a more advanced process and is used more commonly than evaporation in metal deposition. We have used evaporation in order to minimize the gold penetration as explained below.

Sputtering vs Evaporation for alumina gold coating

Evaporation is a technique in which the depositing material (charge) is placed in a crucible and heated to its melting point. The material evaporates in all directions. When the vapor hits the cool surface of the wafer (target), some of the particles stick and create the depositing film. When this is done in a high vacuum, the mean free path is on the order of tens of meters. Deposition is highly directional in this method. Being directional reduces the step coverage. This is generally considered to be a disadvantage. Fig. 2.7 demonstrates this phenomenon.

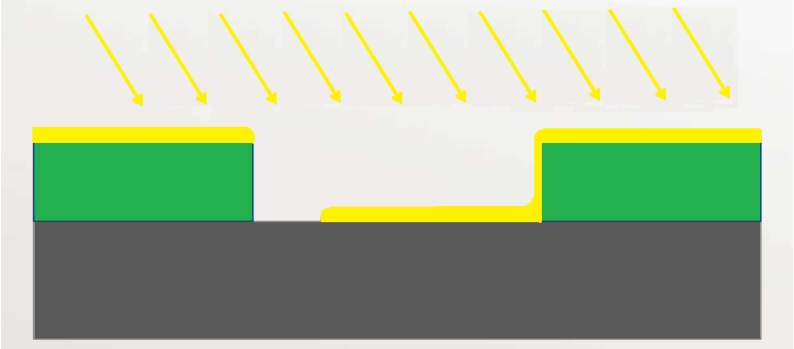

Figure 2.7 One property of evaporation is poor step coverage which in general is considered as a disadvantage in semiconductor manufacturing while it is an advantage in our case because we do not want gold to penetrate into the pores.

The step coverage becomes worse (in our case becomes better) with increasing aspect ratio. Since we do not want the gold to penetrate into pores, the poor step coverage is an advantage for us. Moreover, we can reduce the step coverage (in our favour) by offsetting the sample so that the evaporation direction is not perpendicular to the substrate. However, offsetting the sample will lead to a deposition uniformity problem since the uniformity of deposition depends on the angle of deposition. Fig. 2.8 illustrates the situation.

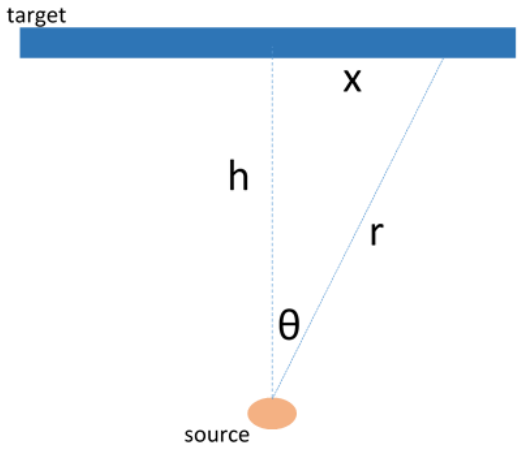

Figure 2.8 Dependency of deposition rate in evaporation method with respect to view angle θ. The further we go from the center the lower the deposition rate. This causes a non-uniform deposition across the sample. This problem can be minimized by rotating the sample during deposition.

Considering Fig. 2.8 we can write the following formula for deposition rate :

$$rate \propto \frac{\cos(\theta)}{r^2} = \frac{h}{(h^2 + x^2)^{3/2}} \tag{2.2}$$

Therefore, the farther we go from center, the poorer the step coverage we get. This is desirable. The cost, however, is poorer uniformity. Although the uniformity is not our main concern in this application, we can reduce the uniformity problem by rotating the target.
Following the above procedures, we were able to deposit gold on the back of our alumina, with almost no gold penetrated into the pores, and with good uniformity. A typical thickness for gold coating is around 0.8 to 1.0μm. Fig. 2.9 shows an SEM image from an alumina sample after being gold coated.

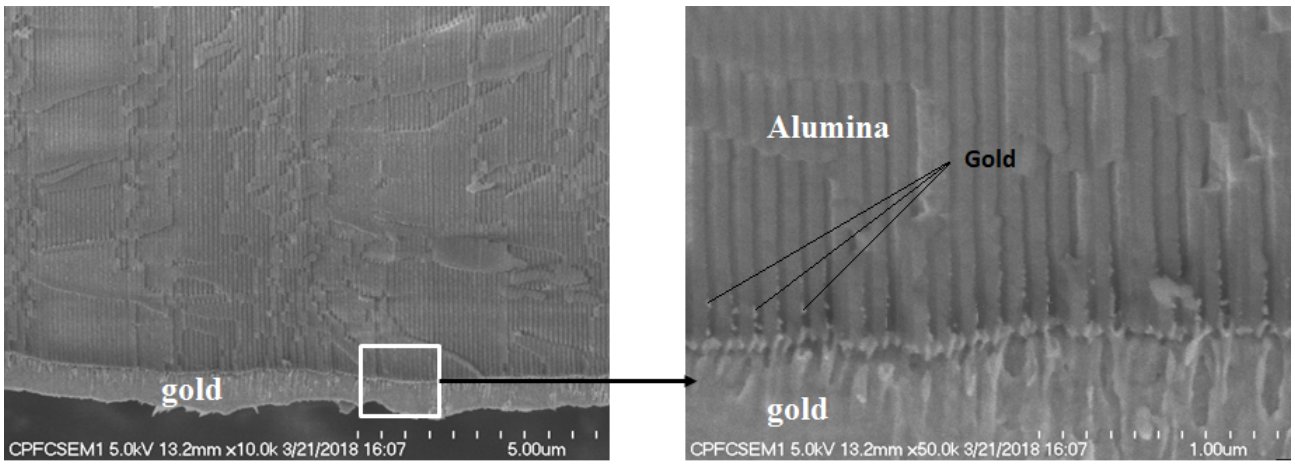

Figure 2.9 Using the evaporation method while the sample is placed offset with respect to the center above the charge, we can deposit gold at the back of the alumina with little gold in the pores. In order to keep the uniformity of the deposited gold in an acceptable range, the samples were rotated during the evaporation.

2.5 Multilayer nanowire array deposition

Among possible techniques for nanowire fabrication, the electrodeposition method has attracted much attention due to its simplicity and low cost, in comparison with other methods. The principal concept of electrodeposition is that, after coating a metal at the back of alumina template, the coated metal (Au in our case) is used as the cathode (also known as working electrode) while a platinum electrode is used as anode (counter electrode). A reference electrode is also used in order to keep the potential constant. The metal ions are then conducted

to the working electrode by applying a voltage between the working and reference electrode (the counter electrode is to provide the current). Figure 2.10 shows a schematic view of the electrochemical cell. As shown, we have created a hole at the bottom of the cell and attached the working electrode from outside so that we only expose the desired area of working electrode to the electrolyte. Depending on how much voltage we apply, we can deposit different metal ions. In the case of multilayer deposition for example, we switch the voltage between two different values in order to deposit two different ions (more to be provided in section 2.5.2)

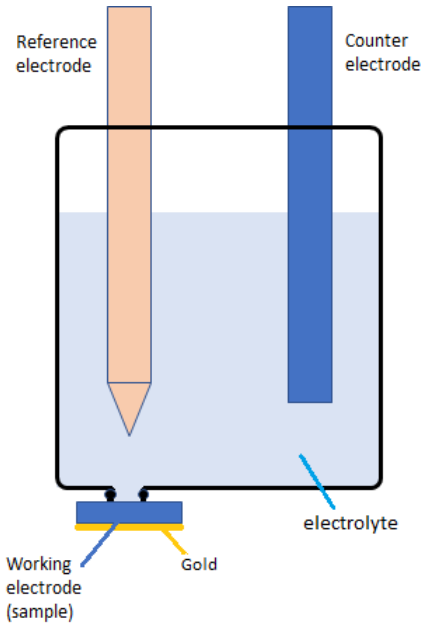

Figure 2.10 Schematic view of the electrochemical cell.

Although the electrodeposition is a fairly simple and inexpensive method, it has its own limitations and drawbacks. One major issue is that achieving layers with a given stochiometry is difficult. The problem is that the electrolyte contains all the metal ions which we want to deposit. Thus, we are co-depositing especially during the deposition of the less noble metal with lower deposition potential. For example, Copper will be reduced at the cathode at -0.56 V while Ni is reduced at -1.4 V. Although Ni will not reduce at -0.56 V, Copper can be reduced at -1.4 V and lower the purity of deposited Ni. In chapter 5, we have shown a simple strategy to minimize this effect along with the elemental characterization of one sample to see the purity of each magnetic and non-magnetic layer in our samples.
Another problem during the electrodeposition is controlling the layer thickness. The time of deposition is frequently used to control the thickness, based on the deposition rate of

a thin film of that metal. However, it was shown (Akhtari-Zavareh *et al.*, 2014) that both layer thicknesses and stochiometry could be significantly off using this method. In the case of deposition of nanowires in alumina pores, the deposition rate depends on many factors such as current and ion density which will decrease as more ions are deposited. Also, the porosity factor is very important for estimating the layer thickness.
For those reasons, we have used Coulometry, which measures charge being deposited for each layer by monitoring the current of the electrocell over time. Thus, we count the number of ions of the metal being deposited. Knowing the pore diameter, the area of deposition, and the density of the metal, we can estimate the thickness of the deposited metal. However, as mentioned above, we need to know the exact area of deposition as well as the effective porosity in which we are depositing. Also, a near 100% current efficiency is required in order to correctly estimate the thickness using coulometry method. We have addressed these problems in following sections. Specifically, we have designed a new method in order to measure the effective porosity of a porous alumina with known thickness.

2.5.1 Coulometry

In order to electrodeposit a material, one can use either the potentiostat or galvanostat mode. In the potentiostat mode, as the name suggests, the potential is kept at a constant value while in galvanostat the current is constant. The latter method is useful for deposition of a single composition because by switching between different currents it is difficult to keep the electrocell in a well defined potential causing co-deposition of our ions into wires. For that reason we will focus on the potentiostat mode which will produce relatively sharp interfaces between different layers (Ni/Cu in most of our samples).
One challenge in this method is to assure that the current efficiency is close enough to 100% so that we can assume that all the current we see is due to the desired material reduction and not to unwanted reduction. This is more problematic during the deposition of a less noble metal, Ni in this case, because at the deposition potential for Ni, Cu can also be deposited. Another source of error could be due to the interdiffusion of Cu during the process. However, since the interdiffusion is only significant at high temperatures, this phenomenon creates negligible current if creates anything at all. In order to minimize the deposition of Cu during the Ni deposition, we have calculated the minimum concentration of Cu which we can use to complete our electrodeposition without running out of it during the experiment.

2.5.2 Determining the Cu and Ni reduction potentials

Theoretically we can solve the Nernst equation in order to determine the reduction potential for Cu at cathode. This is basically related to the concentration of Cu. To have a sense about this we can assume that we want to have 99.99% of the Cu to be reduced at the end of the experiment. This can be achieved by solving the Nernst equation where we have $[Cu^{2+}]_{t_e}\,M = 0.0001 \times [Cu^{2+}]_0\,M$, that is at time t_e we have 0.0001 concentration of the initial concentration of Cu, $[Cu^{2+}]_0$. Substituting this equation into the Nersnst equation for Cu reduction :

$$E = E^0_{Cu^{2+}/Cu} - \frac{0.05916}{2} \log \frac{1}{[Cu^{2+}]} \tag{2.3}$$

where E^0 is the cell potential (V) at standard conditions and [ ] denotes the concentration. Assuming we have 3×10^{-3} initial concentration for Cu, the required potential will be $+0.15\,V$ for copper knowing that the required potential for reduction of Cu versus the standard hydrogen electrode is 0.342 in standard conditions. However, most often the reduction of Cu will take place in a more negative potential due to the overpotential[1] (Schönenberger *et al.*, 1997). Using a careful study with cyclic voltametry, -0.56 V is the optimum voltage for Cu reduction (Carignan *et al.*, 2011) for our experimental setting which is a single bath solution of 0.5-M $NiSO_4.6H_2O$, 0.003-M $CuSO_4.5H_2O$ with pH kept at 2.8 at room temperature.
In order to determine the potential for the less noble metal, Ni in our case, we have swept the potential from -0.03 V to -1.6 V to see in what range we can deposit the Ni. We do not want an overly negative potential in order to avoid reduction of H_3O^+ producing hydrogen bubbles near our working electrode. Controlling the applied electrochemical potential and the composition of electrolyte permits to control the advancement of the reaction of H_2 evolution. At the same time we do not want to go to a relatively too positive potential as well where the reduction of Ni is slow, while Cu continues to deposit. We have considered the inflection point (where the current curve changes concavity) as our criterion because from that point, decreasing the voltage does not change the rate of deposition very much. Fig. 2.11 confirms that -1.4 V is fairly a good choice for Ni.

1. Overpotential refers to the difference between thermodynamically determined reduction potential and the potential at which the reduction is experimentally observed

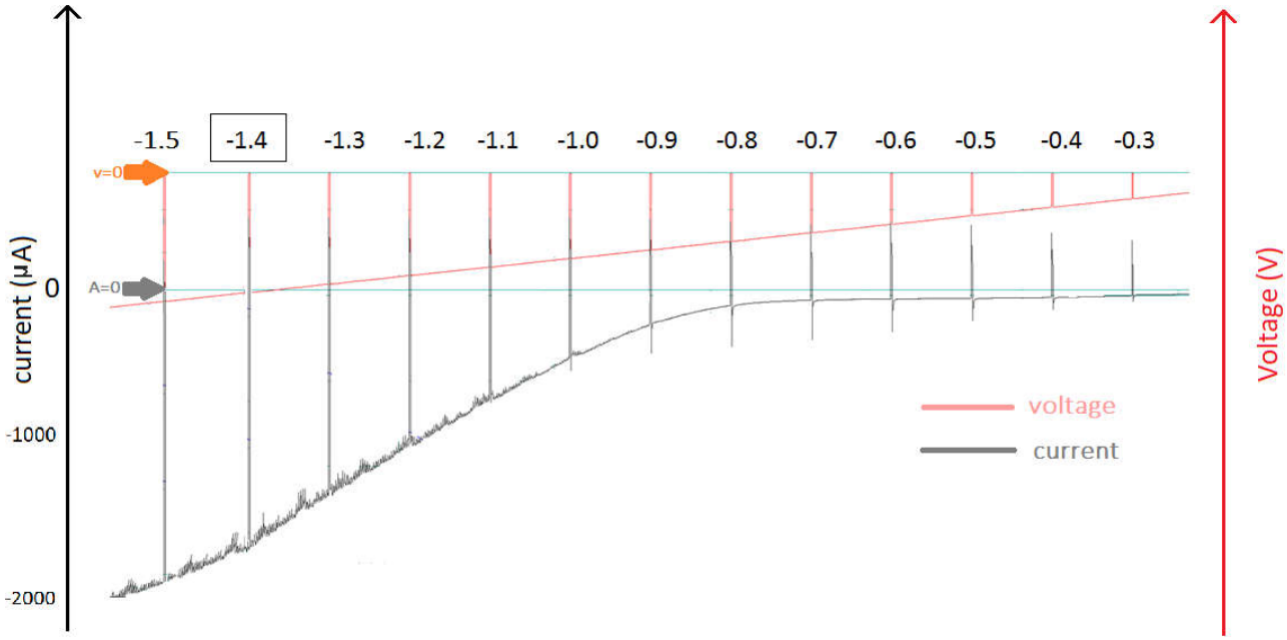

Figure 2.11 Current vs Voltage for the deposition of Ni. At around -1.4 V the deposition starts to be limited. The spikes in the diagram are due to very short breaks in applying voltage to let the electrolyte get refreshed.

These selected potentials, i. e. -0.56 V for the Cu and -1.4 V for the Ni will guarantee that we are close enough to 100% current efficiency so that the use of Coulometry method is justified. Please note that the method discussed here is only a validation of use of these values for potential while the exact numbers are adopted from literature.

2.5.3 Experimental implementation

In order to perform the electrodeposition and control the layer thicknesses by Coulometry, we have used a HEKA PG310USB model as our potentiostat which provides good flexibility to the user, who may computerize the process by developing a program to control the electrochemical cell where the electrodeposition is taking place. The schematic setting is shown in Fig. 2.12.

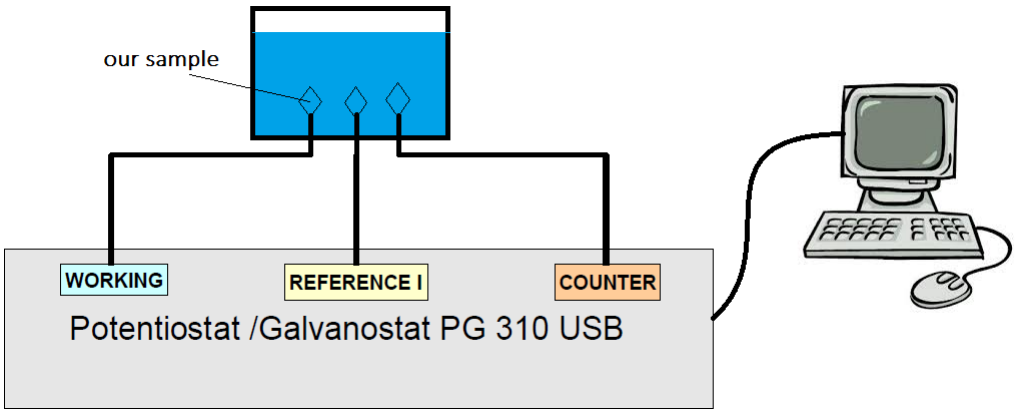

Figure 2.12 Schematic view of potentiostat and the electrocell setup.

In order to automate and connect our electrochemical cell to a computer, we use POTMASTER software. Using this software, we are able to use a computer program to communicate with our cell. As explained above, we have written a program (see annexe A) so that after a certain amount of charge has been transferred at a specific voltage, the deposition potential will be switched to another value to deposit the other metal and again switch back to deposit the first metal, etc. We can set how many times we would like this iteration to happen based on how many bi-layers we want. Depending on what voltage we set, we control what metal we deposit. For example, as explained above, a voltage of $-0.56\,\mathrm{V}$ has been set to deposit Cu in a bath of Cu and Ni ions, and a voltage of $-1.4\,\mathrm{V}$ has been set to deposit Ni. We have diluted the Cu as much as possible to minimize deposition of Cu at $-1.4\,\mathrm{V}$. Also, depending on what value we have set for breaking condition for the deposited charge, we can adjust the layer thickness of deposited material. In this example, we have set the breaking condition to $670\,\mu\mathrm{C}$ and $1.4\,\mathrm{mC}$ for Cu and Ni respectively. Using Eq. 3.14, which will be presented in the next chapter, we can calculate the corresponding thickness for each metal.
Figure 2.13 shows the total deposited charges as a function of time, as recorded from the HEKA instrument. As shown in this figure, we have been able to successfully transfer steady amounts of charge for each layer (the magnified figure on right).

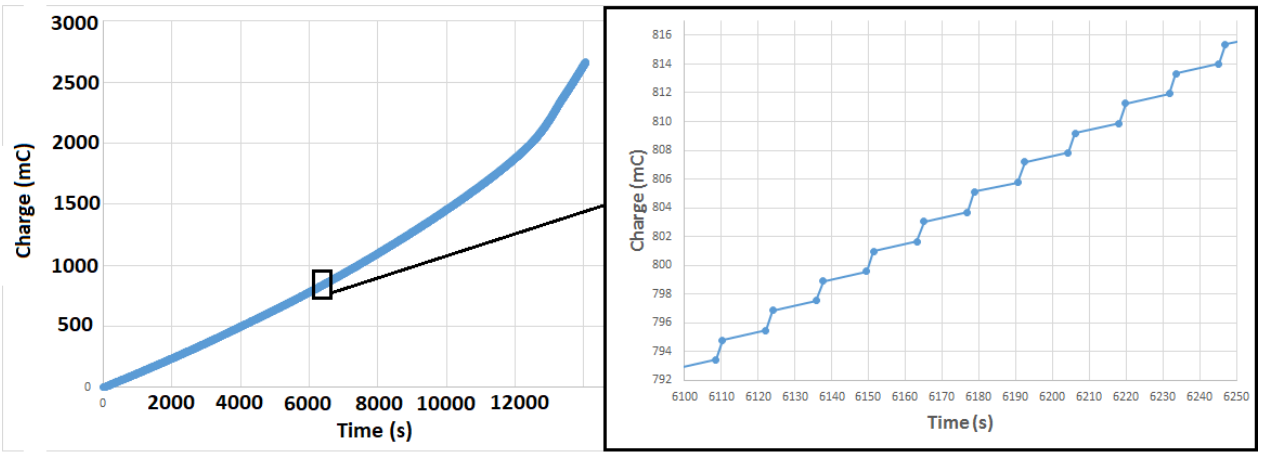

Figure 2.13 Charge (mC) vs Time (S) for a bi-layer of Cu(5nm) − Ni(20nm) multilayer structure.

Fig. 2.13 shows an increase in deposition rate around 11000 s, in other words, we observe the same amount of charge being transferred in a shorter time. One explanation could be consideration of deposition resistance. Because of very high aspect ratio in our template, at the beginning of the deposition, the ions pass through long narrow pores to reach the bottom of the template where they are deposited. As the deposition progresses, the pores are filled and the distance which the ions pass gets shorter. This reduces the resistance of the electrolyte inside pores and increases the deposition rate. There are several other factors controlling the deposition rate such as the concentration, applied voltage, pore diameter, filling factor, stirring rate, cell size, distance of the electrodes, temperature etc. However, the two leading factors after the electrocell is set, are deposition resistance, as explained above, and concentration. Ideally, other factors should not change during a course of deposition. The concentration however, will reduce the deposition rate as the deposition progresses simply because there are fewer ions to be deposited. However, as one can see in Fig. 2.13, the fact that the deposition rate is actually higher near the end of the experiment, the deposition resistance seems to be the leading factor in our setting. At this point, we can understand why Coulometry makes sense for control of the thickness. Coulometry does not depend on the factors mentioned above. For any deposition rate, we can always achieve the same thickness by counting the charges carefully.

One possible source of systematic error in this method is the the communication speed of the computer interface and the instrument response time. When the current is measured, it must be recorded with a specified resolution (for example we have set it to be one data point every 5 mS). Then the data should be sent to another processing i. e. calculating the integral

of the current with respect to time in order to count the consumed charges. Finally, based on the breaking point condition, the software should send a signal to the potentiostat to switch the voltage once the counted charge has reached a specified amount. All these processes take time to be performed. As a result, one can see a systematic error in the final results. The slower the processing speed the larger the error. However, using a reasonably fast computer (for example an Intel Core i7-7700K) will do the job quite well with minimal error.

CHAPTER 3 CHARACTERIZATION OF NANOPOROUS ALUMINA MEMBRANES

3.1 Introduction

In this chapter we first introduce a statistical method, called level crossing analysis (LCA), which quantitatively measures the surface roughness of an electropolished Al sheet. We propose an image processing method to accurately and quantitatively evaluate the regularity ratio of the pores in alumina. Then, we relate the surface roughness of an Al sheet to the regularity ratio of the alumina. We show that the regularity ratio of the alumina fabricated by anodization increases with the smoothness of the Al sheet. Our analysis is based on 16 different samples electropolished under different conditions but anodized under the same condition. Our results have been recently published in Journal of Porous Materials (Yazdizadeh *et al.*, 2020).

Next, we propose an experimental method in order to measure the effective porosity (filling factor). Porosity[1] is fairly simple and straightforward to calculate in an ideal situation, however, in reality not all pores are filled during the electrodeposition, making the real porosity smaller than its theoretical value. In this method we aim to estimate a more realistic value for porosity (filling factor).

Finally, using the method explained in 2.5.1, we estimate the layer thickness for one of our samples and compare it with experimental measurement obtained from SEM.

3.2 Surface roughness analysis : Level crossing method

Since the first studies of upcrossing and downcrossing of a stochastic signal by Rice (Rice, 1944), many studies have been devoted to signal processing and fluctuation of heights of rough surfaces including Level Crossing (LC) as a powerful method in complex systems (Brill, 2000; Movahed and Khosravi, 2010). In the LC method we are interested in determining the number of upcrossings (or downcrossings) of a given fluctuating signal, N_α, at any arbitrary level, α. In our case, the signal to be studied is the surface roughness of the electropolished aluminium achieved by a 3D optical microscope (also known as optical profiler) with a ZYGO NuView 5000 instrument (camera spatial resolution of 0.1μm) (Forman, 1979). It permits quantitative determination of the optimum condition of electro polishing (temperature of the electropolishing acid, duration of electropolishing and voltage).

1. Porosity and effective porosity will be discussed in Section 3.4

3.2.1 Methodology

To evaluate this method, we first simulate a set of data representing rough and smooth surfaces and then examine how the LC method can distinguish these simulated data. Let us consider a sample function of surface roughness fluctuations in the x-y plan represented by $S(x, y)$. We then assign surface roughness fluctuation to each point by $S(x_i, y_i)$ where x_i and y_i demonstrate the coordination position. The origin of the coordinate system of the sample is located at the left bottom of the corresponding map. Without losing any generality, we consider a one-dimensional slice of surface roughness fluctuation on a patch of a polished sample of size Θ parallel to x or y. We also consider $\mathcal{R}$ as the resolution of our data set, which can be our simulated data set or the measured data using Zygo. Obviously we have $\mathcal{R} = \Theta/N$ where N denotes the number of pixels in a slice. For meaningful statistical results, we consider a sample of an ensemble of one dimensional signals of surface roughness fluctuations, $S(k)$, in which k runs from 1 to N. Suppose n_α^+ denotes the number of upcrossings of $S(k) - \langle S \rangle = \alpha$ for a typical sample size $\Theta = \mathcal{R} \times N$ (see Fig. 3.1)

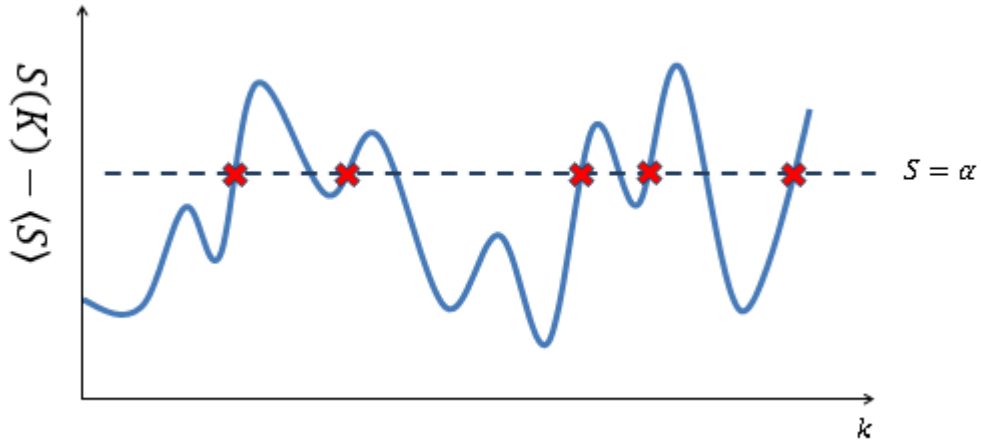

Figure 3.1 Positive slope crossing at level $S = \alpha$.

The ensemble average[2] of upcrossings is then given by :

$$N_\alpha^+(\Theta) = \langle n_\alpha^+(\Theta) \rangle \tag{3.1}$$

For a statistical isotropic and homogenous fluctuation, which is true in our case, the ensemble averaging can be done on various one dimensional slices of fluctuations. For convenience, we have chosen these slices to be parallel to the x axis without loss of generality. The number of crossings is proportional to the sample size Θ hence :

$$N_\alpha^+(\Theta) \propto \Theta \rightarrow N_\alpha^+(\Theta) = \nu_\alpha^+ \Theta \tag{3.2}$$

Where ν_α^+ is the average frequency of positive slope crossing at the level α. In the long run, there is no difference between using upcrossing or downcrossing. From a statistical point of view it is possible to deduce ν_α^+ from the probability distribution associated with the surface roughness fluctuation, $S(k) - \langle S \rangle = \alpha$. To calculate this probability distribution function, two necessary conditions should be satisfied for $S = \alpha$ as follow :

$$S(k_1) - \langle S \rangle < \alpha \tag{3.3a}$$

$$\frac{d\left[S(k) - \langle S \rangle\right]}{d_\Theta} > \frac{\alpha - \left[S(k_1) - \langle S \rangle\right]}{d_\Theta} \tag{3.3b}$$

Where $d_\Theta = \mathcal{R}$. These two conditions are shown schematically in Fig. 3.2.

2. We have collected data for 100 patches (ensembles) for each image. n^+ is the number of upcrossing for each patch while N^+ is the average of the 100 patches.

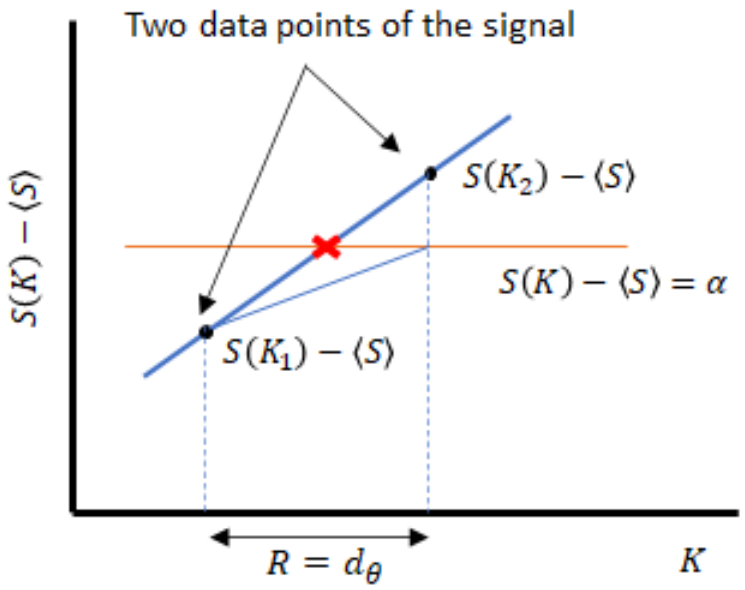

Figure 3.2 Schematic view of the two conditions in Eq. 3.3.

In other words, Eq. 3.3b is saying that the first data point should be below the level α and the slope of the signal at the first data point should be higher than the line which connects the first data point to level α at the second position. If these two conditions are satisfied, we can statistically expect high probability of an upcrossing in the interval d_Θ. To see if above conditions are satisfied at any arbitrary k, we should find out how the values of $y \equiv S(k) - \langle S \rangle$ and $y' \equiv d_y/d_\Theta$ are distributed by considering their joint probability density function $P(y, y')$. We can write the probability of upcrossing of signal at level $y = \alpha$ in the interval d_Θ as :

$$Probability = \int_0^\infty dy' \int_{\alpha - y' d_\Theta}^{\alpha} P(y, y') dy \tag{3.4}$$

When $d_\Theta \to 0$ we can write :

$$P(y, y') = P(y = \alpha, y') \tag{3.5}$$

Since at large values of y and y' the probability goes to zero quickly, we can rewrite equation 3.4 as :

$$Probability = \int_0^\infty dy' \int_{\alpha - y' d_\Theta}^{\alpha} P(y = \alpha, y') dy \tag{3.6}$$

So, because it does not depend on y, we have :

$$Probability = d_\Theta \int_0^\infty P(y = \alpha, y') y' dy' \tag{3.7}$$

Fig. 3.3 shows this calculation schematically.

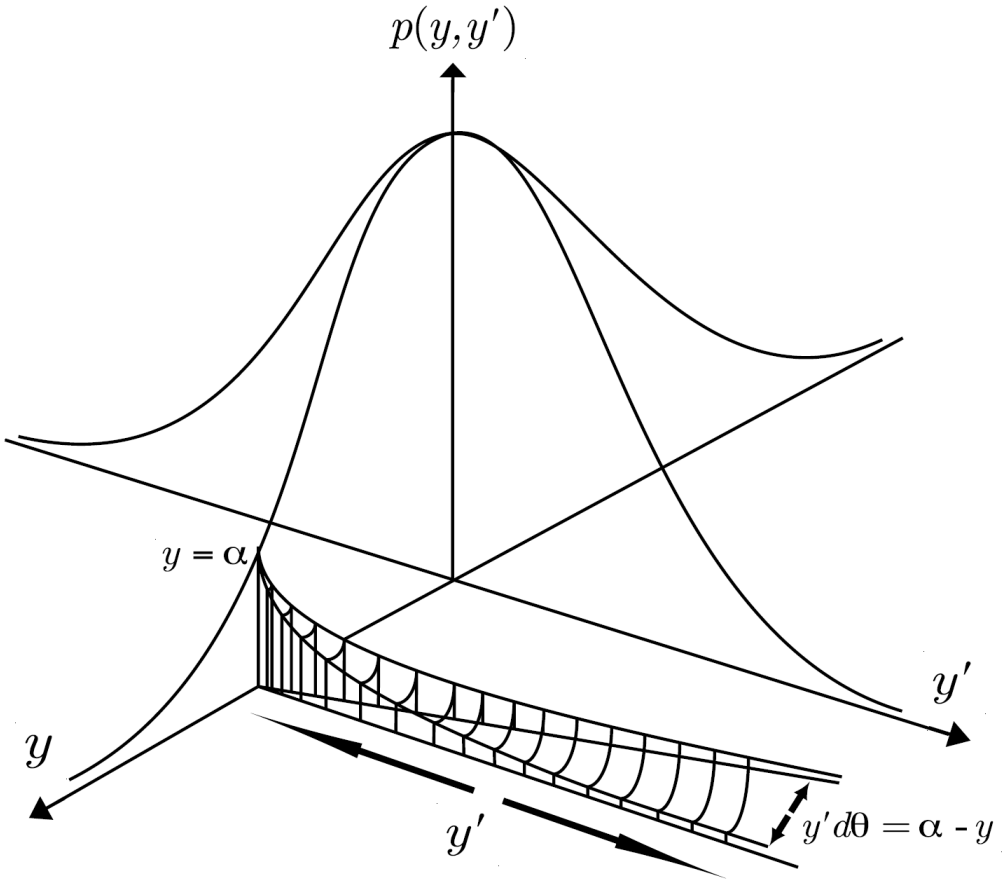

Figure 3.3 Schematic view of the joint probability density function of a typical fluctuation and its derivative. The hatched area is the probability of having an upcrossing at level $y = \alpha$.

Since we have already introduced the average number of upcrossings at interval Θ as $\nu_\alpha^+\Theta$ we can write :

$$\nu_\alpha^+ d_\Theta = d_\Theta \int_0^\infty P(y = \alpha, y')y'dy' \tag{3.8}$$

Or

$$\nu_\alpha^+ = \int_0^\infty P(y = \alpha, y')y'dy' \tag{3.9}$$

Another useful parameter based on ν_α^+ can be introduced as :

$$N_{tot}^+(q) = \int_{-\infty}^\infty \nu_\alpha^+ |\alpha - \bar{\alpha}|^q d\alpha \tag{3.10}$$

Where q is an arbitrary moment. For $q = 0$, Eq. 3.10 shows the total number of upcrossings for

surface roughness fluctuations at all levels. For a typical rough surface, $N^+_{tot}(q=0)$ is greater than that of a smooth surface and hence this quantity is a measurement of the roughness of the surface (Sangpour *et al.*, 2005). For $q < 1$, the terms in N^+_{tot} with small deviation from mean level, $\bar{\alpha}$, will be dominant which emphasises the small fluctuations while $q > 1$ emphasises the large fluctuations. Finally, we define LC as the normalized total number of upcrossings at all levels as :

$$LC = (1/r) \times \int_{-\infty}^{+\infty} \nu^+_\alpha d\alpha \tag{3.11}$$

Here, r is the resolution of α.

To examine the ability of the level crossing method in surface roughness evaluation, we need to simulate surfaces with known roughness. In order to simulate a surface with pre-defined roughness we have used the idea of autocorrelated signals. Roughly speaking, a correlated signal means having a positive value in a signal, makes it more likely to have the next observation with a positive value than a negative value and having a negative value makes it more likely to have the next observation also negative rather than positive (Vahabi and Jafari, 2008). However, an anti-correlated signal means having a positive value in a signal makes it more likely to have the next observation with opposite sign. Hence, a correlated signal is expected to be smoother and therefore has smaller value in its level crossing measurement while an anti-correlated signal is expected to very rough since any summit in the signal (which is the surface roughness in our case) is expected to be followed by a valley. In the following we have simulated three different kinds of signals : correlated with different degrees of correlation coefficient, completely random and anti-correlated signals with different degrees of correlation coefficients (simulation codes are provided in annexe A).

Figure 3.4 compares the level crossing of a correlated and anti-correlated signal with their shuffled data. Shuffling is a process in which the order of data points are randomly reordered so that there will be no auto correlation in the signal meaning that the autocorrelation coefficient is zero. As illustrated, the level crossing shows greater values when it is applied to an anti-correlated signal while it shows smaller values when applied to a correlated signal. It is somewhere in between for a completely random signal as expected. As shown in Fig.3.5, for a sinusoidal curve, as one may expect, the number of upcrossing is the same at all levels. Therefore, the level crossing will show a square shape rather than a bell shape curve. Fig. 3.6 also compares the level crossing for different signals with correlation coefficients of $+0.99, +0.7, +0.5, +0.2, 0, -0.2, -0.5, -0.7, -0.9$. As it is shown, the greater the correlation coefficient (or equivalently we can say the smoother the surface) the smaller the number of

level crossings.

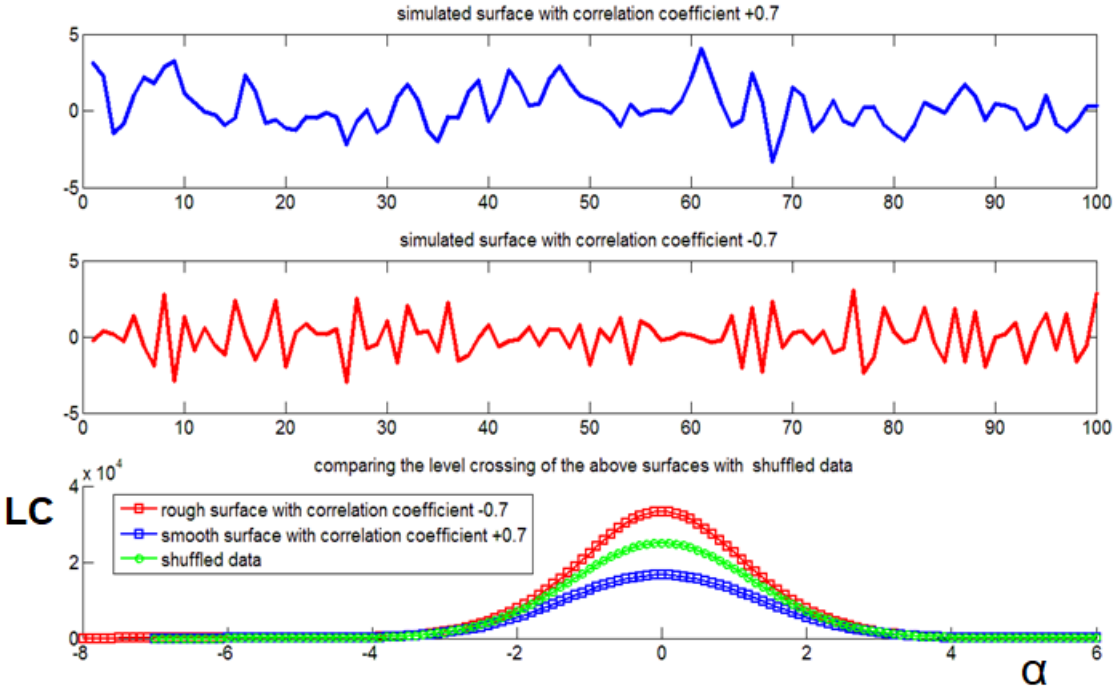

Figure 3.4 Top panel shows a simulated surface with correlation coefficient of $+0.7$ which is considered to be a smooth surface. the middle panel is the same simulation for correlation coefficient of -0.7 which is considered to be a rough surface. The bottom panel compares the level crossing of the two surfaces with their shuffled data, i. e completely random or we can consider it to be a signal with correlation coefficient of 0.

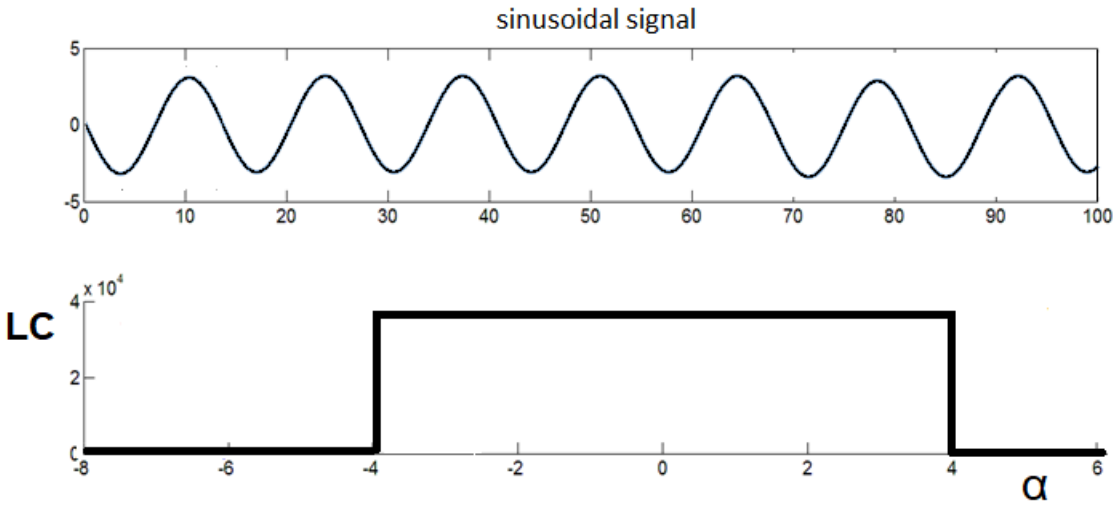

Figure 3.5 Top panel shows a sinusoidal signal. The bottom panel shows the corresponding level crossing analysis. For a sinusoidal signal, as the number of upcrossing is the same at all levels, the level crossing shows a square shape rather than a bell shape.

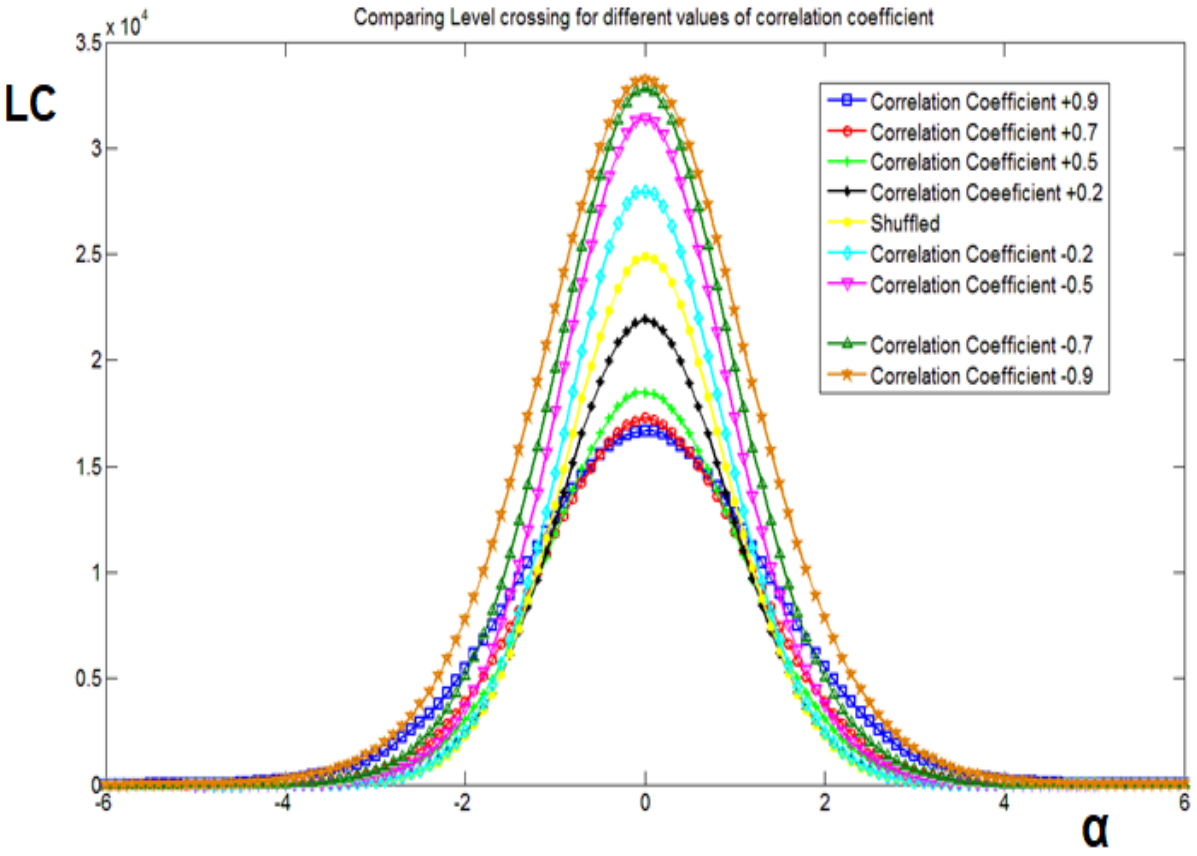

Figure 3.6 comparing the level crossing measurements for different surface roughness with different correlation coefficients. The smoother the surface, the lower the level crossing.

3.2.2 Experimental results

So far, we have shown that LC can be used in order to calculate the surface roughness[3] and we have shown that the smoother the surface, the smaller the LC. In order to measure the surface roughness quantitatively, we have used the parameter $N^{+}_{tot}(0)$ from equation 3.10 in our real data obtained from an optical profiler (interference microscope), ZYGO NuView 5000 (camera spatial resolution of 0.1 µm). The instrument was calibrated using standard samples with step heights of 0.01, 0.1 and 1 µm Zygo microscopy. In the following samples, we have changed the *voltage* at which the electro polishing is implemented, the *temperature* and the *time duration* of the electro polishing. The optimized condition will be associated

3. One may think that simply the standard deviation can be used without the complications of LC. However, there is much more information in LC compared to simply using the standard deviation. For example, standard deviation is sensitive to outliers or it does not differentiate between local or global roughness.

with the LC of the surface of the samples with the lowest value.

Fig. 3.7(a) to (i) show the 2D Zygo images for different sets of voltages, temperatures and times for selected polished samples. Area of each image is $0.1 \times 0.14\text{mm}^2$. Fig. 3.8(a) to (i) shows the corresponding surface profiles for the horizontal lines drawn in Fig. 3.7 and Fig. 3.9(a) to (i) are also demonstrating the corresponding 3D images of Fig. 3.7. In order to perform LC on these data, we have taken an image of the form presented in Fig. 3.7 and we have drawn 50 lines in random directions. For each line we have a signal such as those provided in Fig. 3.8 and then we attached these signals together in order to get a larger sample with more data (the bigger the number of data we use, the more reliable the conclusion we get from LC). Then we have performed the LC analysis using the MATLAB code provided in annexe A in order to calculate the total number of upcrossings for all levels. This is done by calculating the area under the curves produced by LC for each sample data.

The corresponding LC results of Fig. 3.7 are shown in Fig. 3.10. Except the first sample which was not polished, other data do not perfectly fit a Gaussian curve. This is because there is local roughness on the surface, that is, the surface was generally polished on a larger scale while there is still smaller scale roughness on the surface. This can be studied in detail by considering q different than 0 in Eq. 3.10. However, this level of attention is not necessary for our purpose.

We have performed LC on a range of different values for voltages, temperatures and times. The results are summarized in table 3.1. Looking at the polished samples, one cannot notice any difference between them. The difference is only obvious after the LC analysis is applied to quantitatively comparing the surface roughness of all samples. As shown in this table, the best (smoothest) surface was obtained for sample P12 by applying 12 V for 6 minutes at 80° C. One can try more settings to get even better results, for example, testing different electrolytes at different concentrations.

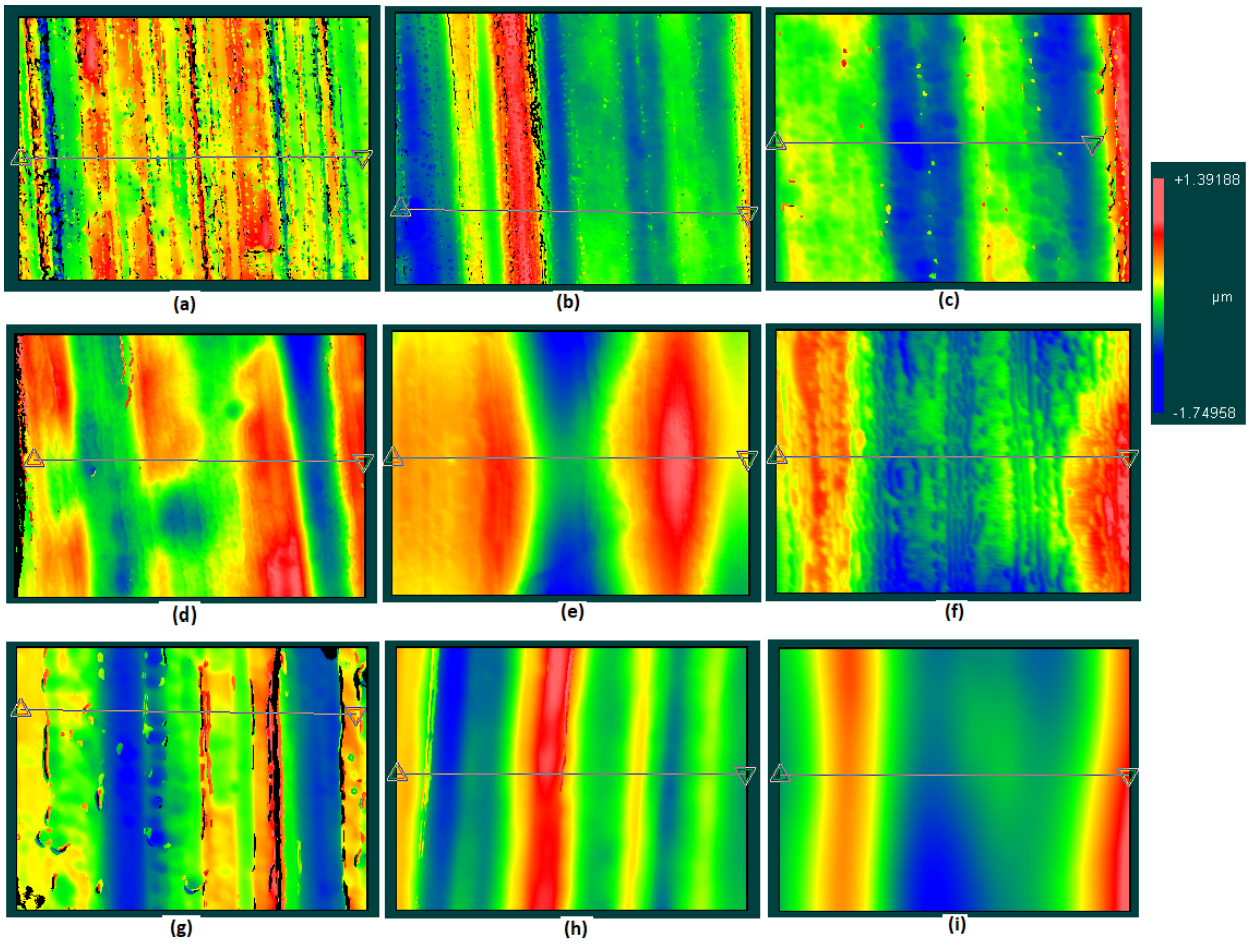

Figure 3.7 Zygo microscope images for (a) raw aluminium sheet without polishing (b) polished with 6V, 3min, 60°C (c) polished with 6V, 6min, 60°C (d) polished with 6V, 3min, 80°C (e) polished with 6V, 6min, 80°C (f) polished with 6V, 3min, 100°C (g) polished with 9V, 6min, 60°C (h) polished with 9V, 6min, 80°C (i) polished with 12V, 6min, 80°C. Area of each image is $0.1 \times 0.14\text{mm}^2$.

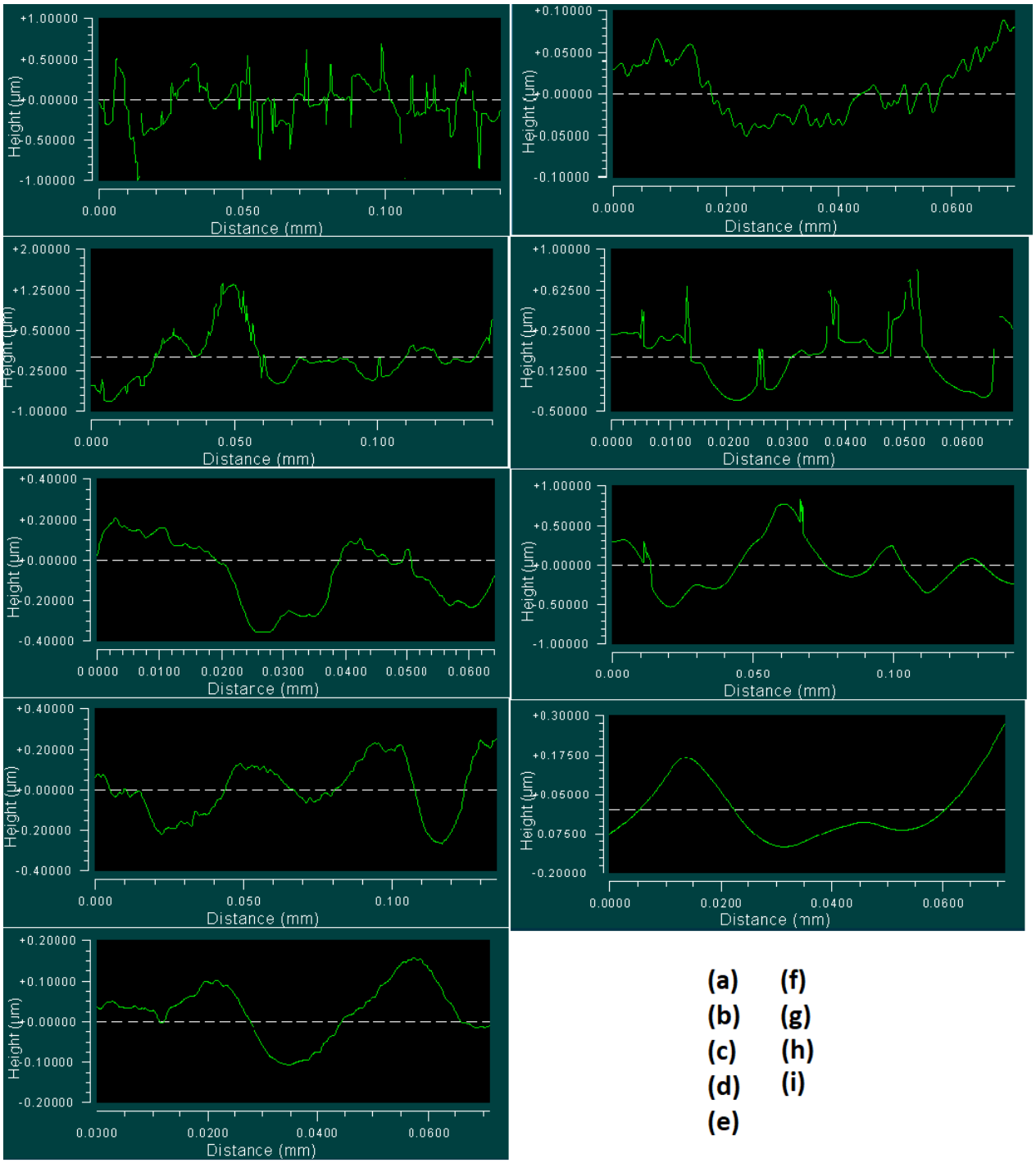

Figure 3.8 Surface profile for the corresponding images of Fig. 3.7.

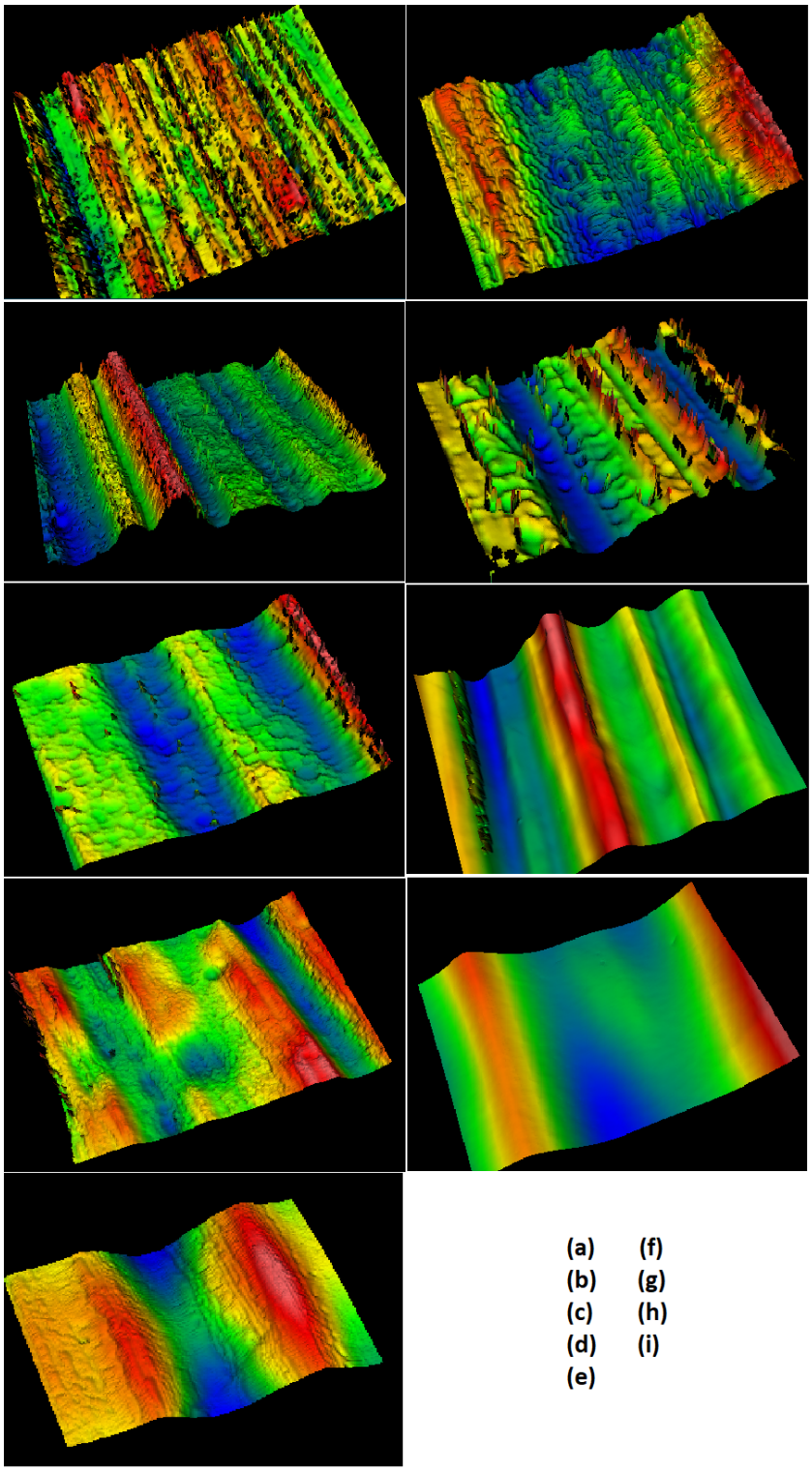

Figure 3.9 3D model of the corresponding images of Fig. 3.7.

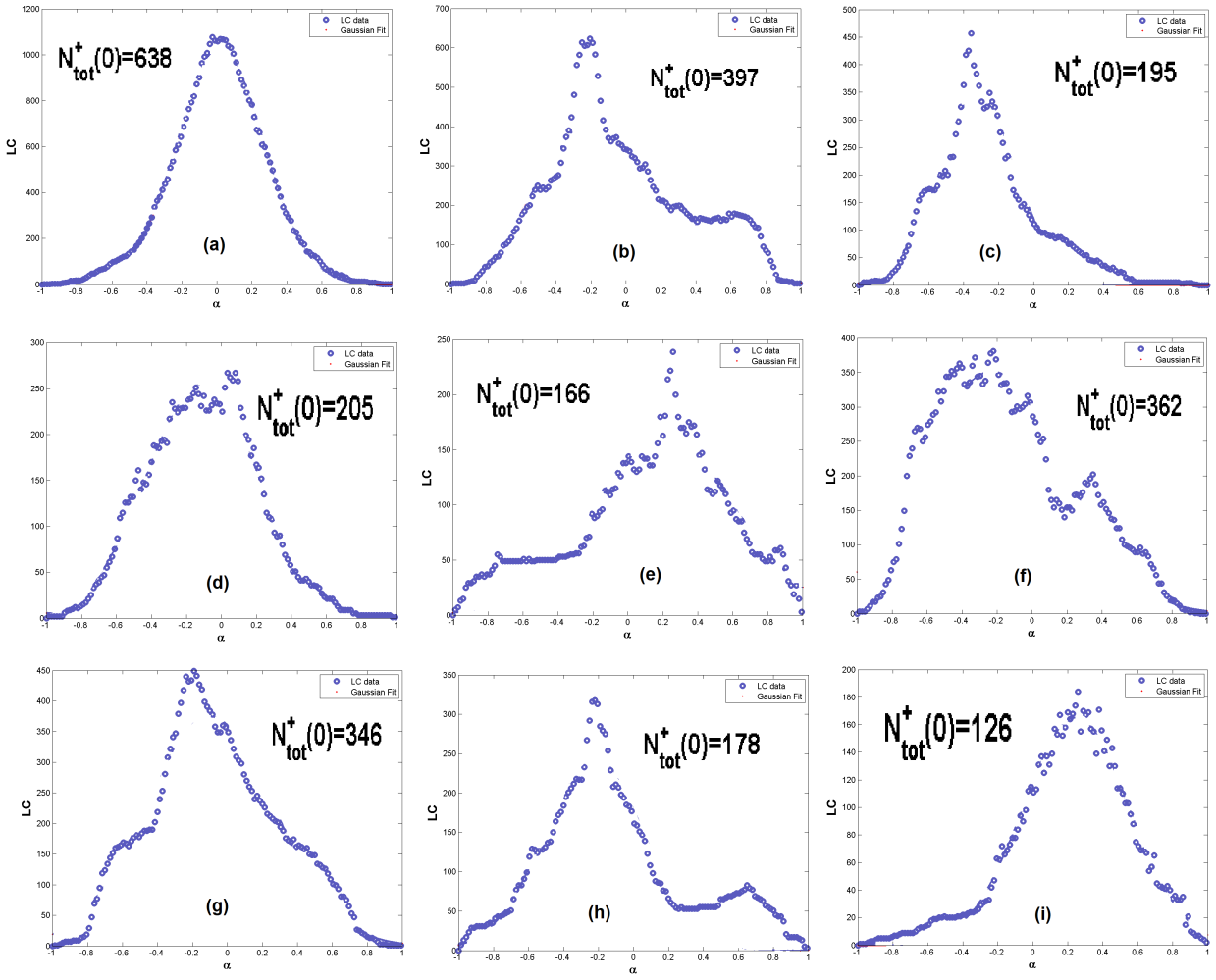

Figure 3.10 LC results of the corresponding images of Fig. 3.7. In each figure, the horizontal axis demonstrate the α i. e. the height of the level crossing analysis and vertical axis is the total number of up-crossing at that level as explained in section 3.2.1. $N^+_{tot}(0)$ shows the total number of up-crossing that is the area under the curve. This number is an evaluation of surface roughness as explained above.

Table 3.1 Values of LC analysis for different polishing conditions. The P1-P7, P9 and P12 are the samples corresponding to the results shown in Fig. 3.7. The best condition is highlighted for P12. $H_2SO_4 + H_3PO_3 + H_2O(2:2:1v/v)$ was used as polishing solution in this experiment.

Level Crossing(LC) results of all samples				
Sample Name	Voltage (V)	Duration (min)	Temperature (°C)	LC result
P1 (unpolished)	-	-	-	638
P2	6	3	60	397
P3	6	6	60	195
P4	6	3	80	205
P5	6	6	80	166
P6	6	3	100	361
P7	9	6	60	346
P8	9	3	80	204
P9	9	6	80	178
P10	9	3	100	98
P11	12	2	80	194
P12	12	6	80	68
P13	12	3	90	110
P14	12	1	100	143
P15	12	2	100	206
P16	15	1	100	123

3.3 Quantitative analysis of pore arrangement

Appropriate assessment of pore arrangement is crucial (Stępniowski *et al.*, 2013). Other research groups have used fast Fourier transform (FFT) analysis in order to evaluate it. Shingubara *et al.* (2010) suggested an FFT-based method for this purpose, considering the height of the 1st spot in the FFT image divided by the full width at half maximum (FWHM) as a regularity ratio. However, the results will depend on many factors such as number of pores to be analysed, surface area and porosity. Stępniowski *et al.* (2013) improved this method by

taking into account these dependencies and suggested calculating the regularity ratio, R :

$$R = \frac{(nS)^{-3/2}}{P^2} \frac{H}{W_{1/2}} \tag{3.12}$$

where n is number of pores, S is surface area, P is porosity, H is height of the first peak in FFT and $W_{1/2}$ is the FWHM. However, this method still suffers from being dependent on the intensity of the image being analysed, the shape of the framework (which might not be necessarily rectangular) and dependence on pore shapes. Most importantly, the FFT image should be transferred to a diagram which shows the intensity of the FFT image (arbitrary units) vs normalized width (1/nm). However, the intensity diagram is too noisy to provide a reliable measurement of the FWHM. It is also highly dependent on the direction in which one creates the intensity-width diagram. For example moving from top to bottom will give a different result from moving from left to right in measuring the intensity profile, since the FFT image is not perfectly symmetric. This becomes worse when an image with low regularity is being analysed, since there will be more noise, making it even harder to measure the FWHM. This is illustrated in Fig. 3.11 (a) to (c).

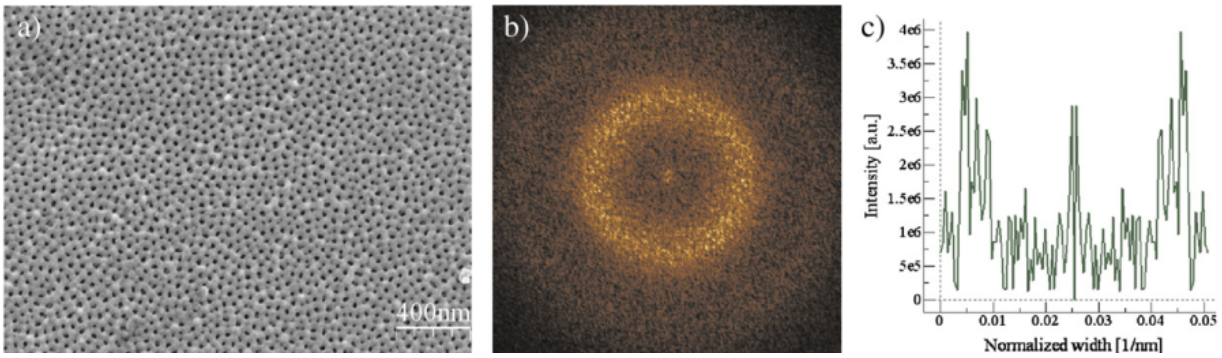

Figure 3.11 (a) Porous alumina of low regularity (b) the FFT image of the porous alumina (c) the intensity profile of the FFT. [figure reprinted from reference (Stępniowski *et al.*, 2013) with permission]

For all of these reasons, we need to develop a more reliable method which can give us the regularity of the porous alumina independent of all factors discussed above so one can compare the regularity criterion for micrographs taken with various microscopes in a meaningful manner.

Fig. 3.12 shows the flowchart of such an algorithm described above.

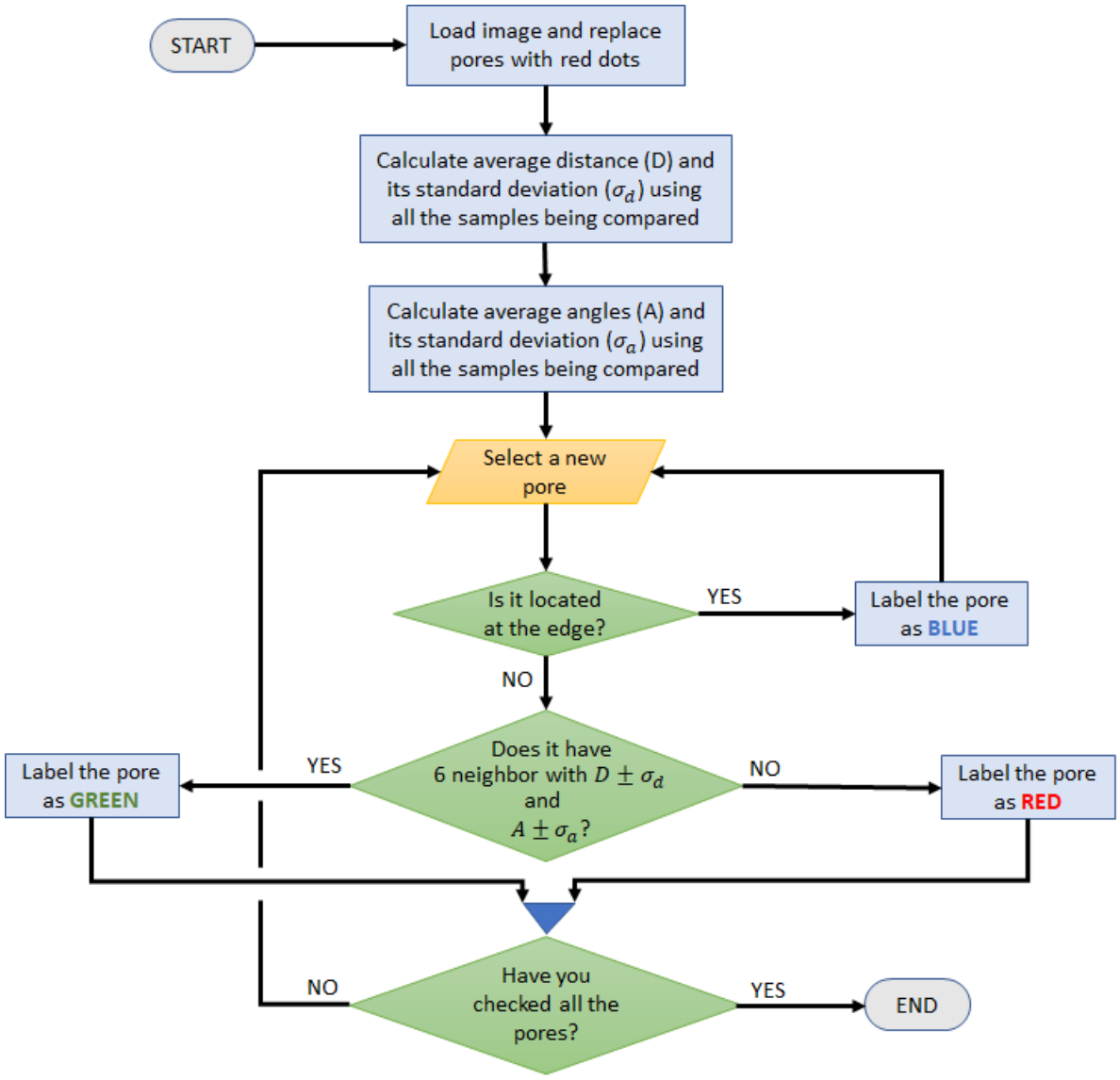

Figure 3.12 Schematic view of the image processing method for calculating the pore arrangement.

Fig. 3.13 shows the execution of this algorithm step by step on two different test samples (we call them TS1 and TS2). TS1 has been anodized without electropolishing and TS2 has been polished under the condition of P12 sample represented in Table 3.1.

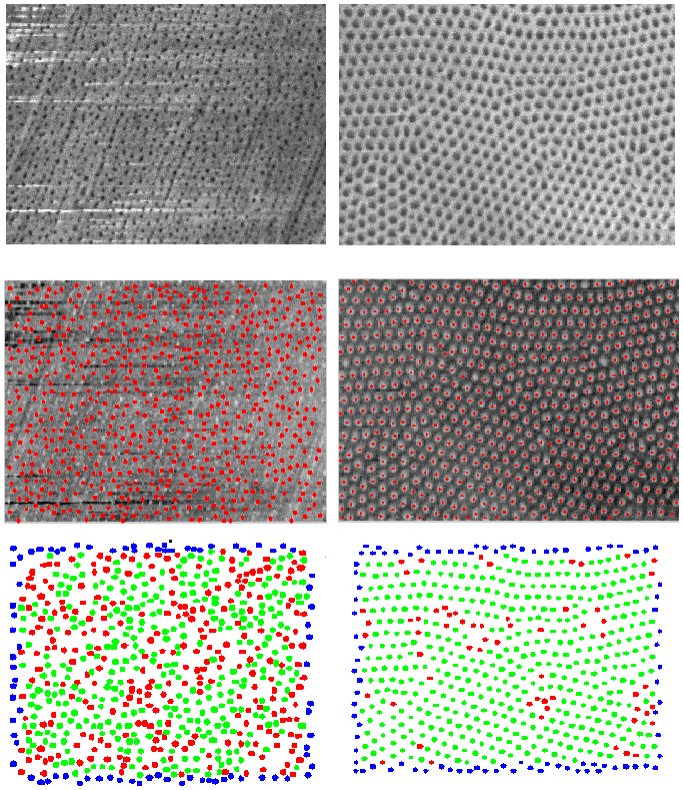

Figure 3.13 Left column shows our image processing execution on a sample without electropolishing (sample ST1) prior to anodization and right column shows a sample with anodization (sample ST2) under the same condition as sample P12 in table 3.1.The regularity ratio for sample ST1 is 29% within an error range of 2 standard deviations while the ST2 sample shows 90% regularity ratio within an error range of 1 standard deviation.

This algorithm has three main steps. First, we detect all the pores and replace them with single red dots. This eliminates the dependency of the result upon pore shapes and will provide us with a matrix which has only 0s and 1s (1s for the pores and 0s everywhere else). Second, we measure the distance between each pore and its neighbours and calculate its average and standard deviation. This is done using all the samples being compared to each other which are anodized under the same condition. Third, we repeat the previous process to calculate the average angle between pores as well as the standard deviation for the angle. The average of the angles should be 60°. We use 60° in the following steps, but we need this step to obtain the standard deviation. This is also done using all the samples being compared to each other. Fourth, we sweep the image and examine every pore one by one and verify if there are six neighbours within the one standard deviation of the average distance and if all

six neighbours are located at $60° \pm \sigma_{angle}$. If yes, we label that pore (previously red pixel) as green. Otherwise, we leave it as red. Since we are analysing the pores in the spatial domain rather than the frequency domain, and since we examine every pore with its neighbours, the pores which are located at the edge of the image are labelled as blue and are not taken into account for the calculation of regularity. We show the correlation between the quality of electropolishing (based on Table 3.1) and the regularity ratio percentage in Fig. 3.14. In this diagram the horizontal axis represents $1000/LC$ and the vertical axis shows regularity ratio. Here, we have defined the regularity ratio as :

$$R = \frac{\text{numberof GREEN dots}}{\text{numberof (GREEN + RED) dots}} \tag{3.13}$$

One can clearly see that the better the polishing (or equivalently the lower the LC is) the better the regularity ratio. Using this method, one can quantitatively and precisely determine the optimum condition to get the best regularity ratio based on the electrolyte acid he is using. Here, our data corresponds to the samples made in 0.3M oxalic acid. Each data point in Fig. 3.14 corresponds to a sample in Table 3.1.

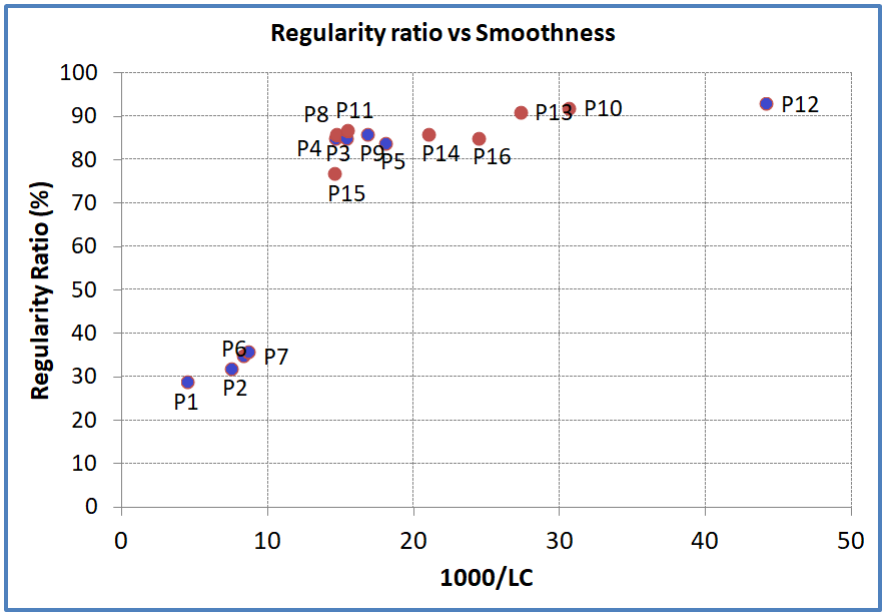

Figure 3.14 The correlation of surface roughness (smoothness) and its effect on regularity ratio of pores in AAO. Each data point here corresponds to a sample presented in table 3.1. The blue dots are corresponding to 9 selected samples represented in Fig 3.7.

Based on the results presented here, the best regularity ratio for samples made in 0.3 M oxalic

acid at 0°C and 40 V can be achieved for sample P12 in Table 3.1, which has the lowest LC value. The regularity ratio in this case is 90% while the regularity ratio for an unpolished sample (and under the same condition for anodization) is 29%. Notice that there are in fact two regimes in Fig. 3.14. IF the roughness is below some thresholds, the regularity is extremely poor. However, above the threshold the regularity jumps to a higher value. Above this threshold, there is little improvement in regularity even if the roughness is very low. We have used $1000/LC$ just to show the smoothness instead of roughness. The number 1000 was just selected so that the smoothness numbers range between 0 to 50 for convenience. One can use this method to optimize the operational condition for anodization for various electrolyte acids such as phosphoric and sulfuric acid.

Thus, we have shown that there is a correlation between the surface roughness of electropolished aluminum and the pore ordering of porous alumina. By quantitatively measuring the surface roughness and the pore ordering, we found that the smoother the surface, the higher pore ordering we can get in porous alumina.

3.4 Measuring the porosity

Usually people simply measure the porosity[4] by measuring the ratio of the area of pores to the area of the entire alumina sample. This is done by manually measuring the porous area and dividing it by the total area of the sample. In order to measure these areas, a more accurate method is using an image analysis software. However, the software generally measures based on the brightness of each pixel in the image. That is, based on a given threshold, the software counts the number of pixels with brightness below the threshold (as pore areas) and above the threshold (as non-pore areas). However, the main drawback of this method is that the result is very sensitive to the given threshold. Moreover, even in perfect conditions, there are always some pores which, due to hydrogen bubbles or other problems, will not be filled and therefore should not be taken into account in porosity calculation. In the following method, which we call overflow method, these issues are minimized. First of all, we need to know the thickness of our alumina template. This has been done using SEM photography. Fig. 3.15 shows this result.

4. Porosity and volume fraction of wires, filling factor, have been used interchangeably in this text. Ideally, porosity and filling factors are the same but since not all pores are fully filled, in practice they are different.

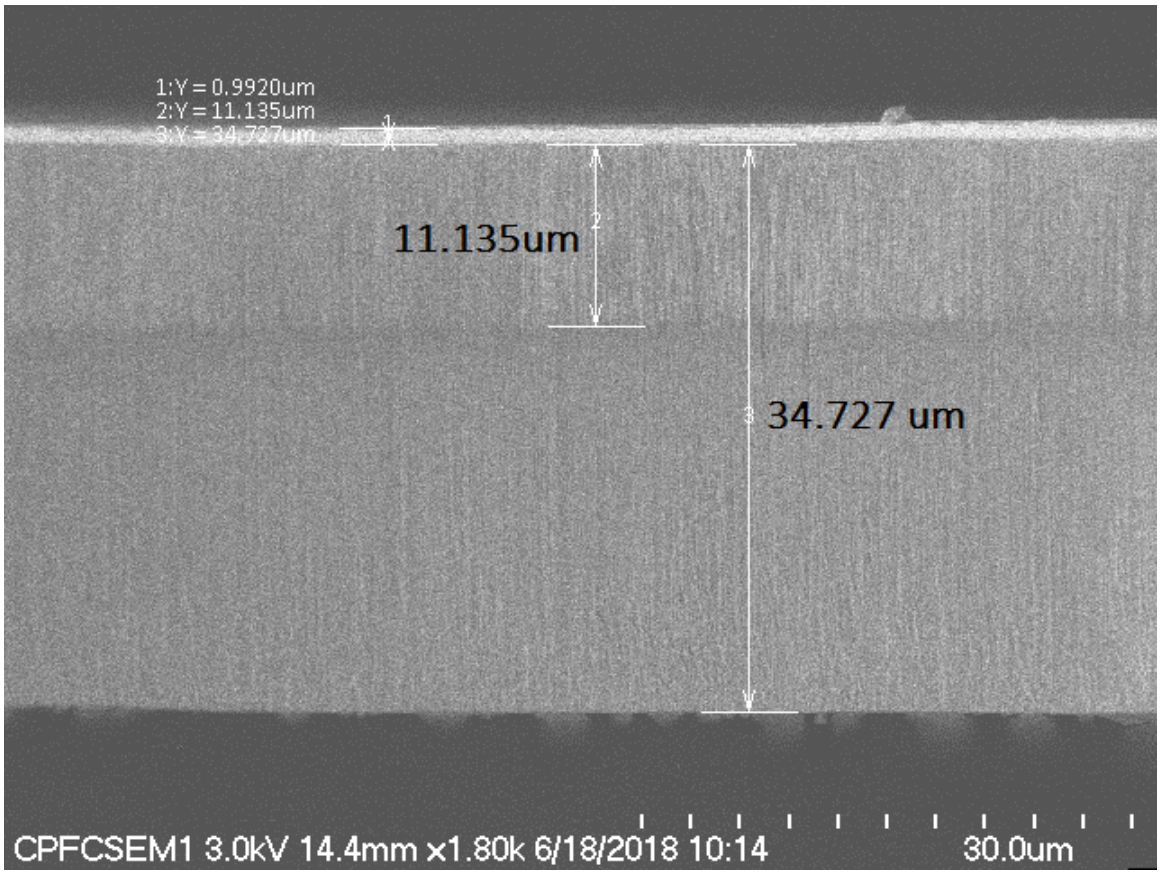

Figure 3.15 SEM image of our alumina template. The thickness of the template is $34.727/\cos(45°) = 49$ μm since the image is taken with sample tilted 45°. $11.135/\cos(45°) = 15.75$ μm is the length of nanowires deposited in this particular sample.

In order to monitor the deposited charge, we have recorded the current passing through the cathode during the deposition using a HEKA PG310USB instrument (the details of this process is explained in next section under Coulometry method). Briefly, the process is monitoring the current and taking the integral of the current with respect to time in order to have the deposited charge for each layer, as well as the total deposited charge. The idea is to let the metal be deposited until it overflows the pores. At that point we expect to see a sharp increase in current (or equivalently a sharp reduced time to count the same amount of charge) because the deposition area suddenly becomes larger. This is shown in Fig. 3.16. In our case, the thickness, d, of the samples is in the range of 47 μm $< d <$ 53 μm.

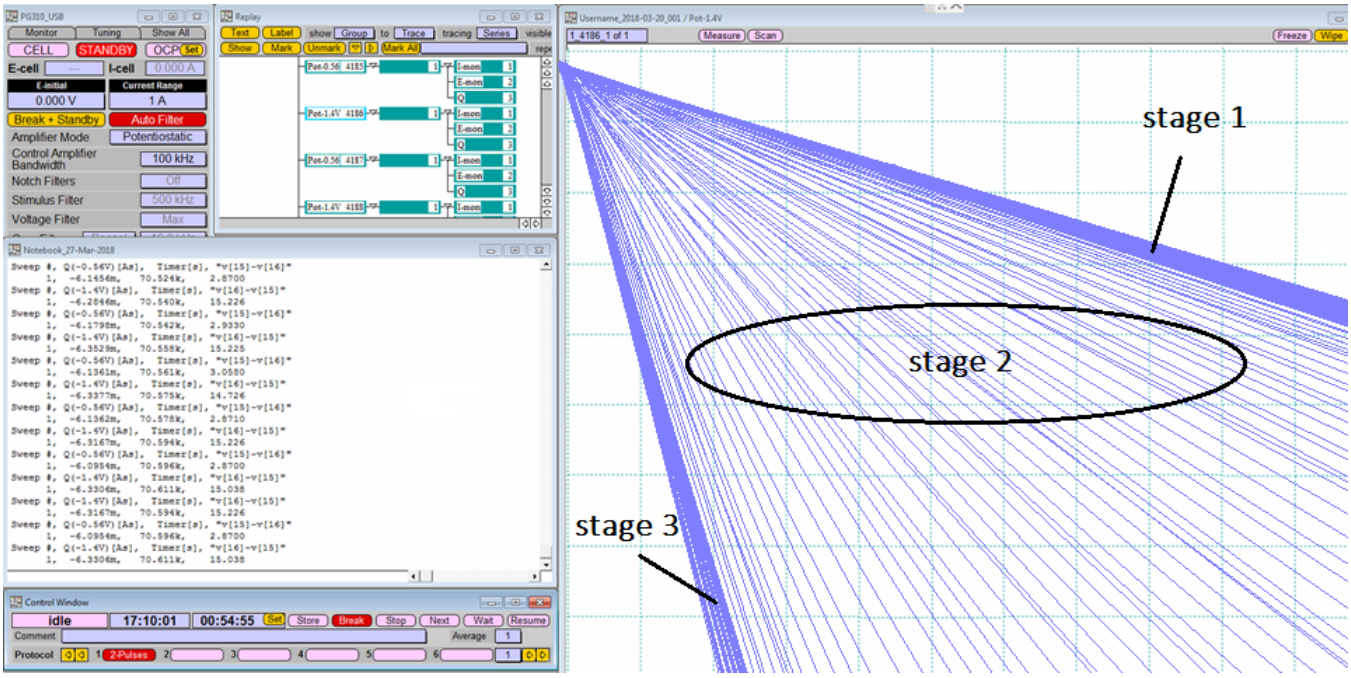

Figure 3.16 Right panel shows the deposited charge (range 7-8 μC) vs time (range 0.2- 3.0 sec) in the HEKA PG310USB software (Potmaster). The left panel is recording the data with respect to the experiment. As shown, stage 1 is when the material is depositing into the pores. Stage 2 is when the material just starts to overflow out of the pores. Stage 3 is when the entire surface of the template is covered due to overflow of the depositing material.

As one can see in this figure, the deposited charge vs time (horizontal axis), which is shown with blue lines, has started to drift to the left as the number of deposition layers increases. That means, the rate of deposition has started to increase. This is an indication of overflowing the deposited material out of the pores which results in acceleration in deposition rate. At the end of the experiment, the entire surface is covered by the deposited material. Fig. 3.17 demonstrates a schematic view of different stages of deposition process corresponding to the Fig. 3.16. We have considered the starting of stage 2 as our reference to when all the pores are filled. At that point we look at the total charge which has been deposited. We call that parameter Q which shows the total deposited charge to fill out the entire length of the pores. In this particular experiment we have $Q = 4200$ μC.

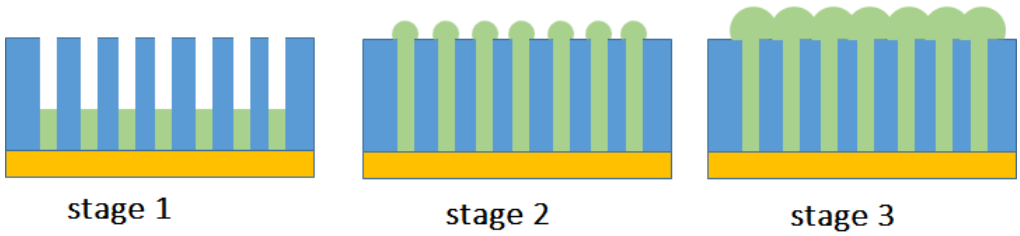

Figure 3.17 schematic view of stage 1, 2, 3 corresponding to Fig. 3.16.

The next step is to determine the entire area of the template where the deposition takes place. We have used the open source free software ImageJ to perform this step (Rasband, 2011). First, we have taken a digital photo of the sample. Then the software will recognize the edge of the deposition area. Then it calculates the area using an object with known dimensions as reference. A screen shot is provided in Fig. 3.18 to show what the software looks like.

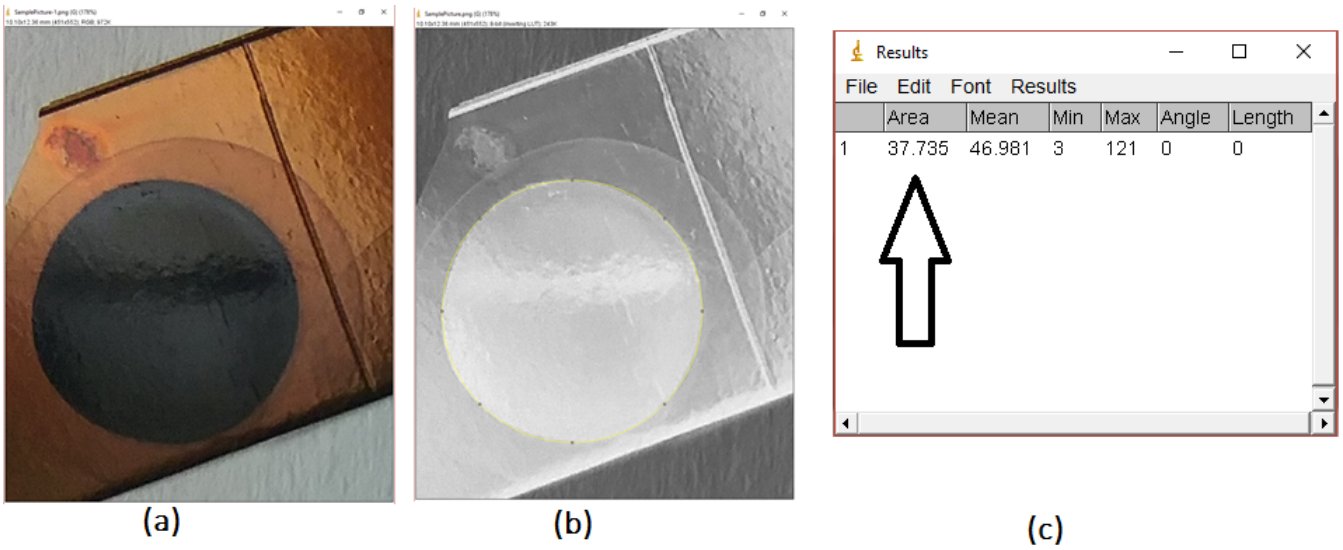

Figure 3.18 (a) The original photo (b) Transformed into a binary image and detecting the edge of the deposition area (c) calculating the area.

As shown in Fig. 3.18 the deposition area in this sample is 37.735 mm^2.
Now that we have all required factors we can use the following formula in order to calculate the deposition area which is the porosity factor.

$$d = \frac{\mathcal{M}}{ZF\rho}\frac{Q}{\mathcal{A}} \tag{3.14}$$

Where d is the thickness of the deposited layer (in our case $d = 49$ μm), $\mathcal{M}$, Z, F and ρ are molar mass, number of electrons, Faraday constant and density of the element respectively, Q is the total deposited charge and $\mathcal{A}$ is the area of deposition. By using $Q = 4200$ μC, $d = 49$ μm and knowing that $\frac{\mathcal{M}}{ZF\rho}$ is 36.7 for copper, we can calculate the area of deposition as follow :

$$\mathcal{A} = 36.7 \text{ (m}^3\text{/C)} \times \frac{4200(\mu C)}{49(\mu\text{m})} = 3.146 \text{ mm}^2 \tag{3.15}$$

Knowing that the total area of our template is 37.735 mm^2 we can deduce that the effective porosity is $\frac{3.146}{37.735} = 0.083$.

As mentioned in the beginning of this section, one can simply measure the area of pores and divide it by the area of the entire alumina sample. This method has two problems. First of all, we know that some pores remain unfilled during the electrodeposition so they should not be taken into account for porosity calculation. Second, the measurement of pore area is inaccurate. The best way to measure the pore area is by using a software to detect the pores in an image. This is done by labelling the pixels in the image either as pore or not-pore. However, this requires to set a threshold for pixel brightness so that above that threshold the pixel is labelled as pore and under the threshold it is labelled as not-pore. The problem is that setting this threshold is more or less arbitrary. To demonstrate this issue, we have performed the pore detection using three different thresholds for pixel brightness and as we see in Fig. 3.19, the porosity can be 0.23, 0.11 or 0.07 for thresholds of 100, 110 and 120 respectively.

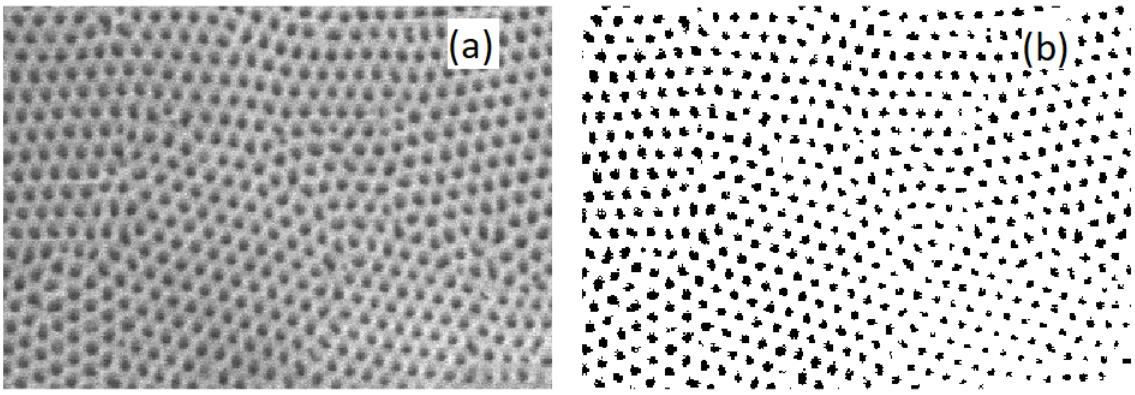

Figure 3.19 (a) The original SEM (b) Detected pores are transformed to black while the rest of pixels are white. The porosity, P=0.1124, is calculated by number of black pixels divided by total number of pixels in the image. The threshold was set to 110.

As discussed above, this method is very sensitive to pre-set threshold. In Fig. 3.20 we have performed the same algorithm above but for two different thresholds which results in P = 0.23 and P = 0.07 for thresholds of 100 and 120 respectively.

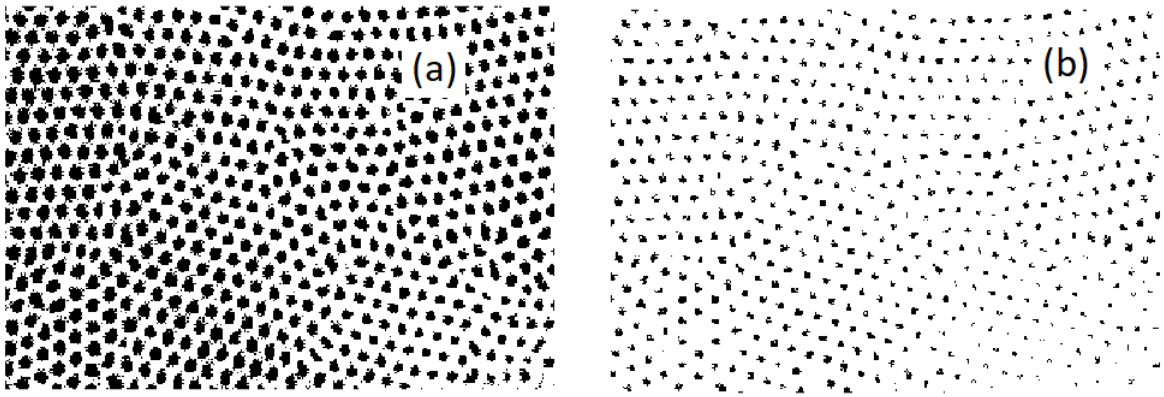

Figure 3.20 (a) Detected pixels of pores for a pre-set threshold of 100 resulting in porosity = 0.23 (b) Detected pixels of pores for a pre-set threshold of 120 resulting in porosity = 0.07.

Clearly, if someone tries to manually measure the porosity, the error is even higher. For instance, in Carignan *et al.* (2007) the porosity for the sample CoFeB was determined as P = 0.178 while the porosity for the sample 50(Ni30/Cu35) was determined as P = 0.050. However, in the same paper, it was mentioned that the alumina samples used in this research are commercial Whatmann Anodisc25 alumina membrane. We would find it quite surprising that a commercial product would exhibit so much fluctuations in the porosity. One should also note that, as a general rule, we expect the porosity to be around 0.1 (Nielsch *et al.*, 2002). If we had used P = 0.050 for the CoFeB sample mentioned above (instead of 0.178) the effective field[5] would be 6400 Oe instead of 3500 Oe reported in the paper. Also, for the sample 50(Ni30/Cu35) if we use P = 0.178 instead of P = 0.05, the effective field would be -2500 Oe instead of -1980 Oe reported in the paper.

Please note that although the tested sample in both methods is not usable for further experiments (due to the destructive nature of SEM) this is not a problem. As we see in Fig. 2.6, our samples (alumina templates) are very large. Therefore, we can use a small cut of the alumina template for porosity calculation and use the rest of the template for electrodeposition.

5. Effective field is defined as the required field to produce the observed magnetization in a system since the magnetization is not necessarily aligned with external field. This concept is discussed in detail in Chapter 4 and 5.

3.5 Measuring the layer thickness

One problem to be addressed in multilayer deposition is to improve control over thickness of deposited layers. Here we try to minimize the error of this estimation.
Since we can now calculate the effective porosity, i. e. the effective number of pores which are filled during a deposition process, we can use that to estimate the thickness of each layer. Previously we used equation 3.14 in order to measure porosity assuming that we already know the thickness. In section 3.4, we calculated the porosity and used the thickness of the alumina template to achieve the area of deposition. In order to measure the thickness of the deposited layer however, we already have the area of deposition (which is exactly the effective porosity), and we want to achieve the thickness of each layer. In other words, once we know the effective surface deposited, an estimate of the total volume deposited will enable us to find the average thickness of the wires. As we explain in the next section how to measure the deposited charge for each layer, we can use effective porosity and consumed charge in order to calculate the thickness. In the following we have done this measurement for one of our samples to see how accurately we can estimate the thickness of each layer. In Section 3.6, we show some SEM images to compare our estimation with reality. However, before we go ahead, let us explain a new challenge for which we do not presently have a solution. During the deposition process, some pores get blocked and no longer contribute to the deposition. As a result, we are depositing the same amount of charge into fewer pores. Therefore, we can expect to observe some increase in deposited layers as we get closer to the top of the template. Here we ignore this phenomenon ; however one can address this challenge in future projects by considering the dynamic number of pores which are contributing to the deposition process.
Fig. 3.21 shows the amount of charge which was deposited for a few layers in a Ni/Cu nanowire sample. In this sample, the average amount of charge which was deposited for each layer is 0.825 μC and 2.450 μC for Cu and Ni respectively.

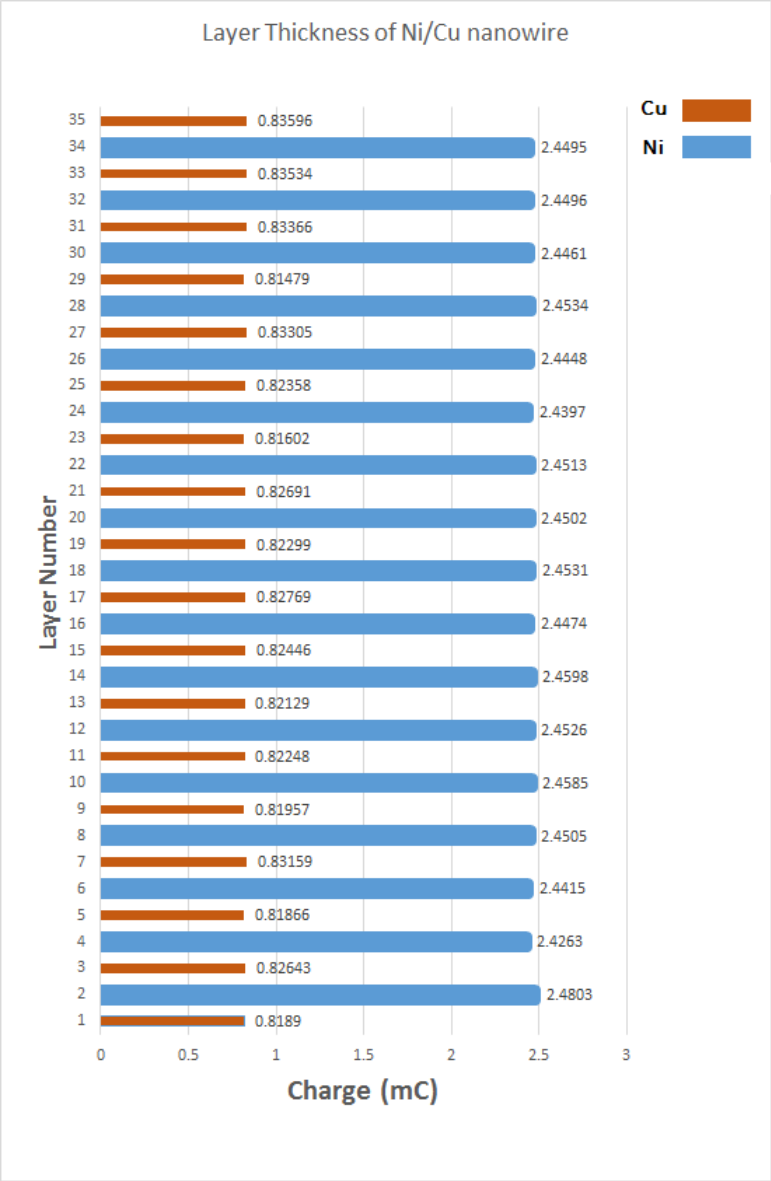

Figure 3.21 amount of charge which was deposited for each layer in a Ni/Cu nanowire sample.

therefore, using equation 3.14 one can calculate the thickness of Cu and Ni as follow :

$$d_{cu} = \frac{36.7}{0.825 \text{ mC} \times 3.146 \text{ mm}} = 9.62 \text{ nm}$$
$$d_{ni} = \frac{34.17}{2.45 \text{ mC} \times 3.146 \text{ mm}} = 26.66 \text{ nm}$$

In section 3.6 we have shown an SEM image for this sample and compared these results with the real thickness of each layer. Please note that we set the charge based on desired layer

thickness. However, in reality due to a small amount of time which takes for the instrument to switch the voltage (and reach the desired voltage from one to another) there is always a small amount of unwanted charge being deposited. In this sample for example, our desired thickness was 10 nm for Cu and 25 nm for Ni. However, in practice, we observe slightly different amount of charge during the experiment for the reason mentioned above.

3.6 Experimental results for controlling the layer thickness

In the work of Akhtari-Zavareh *et al.*, 2014, the thickness of each layer was controlled based on some growth rate of a thin film with the same material. However, we saw that growth rate depends on too many factors, such as the concentration of the electrolyte, the applied voltage, the cell size, pore diameter, aspect ratio and most importantly the porosity factor. Therefore, a pre-assumed growth rate is likely too far from the actual growth rate. In fact, the best way to control the layer thickness is to control the thickness in situ. As we explained above, coulometry will do this by counting the deposited charges while we are depositing. However, as we discussed above, this method has its own limitations as well. The most challenging issue, is that, as we progress in deposition, some pores may get blocked (mostly due to formation of hydrogen bubbles we believe or might be due to contamination in our electrolyte which can be eliminated if we perform the fabrication in a clean room environment) and therefore we will be depositing in fewer pores than expected and an underestimate of layer thickness. This will result in thicker layers as we get closer to the top of the template. Here, we have ignored this source of error.

In section 3.5 we calculated the layer thickness of one of our samples, i. e. Ni (26 nm)/Cu (10 nm), based on our coulometry model. Here we have provided some SEM of the same sample to see how accurate we have been able to predict the thickness of each layer. The recorded data of our experimental setup was provided in section 3.5. Fig. 3.22 shows an SEM image from this sample. In this image, the darker area corresponds to copper and the brighter area corresponds to Ni. Unfortunately we do not have an image of the top area of the template to see if the layer thickness is actually increasing as we get closer to the top. This image was taken from the bottom of the template. As one can see, our prediction for layer thickness is close to the real thickness of the layers. In fact, we expected the Cu layers to be 9.6 nm and Ni layers to be 26.6 nm based on the observed electrical charge that we have deposited. Here we see Cu layer thickness ranges from 10 to 20 nm with an average thickness of around 14 nm. We think that the Cu with 20 nm thickness is due to the formation of hydrogen bubbles which has prevented the next Ni layer to be deposited resulting in two layers of Cu which is close to 20 nm. The Ni layer thickness on the other hand is closer to what we expected with

an average thickness of around 25 nm. The average layer thicknesses were calculated based on Fig. 3.22. As we discussed earlier we expect a little bit more mismatch near the top of the sample.

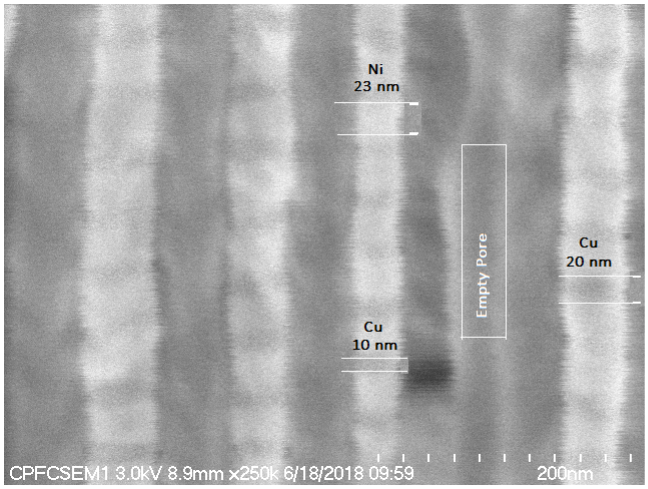

Figure 3.22 Layer thickness of each layer of a Ni(26 nm)/Cu(10 nm) sample. The dark area corresponds to Cu and the bright area corresponds to Ni for each wire. The thickness prediction based on our coulometry model, is very close to the observed thickness in this SEM.

CHAPTER 4 MODIFIED MEAN FIELD MODEL

4.1 Introduction

Mean field theory studies a complicated and high interactive many body system by reducing the degrees of freedom so that one can treat the system as a lower dimensional or even one body system. The main idea is to replace the interaction of all particles with an average for a given particle of the system. This idea was first introduced by Pierre Weiss in 1907 (Weiss, 1907). He originally developed this idea in order to be able to explain ferromagnetism. Since we are replacing all interactions of all particles of the system with an average interaction, this is sometimes called effective interaction. In the following, we adopt this approach in order to develop a mean field model to explain the magnetic anisotropy of an array of ferromagnetic/nonmagnetic multilayer nanowire system.

Magnetic anisotropy describes how the magnetization of a system reacts to an applied field. In an isotropic system, the magnetization reacts the same way no matter in which direction the external field is applied. In an anisotropic system, there is a preferred axis (or preferred axes). The magnetization tends to align parallel to these axes. Any deviation from the easy axis will increase the energy of the system. One can consider this as a measure of magnetic hardness of the material (Coey, 2010).

Magnetic anisotropy is one of the most important parameters that characterize a ferromagnetic material, along with other properties such as Curie temperature, coercivity, saturation field, saturation magnetization and remanent magnetization . In technology for example, depending on the type of application, materials with high, medium or low anisotropy are required in permanent magnets, information storage media and magnetic recording heads respectively. The behavior of magnetic properties is quite different in bulk materials and nano scale materials. In magnetic multilayer nanowires it is possible to tailor the magnetic anisotropy by varying the thickness of the magnetic and non-magnetic layers or by choosing different materials along the wire. This is an extra degree of freedom, compared with bulk materials (Sun *et al.*, 2005). Magnetic anisotropy may result from crystallographic structure, mechanical stress or shape anisotropy. The shape anisotropy, or equivalently, the dipolar anisotropy, which is the focus of this chapter, is due to magnetic dipole interaction within a specimen. This interaction is long range and depends on the shape of the sample. It is the dominant contribution in multilayer nanowires, in which magnetocrystalline and surface anisotropy can be neglected (Bland, 2002). This is often the case for Fe or Ni based soft magnetic alloys, but not so much in hard materials such as pure Co. For example, the crystal

anisotropy is in the range of $10^3 \sim 10^4$ erg/cm^3 for Ni nanowires while the shape anisotropy is in the range of $10^5 \sim 10^6$ erg/cm^3. However, in the case of Co nanowires the crystal anisotropy will compete with shape anisotropy (Fert and Piraux, 1999). The only case where it does not dominate in soft materials is a spherical assembly of spherical particles, because the shape anisotropy due to dipolar interactions is isotropic

In previous studies, in order to describe the anisotropy in arrays of multilayer nanowires, an effective field model based on a simple mean field approach was developed (Carignan *et al.*, 2007). The key ideas of this model are developped in Section 4.3. We will refer to it hereafter as "effective field model". However, it fails to describe the observed anisotropy of multilayer nanowires. One reason for this, as it was later found, was that the thicknesses and the stochiometries of the magnetic layers were different from what had been assumed (Akhtari-Zavareh *et al.*, 2014). Another factor was that the effect of nearest neighbor disks was not considered explicitly in the effective field model. Further, the nature of the nanowire deposition process results in arrays of multilayer nanowires with variable lengths inside an alumina template. This has an influence on the effective field which was not considered in the effective field model. There are also other parameters which can affect the effective field in an array of multilayer nanowires such as non uniform distribution[1] of magnetic dipoles and the effect of roughness of the interface of magnetic and non-magnetic layers. These were also neglected in the effective field model. Here we address the contribution of nearest neighbor interaction and multiple length distribution. One can further study the effect of vortex distribution and roughness of interfaces between magnetic and non-magnetic layers to improve the current effective field model.

In what follows, we first introduce the effective field model based on the simple mean field model as developed in Carignan *et al.* (2007) and Carignan (2012). Then we explain the modifications, i.e. the nearest neighbor dipolar interaction, which has been applied to assess the importance of that effect and possibly improve the effective field model.

4.2 Some aspects of magnetic anisotropy

The Weiss molecular field theory of ferromagnetism explains the magnetic domains in which the magnetic dipoles are aligned when a sample is cooled below the Currie temperature. Heisenberg considered the origin of the Weiss molecular field by introducing the quantum

1. See section 4.4.2

mechanical concept of exchange interaction. This term basically is due to the overlapping of wave functions of adjacent atoms and is given by

$$\epsilon_{ex} = -2\boldsymbol{A}_{ij}\vec{S}_i\vec{S}_j \tag{4.1}$$

where $\vec{S}_i$ and $\vec{S}_j$ are the electron spin and A_{ij} is the exchange constant which determines the strength of the exchange interaction. In ferromagnetic materials the exchange constant is positive and large which tends to make the spins parallel to each other to minimize the exchange energy.

Another factor for magnetization is the crystallographic property of a material which dictates a specific direction in which the magnetic moments tend to align. This will introduce a term in anisotropy energy called crystalline anisotropy energy. For example in cubic structures, either the <100> or <111> directions will be the easy axes. Any deviation of magnetization direction from the easy axis requires energy which increases the total free energy of the system.

The third term which plays an important role, is the magnetostatic (demagnetizing) energy. This energy, which arises from dipole-dipole interactions, describes the dependency of the total free energy on the direction of magnetization with respect to the shape of the sample. In general, the magnetic field inside the object is in the direction opposite to the magnetization which creates that field, and is therefore called the demagnetizing field which is proportional to the magnetization with a so called demagnetizing factor, namely :

$$H_d = -N_d M \tag{4.2}$$

where N_d is the demagnetizing factor. Since N_d depends on the shape of the object, this magnetic anisotropy is called shape anisotropy.

In addition to the three terms mentioned above, the magnetic total free energy can have additional terms in general, such as a magnetoelastic or surface anisotropy terms. However, those three terms mentioned above are usually leading terms in ferromagnetic materials especially when there is no external or local stress. The exchange term tends to align each spin parallel within a nanowire, whereas the magnetocrystalline anisotropy fixes this direction along certain crystallographic axis. Polycrystallinity, if present, can thus introduce some local fluctuations in the magnetic anisotropy. The shape anisotropy favors the direction of magnetization parallel to the axis of long nanowires, however the interwire dipolar interaction, where the lateral dimensions of the arrays are large compared to their thickness, will upset this trend and favor in-plane alignment of the magnetization. As discussed in Section 4.3, where we develop an effective field model in order to explain the magnetic anisotropy

of the multilayer nanowires, we will see that the shape anisotropy, which results from the dipole-dipole interaction, plays the major role in determining the magnetic anisotropy of the multilayer nanowires. In Section 4.3, we first calculate the effective field based on a simple effective field model by calculating the demagnetizing factor for the system, assuming that we can approximate the magnetic disks as oblate ellipsoids, and then explicitly include the contribution of the dipole-dipole interaction for the nearest neighbors of magnetic layers within a multilayer nanowire.

4.3 The simple effective field model

This simple model explains the magnetic anisotropy for arrays of uniformly magnetized magnetic nanowires and for arrays of multilayer magnetic-nonmagnetic nanowires. Throughout the rest of this chapter, we have assumed that our samples are submitted to a strong enough external field, so that we can assume the magnetization is always saturated in one direction. In the case of multilayer nanowires, it is expected to work relatively well when the spacers (non-magnetic layers) are thick enough, and magnetic layers thin enough, so that we can treat each magnetic layer as a single magnetic dipole (a mean field approach). However, it is expected to fail in explaining the effective anisotropy field for samples with very thin spacer layers. This is because the nearest neighbor interaction is quite inhomogeneous over adjacent magnetic disks. We will see in this chapter that after taking into account of 5 nearest neighbor magnetic disks, both models approach to the same results. Apparently, number of nearest neighbors to be taken into account depends on the thickness of each layer. According to our simulation results, we can conclude that the mean field approach suffices after about a range of 150 nm or higher.

The geometry of the nanowire system is shown in Figure 4.1, for multilayer nanowires. Homogeneous nanowires can still be considered as multilayered, where all layers have the same composition. The main problem is to calculate the total effective field applied to each single magnetic disc within each wire. This total field includes the applied external field and the magnetostatic interaction field. The dipolar interaction can be separated into interwire and intrawire parts and the intrawire interaction can be further separated into the demagnetizing field of the single layers and the intrawire interaction between layer. We can write the

magnetic field produced at $\vec{r_j}$ by a magnetic dipole located at $\vec{r_i}$ as :

$$\begin{aligned}\mathbf{B}_i(\mathbf{r_j}) &= \frac{\mu_0}{4\pi R_{ij}^5}\left[3\left(\boldsymbol{m}_i \cdot \boldsymbol{R}_{ij}\right)\boldsymbol{R}_{ij} - R_{ij}^2 \boldsymbol{m}_i\right] \\ &= -\mu_0 \overline{\mathbf{N}}_{ij}\mathbf{M}_i \end{aligned} \tag{4.3}$$

In equation 4.3, μ_0 is the vacuum permeability, $\boldsymbol{m}_i$ is the magnetic moment which can be

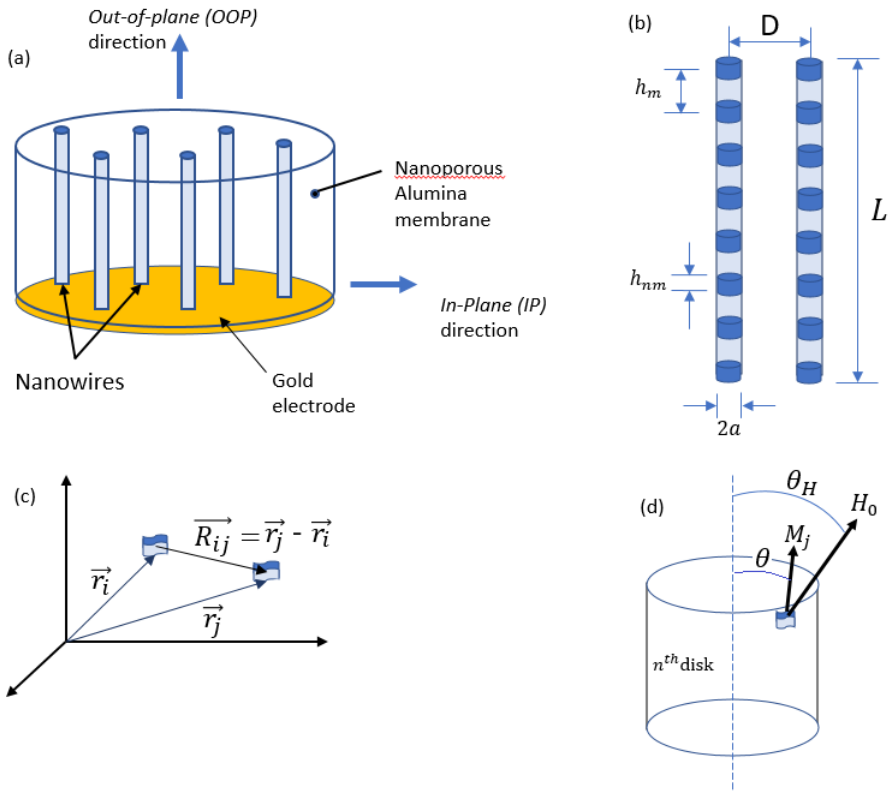

Figure 4.1 (a) the whole system (b) definition of the geometric parameters (c) two arbitrary dipoles at $\vec{r_i}$ and $\vec{r_j}$ located at $\mathrm{k_{th}}$ and $\mathrm{n_{th}}$ disks respectively (disks are not shown in this image) (d) large image of the $\mathrm{n_{th}}$ disk and the definition of θ and θ_H.

written as $\mathbf{M}_i V_i$ where V_i is the volume associated with dipole i and $\mathbf{R}_{ij}$ is defined as (see Figure 4.1) :

$$\mathbf{R}_{ij} = \mathbf{r_j} - \mathbf{r_i} = (X_{ij}, Y_{ij}, Z_{ij}) = (x_j - x_i, y_j - y_i, z_j - z_i) \tag{4.4}$$

and $\overline{\mathbf{N}}_{ij}$, dipolar interaction tensor, is defined as :

$$\overline{\mathbf{N}}_{ij} = \frac{V_j}{4\pi R_{ij}^5} \begin{pmatrix} R_{ij}^2 - 3X_{ij}^2 & -3Y_{ij}X_{ij} & -3Z_{ij}X_{ij} \\ -3X_{ij}Y_{ij} & R_{ij}^2 - 3Y_{ij}^2 & -3Z_{ij}Y_{ij} \\ -3X_{ij}Z_{ij} & -3Y_{ij}Z_{ij} & R_{ij}^2 - 3Z_{ij}^2 \end{pmatrix} \tag{4.5}$$

Using equation 4.3, one can sum up all $\vec{m_i}$ to obtain the total field at $\vec{r_j}$:

$$\mathbf{B}(\mathbf{r_j}) = \sum_{i \neq j} \mathbf{B}_i(\mathbf{r_j}) = -\mu_0 \overline{\mathbf{N}}_j \mathbf{M}_j \tag{4.6}$$

where summation is over all dipoles except the $\mathrm{j_{th}}$ dipole at point $\vec{r_j}$ and $\overline{\mathbf{N}_j}$ is the total effective demagnetizing tensor.

We need to calculate the effective demagnetizing tensor, $\overline{\mathbf{N}}_j$, which in its most general form it can be written as :

$$\overline{\mathbf{N}}_j = \sum_{i \neq j} \overline{\mathbf{N}}_{ij} \tag{4.7}$$

In principle, it is possible to consider all mutual interactions between all elementary dipoles in the whole system to obtain the total dipolar energy. However, this requires the exact vectorial distribution of all elementary dipoles. In fact we have shown that using the OOMMF (Object Oriented Micro Magnetic Framework) software, it is possible to simulate this anticipated distribution. However, this requires a super computer as there are millions of nanowires in an array with hundreds of disk in each wire. Assuming the cell size of each dipole in our simulation is $5 \times 5 \times 5\mathrm{nm}^3$, we are dealing with trillions of dipoles and for each pair of dipoles we are solving an integral. Moreover, the calculated dipolar field would depend on the location of the observation point r_j, and will thus vary both along the wire and across the array. Therefore, in the simplified effective field model proposed in Carignan *et al.* (2007) some simplifications were made :

1. We consider only the field at the central point of the central disc of the central nanowire. In other words, the k_{th} disc in Fig 4.1 is the center of the array. This simplification is justified in laterally infinite sample and long nanowires so that we can assume the interaction field along the nanowire is uniform.
2. We approximate this central field to be the average uniform field everywhere in the array. This simplification is also justified in the same conditions as simplification no. 1.
3. The self demagnetizing field of the central disc is treated as the uniform demagnetizing field of an equivalent ellipsoid. This simplification is justified in very flat or very elongated ellipsoids (very small or very high aspect ratio).

4. Magnetic anisotropy is generally dominated by dipolar interactions (demagnetization fields) that is magnetocrystalline and magnetostrictive contributions are negligible. This simplification is justified in soft magnetic materials.
5. Surface anisotropy and interlayer exchange interaction are negligible. This simplification is justified if the spacer (non-magnetic layer) is not too thin.
6. The magnetization of every layer equals the average magnetization of the array (mean field approach). This simplification is justified if magnetic layers have the same stoichiometry and are uniformly magnetized.

A schematic view of above simplifications is shown schematically in Fig. 4.2.

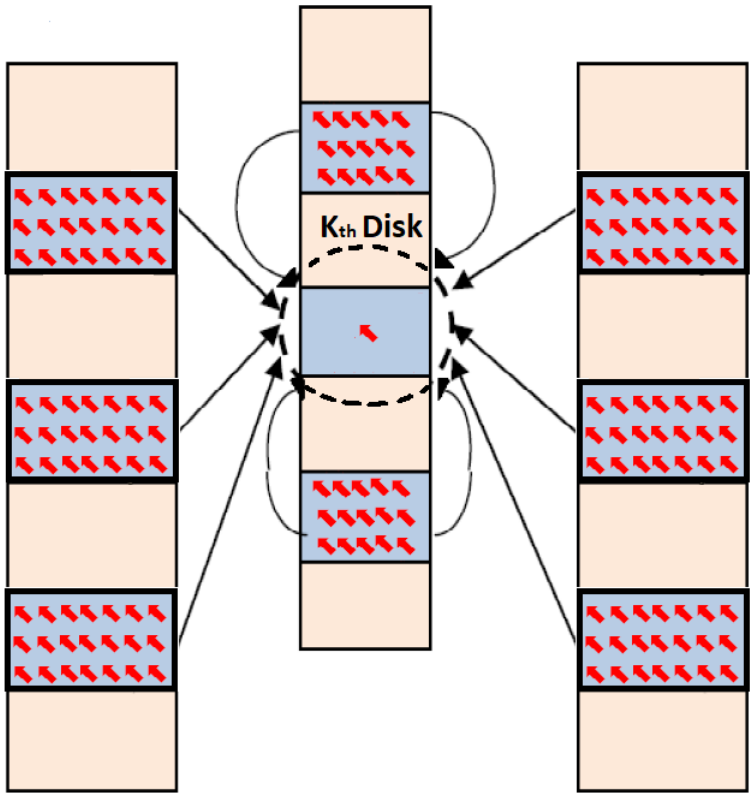

Figure 4.2 Mean field approach for the entire system of multilayer nanowires. Here the magnetic field of all dipoles is calculated at the center of the central disk and it is assumed that all other magnetic layers experience the same field. This is equivalent to assuming that the interaction field along the nanowire axis is uniform and the lateral dimensions of the array are infinite.

Replacing the summation over each disk by volume integration, it is possible to transform the dipolar field in terms of a sum of contributions of the central disk, N_d, the other disks of

the central wire, N_{intra} and the disks of the the other wires, N_{inter}. Within this scheme, the total demagnetizing tensor at $\mathbf{r}_j = 0$ can be written :

$$\overline{\mathbf{N}}_j = \overline{\mathbf{N}}_d + \overline{\mathbf{N}}_{intra} + \overline{\mathbf{N}}_{inter} \tag{4.8}$$

In equation 4.8, we highlighted the term which is related to the shape demagnetization of the dipolar volume at $\mathbf{r}_j$. If we treat the central disk as an ellipsoid we can write the demagnetizing tensor as :

$$\overline{\mathbf{N}}_d = \begin{pmatrix} N_{ip} & 0 & 0 \\ 0 & N_{ip} & 0 \\ 0 & 0 & N_{oop} \end{pmatrix} \tag{4.9}$$

where N_{ip} and N_{oop} are the in-plane(IP) and out-of-plane(OOP) shape demagnetizing factors of the disk (Osborn, 1945) and $2N_{ip} + N_{oop} = 1$. Equation 4.8 and 4.9 can be added together to obtain the total demagnetizing tensor. If we assume that the dipolar interaction field along the nanowire axis is uniform and the lateral dimensions of the array are infinite and r_j is implicitly 0 that is the center of the array (see Eq. 4.5 and Eq. 4.4), we can write the total demagnetizing tensor in diagonal form with constant components as follow (for details see Carignan *et al.* (2007)) :

$$\overline{\mathbf{N}} = \begin{pmatrix} \tilde{N}_{ip} & 0 & 0 \\ 0 & \tilde{N}_{ip} & 0 \\ 0 & 0 & \tilde{N}_{oop} \end{pmatrix} \tag{4.10}$$

where

$$\tilde{N}_{ip} = N_{ip} + \sum_{r_i} \frac{V(r_i^2 - 3x_i^2)}{4\pi r_i^5} \ (r_j = 0 \ \text{ at the center of the array}) \tag{4.11}$$

$$\tilde{N}_{oop} = N_{oop} + \sum_{r_i} \frac{V(r_i^2 - 3z_i^2)}{4\pi r_i^5} \ (r_j = 0 \ \text{ at the center of the array}) \tag{4.12}$$

Since the trace of equation 4.5 is null, we can still assume that $2\tilde{N}_{ip} + \tilde{N}_{oop} = 1$. This will reduce our problem to calculating $\tilde{N}_{oop}$ only. Hereafter, we focus on this. Considering the simplification no. 5 on page 65 , we can write the total magnetic field produced by the dipolar interaction at the center of the k_{th} disk as :

$$\mathbf{B} = -\mu_0 \overline{\mathbf{N}}\mathbf{M} = -\mu_0 \begin{pmatrix} \tilde{N}_{ip} & 0 & 0 \\ 0 & \tilde{N}_{ip} & 0 \\ 0 & 0 & \tilde{N}_{oop} \end{pmatrix} \mathbf{M} \tag{4.13}$$

Considering that this field can be obtained from the gradient of the energy density with

respect to **M**, the dipolar energy density may be written as :

$$U_{dipolar} = -\frac{1}{2}\mathbf{M}\cdot\mathbf{B} = \frac{\mu_0}{2}\mathbf{M}\cdot\overline{\mathbf{N}}\mathbf{M} \tag{4.14}$$

Now considering the simplifications no. 4 and no. 5 allows us to re-write equation 4.14 as :

$$\begin{aligned} U_{dipolar} &= \frac{\mu_0 M_s^2}{2}(\tilde{N}_{ip}\sin^2\theta + \tilde{N}_{oop}\cos^2\theta) \\ &= \frac{\mu_0 M_s^2}{4}(1-3\tilde{N}_{oop})\sin^2\theta + C \\ &= K\sin^2\theta + C \end{aligned} \tag{4.15}$$

Here M_s is the saturation magnetization. The point of this equation is that it has the form of uniaxial anisotropy in which we can define the effective field as :

$$H_{eff} = \frac{2K}{\mu_0 M_s} = \frac{M_s}{2}(1-3\tilde{N}_{oop}) \tag{4.16}$$

in which K is the effective anisotropy constant. From this equation we can see that an estimation of $\tilde{N}_{oop}$ will give us the effective field.

4.3.1 Estimation of the demagnetizing factor

In the case of multilayer nanowires, we can rewrite the total demagnetizing factor, $\tilde{N}_{oop}$, as three terms :

$$\tilde{N}_{oop} = N_{oop} + N_{inter} + N_{intra} \tag{4.17}$$

The right hand side of this equation includes the shape demagnetizing factor N_{oop}, the interwire demagnetizing factor N_{inter}, and the intrawire demagnetizing factor N_{intra}. If we treat the k_{th} disk as an oblate ellipsoid ($c' = h_m/2a \ll 1$ in 4.1) the shape demagnetizing N_{oop} is well approximated by :

$$N_{oop} = 1 - \frac{\pi}{2}c' + 2c'^2 \tag{4.18}$$

By evaluating the sum in equation 4.12 when $x_i^2 + y_i^2 \neq 0$ and the k_{th} disk is in the middle of the central nanowire, it can be shown (Carignan *et al.*, 2007) that the interwire demagnetizing factor N_{inter} can be approximated by :

$$N_{inter} = fP\sum_{m=1}^{\infty}\frac{ms}{(m^2+s^2)^{3/2}} = fP \tag{4.19}$$

Where $f = h_m/h$ and P is the filling factor (porosity) discussed in section 3.4, which is calculated separately by considering the occupied surface by wires in alumina template and $s = L/2D$ is the normalized length. The summation in equation 4.19 is equal to 1 (Carignan *et al.*, 2007).
Finally, the intrawire demagnetizing factor N_{intra} can be also calculated by evaluating the sum in equation 4.12 for $x_i^2 + y_i^2 = 0$ and when the k_{th} disk is in the middle of the nanowire. This can be approximated by (Carignan *et al.*, 2007) :

$$N_{intra} \approx -f + 2c^{'} \tag{4.20}$$

Therefore, for thin disks ($c^{'} \ll 1$) and long wires we can rewrite the total demagnetizing factor $\tilde{N}_{oop} \approx 1 - f(1 - P)$ and so the effective field is approximated as :

$$H_{eff} = \frac{M_s}{2}\{1 - 3[1 - f(1 - P)]\} \tag{4.21}$$

This last formula shows that by adjusting the ratio of magnetic to non-magnetic layer thickness, that is h_m/h_{nm}, it is possible to adjust the magnetic anisotropy and have easy axis or easy plane depending on whether the $\tilde{N}_{oop} < 1/3$ or $\tilde{N}_{oop} > 1/3$ respectively.

In Carignan *et al.* (2007) it is shown that some discrepancies between this effective field model and experimental results arise particularly for samples with low h/a ratio. This could be because of simplification no. 3. We know that the nearest neighbor dipolar interaction is quite inhomogeneous over the middle disk when the magnetic layers are fairly close to each other (spacer layers are very thin).
In the next section, we have taken into account the effect of the nearest neighbor dipolar interaction explicitly. This can improve the results presented in Carignan *et al.* (2007).

4.4 Nearest neighbor model

An important limitation of the effective field model is the lack of averaging over the space dependent dipolar fields due to the nearest dipoles. The effect of the nearest neighbors in our modified mean field model will now be accounted for more rigorously. Hereafter, we refer to our modified effective field model as nearest neighbor mean field model (or NNMF model for short). This modification is based on the Oguchi model, an improvement of the Weiss mean field model (Smart, 1966; Oguchi, 1955). Briefly, Oguchi considered the hamiltonian for the nearest neighbor interactions of the many body system exactly and treated the remainder of the system within the mean field model as Weiss did. Using this method, he was able

to better explain the specific heat of ferromagnets. In principle,using eqs 4.1 and 4.2, one can take into account all interactions between all dipoles in the system. However, in a large and complicated system such as multilayer nanowires, this will lead us to an unmanageable problem. Therefore, in what follows, we will keep the assumption of the rigid magnetization and treat the far-away dipoles in a mean field approach, as before, but we will explicitly consider the dipolar interaction between nearest-neigbors in a small volume surrounding the point of interest. To do so, we first assume that the middle disk in the central wire and its nearest neighbors magnetic layers are made of small magnetic dipoles in a rigid magnetization distribution, that is, all dipoles are parallel. In section 4.4.2 we describe how we can even improve the nearest neighbor interaction by considering non-uniform distribution of dipoles within a magnetic disk. However, the detailed result is not presented in this thesis and might be considered as future work. The interaction of all other magnetic layers including interwire and intrawire interactions, is treated using the mean field model.

4.4.1 Estimation of the effective field

Here, we assume that all dipoles are rigidly aligned, meaning that magnetization is uniform in amplitude and orientation throughout the array. The geometry of this problem is displayed schematically in figure 4.3. We consider three neighboring disks. The middle one is located at the origin of our coordinate system. The goal is to calculate the magnetic field produced by each dipole of the top, bottom and the middle disk itself, over the entire volume of the middle disk and then average this field over the middle disk. To achieve this goal, we first divide the uniformly magnetized disks into cells (in a cubic shape) of volume V, each cell associated with a central point dipole $m = MV$, where M is the mean magnetization. We then calculate the field produced by a single dipole located inside the top disk and repeat this calculation and sum over all the dipoles of the top, bottom and the middle disk. The number of dipoles we take into account depends on the cell size of our numerical calculation code. The smaller the cell size (higher resolution), the more time needed for the calculation. A typical cell size is $5 \times 5 \times 5$ nm^3 for each magnetic dipole.

The total field at position $\vec{r_j}$ in the k_{th} (middle) layer is :

$$\mathbf{B}(\mathbf{r}_j) = -\mu_0 \overline{\mathbf{N}}_j \mathbf{M}_j + \mathbf{B}_{MF}(\mathbf{r}_j) \tag{4.22}$$

where $\overline{\mathbf{N}}_j$ is given by equation 4.7 for which the summation $\sum_i$ runs over all $\vec{r_i}$ for the middle and a number of nearest neighbor layers. The $\mathbf{B}_{MF}$ is the contribution of all other layers as calculated by the mean field approach, without including the contribution of nearest neighbor already included and the self-demagnetizing contribution. Then, the new mean field

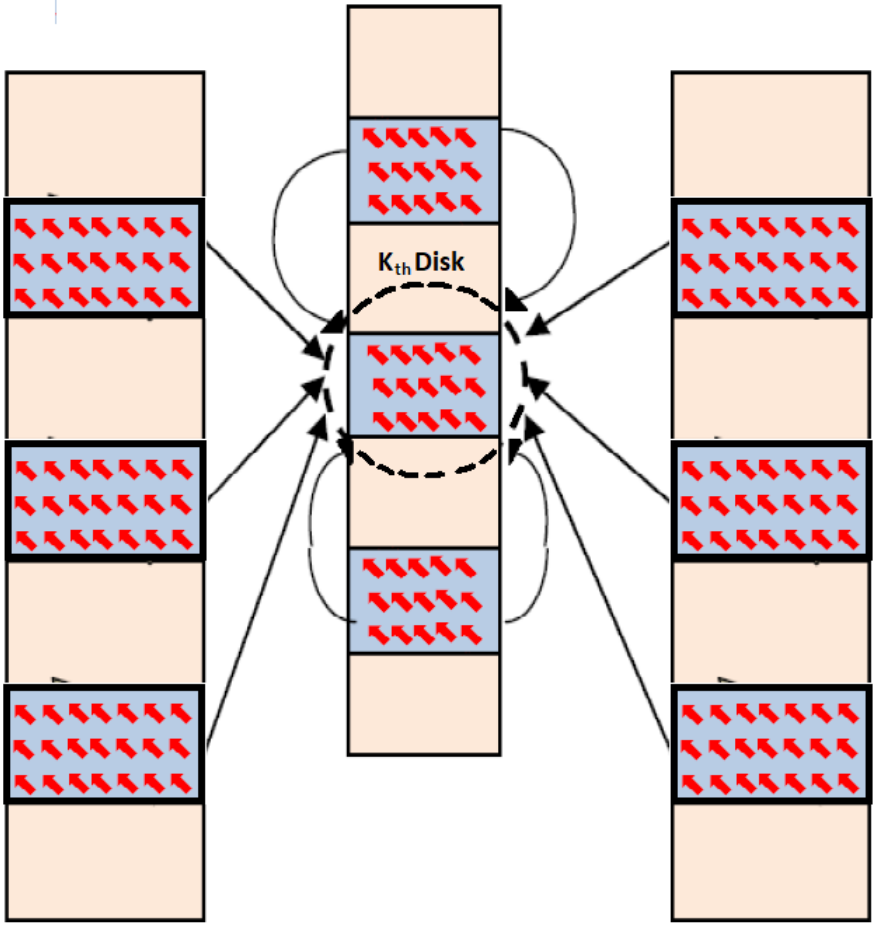

Figure 4.3 Schematic view of NNMF model. In this model, all interactions are considered as mean field interaction except for the interaction of nearest neighbors of the k_{th} disk at the middle of the central wire. The interactions of all single dipoles from nearest neighbor layers are included explicitly in this model.

is obtained by averaging over the k_{th} (middle) layer as :

$$\mathbf{B} = \frac{1}{N_{cell}} \sum_{\mathbf{r}_j \in \text{ middle disk}} \mathbf{B}(\mathbf{r}_j) \tag{4.23}$$

where N_{cell} is the number of dipoles in the k_{th} layer.

In what follows, we adopt a slightly different notation well adapted to the numerical coding of the calculation. In this new notation, the magnetic field of a magnetic dipole located at the origin of the coordinate system can be written as :

$$\mathbf{B}_{dip}(x,y,z) = \begin{cases} B_x = 3Cx(y\sin\theta + z\cos\theta) \\ B_y = C[(2y^2 - x^2 - z^2)\sin\theta + 3yz\cos\theta] \\ B_z = C[(2z^2 - x^2 - y^2)\cos\theta + 3yz\sin\theta] \end{cases} \tag{4.24}$$

where $C = \frac{\mu_0 m}{4\pi r^5}$ and $r^5 = (x^2+y^2+z^2)^{5/2}$. This is the field produced by a magnetic dipole located at the center of the coordinate system with angle θ from Z axis in Y-Z plane in Cartesian system as illustrated in figure 4.4.

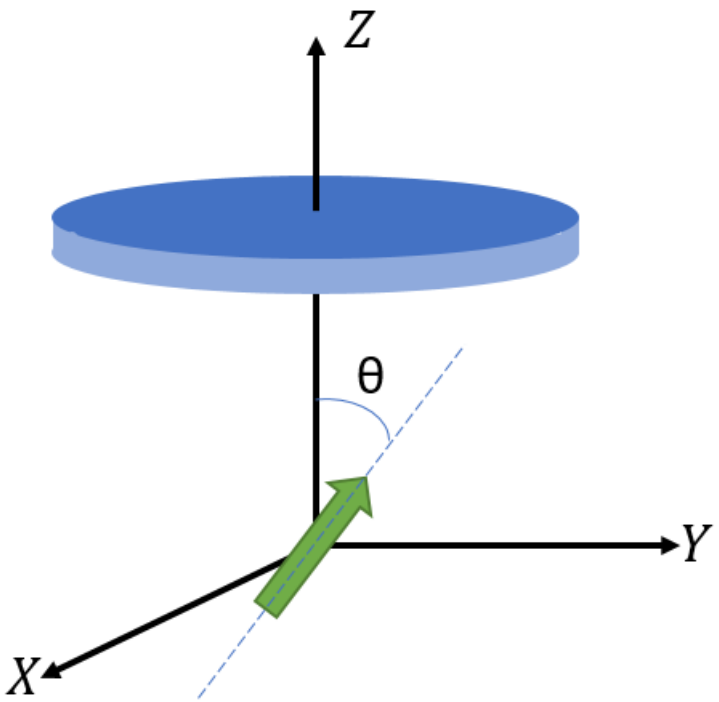

Figure 4.4 The geometry related to the calculated field in equation 4.24. We can integrate the B field over the entire volume of the above disk to calculate the average field.

In Fig. 4.5, we have shown schematically how the nearest neighbor (NN) contribution has been calculated in mean field model. In fact, the mean field calculates the B field of all dipoles from all disks (including NN disks) only at the center of the target (k_{th}) disk while in NNMF model we have expanded the calculation over the entire of the target disk (rather than only the central point) for NN magnetic disks. The analytical B field for the NN contribution in mean field can be obtained by equation 4.25. This can be derived from Eq. (26) of Carignan *et al.* (2007) when we carry the sum over n for -1 and +1 that is the first NN neighbors only.

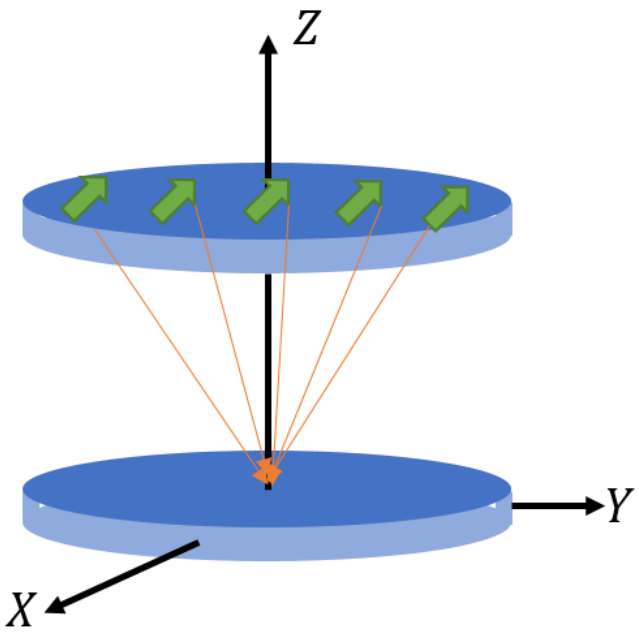

Figure 4.5 Schematic view of how B field is calculated from one disk (here an NN disk) over the target disk which is located at the origin of the coordinate system. The B field of all dipoles are considered only at the center of the target disk.

$$\langle B_{nnx}\rangle = 0$$

$$\langle B_{nny}\rangle = \frac{\mu_0 M}{2}\sin(\theta)\left[\frac{\frac{3h_m}{2}+h_n}{\left(a^2+\left(\frac{3h_m}{2}+h_n\right)^2\right)^{1/2}} - \frac{\frac{h_m}{2}+h_n}{\left(a^2+\left(\frac{h_m}{2}+h_n\right)^2\right)^{1/2}}\right]$$

$$\langle B_{nnz}\rangle = -\mu_0 M\cos(\theta)\left[\frac{\frac{3h_m}{2}+h_n}{\left(a^2+\left(\frac{3h_m}{2}+h_n\right)^2\right)^{1/2}} - \frac{\frac{h_m}{2}+h_n}{\left(a^2+\left(\frac{h_m}{2}+h_n\right)^2\right)^{1/2}}\right] \tag{4.25}$$

There is no analytical solution for the averaged B field when we consider all points over the target disk. As expected, there is no net field component perpendicular to the plane of rotation of the average magnetization due to the symmetry of the problem. We also note that $2\langle B_{nny}\rangle = -\langle B_{nnz}\rangle \tan\theta$.

By calculating the B field using equation 4.24 for all dipoles inside the nearest neighbor disks (that is top, bottom and the middle disk), we will have the B field produced by all dipoles which are located inside the nearest neighbor disk over the k_{th} disk. We have plotted the B

field produced by a disk at the center of the neighbor disk versus the angle of the dipoles in figure 4.6 using equation 4.25 to see the behaviour of the field. As expected, when all dipoles are pointing to the Z direction we have maximum value for B_z component and B_y is zero due to the symmetry of the geometry of the problem. When all dipoles align in Y direction the B_z component vanishes and B_y is maximized. B_x is always zero since we have assumed dipoles to be in Y-Z plane.

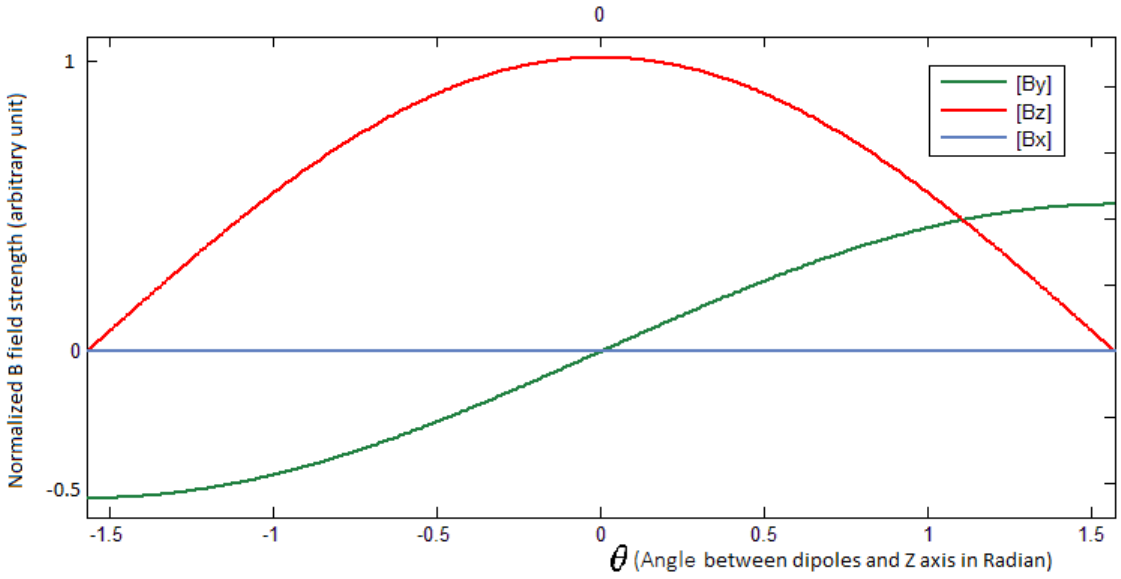

Figure 4.6 The B field produced by all dipoles from one disk over the neighboring disk, from equation 4.25.

Appendix A presents the MATLAB code that has been used to compute the calculation presented above. Once we have the B field over the k_{th} disk produced by its two nearest magnetic neighbors and the self-demagnetizing contribution, we can calculate the averaged magnetic energy density for this tri-layer system (that is the k_{th} disk and its two nearest neighbors) using $U_{dipolar} = -1/2\mathbf{M} \cdot \mathbf{B}$. Figure 4.7 shows the total dipolar magnetic energy density of the system for different angles of dipoles rotating from $-\pi/2$ to $+\pi/2$ with respect to Z axis (wire axis). In Fig. 4.7, the total energy density of this tri-layer system was calculated using the dipolar contribution of the neighboring dipoles as just described, to which we added the contribution of the remaining dipoles using the effective field model of Carignan *et al.* (2007). This mean field contribution was obtained by exactly the same process as explained in section 4.3.1 except we have excluded the contribution of nearest neighbors, given by equation 4.25, while calculating the N_{intra} in equation 4.20 namely in Eq. (26) of Carignan *et al.* (2007) the

summation is carried for n from $-(N-1)/2$ to -2 and then $+2$ to $(N-1)/2$ so that we do not consider the mean field nearest neighbors contribution ($n=-1$ is the nearest magnetic disk below the k_{th} disk and $n=+1$ is the disk above the k_{th} disk and N is the total number of disks in a wire). Note that for 1-2 NN[2] contribution (Table 4.1) we have excluded 1-2 NN from mean field approach by carrying the sum over n from $-(N-1)/2$ to -3 and then $+3$ to $(N-1)/2$. The same process has been done for 1-3 NN contributions and 1-5 NN contributions. Also, the self demagnetizing field contribution which is shown in equation 4.18 has been excluded, since it is already accounted for in our calculation. This is to make sure that we do not consider the effect of NNs and self demagnetization field (which is due to the shape) twice in NNMF model. Once we have the new N_{intra} excluding the contributions of nearest neighbors and self demagnetizing field, we can calculate the H_{eff} using equation 4.21 and K from equation 4.16 to which we add the result of our calculation in order to obtain corrected values for K and H_{eff}. The results are reported in Table 4.1. Note that these results are for a specific sample with 500 magnetic and non-magnetic layers with 20 nm and 10 nm respectively. We use the notation 500(Ni20/Cu10) to show these geometrical features. The diameter of wires, $2a$, is 170 nm. In order to calculated the self demagnetization field, equation 4.18 was used both in this thesis and in Carignan *et al.* (2007). Also, in this paper it was assumed the magnetic disk are oblate enough so we can ignore the $c^{''} = h_m/2a$ and just replace the self demagnetization factor with 1 (as equation 4.18 suggests). We have followed the same assumption in this thesis. However, one can use the full equation for the self demagnetization (namely Eq. (20) in Carignan *et al.* (2007)) to be more accurate. The full self demagnetization equation was introduced by Osborn (1945).

Fitting the data in Fig. 4.7 with equation 4.15 yields an effective anisotropy constant $K = 9255(J/m^3)$. After replacing this number, which is the total contribution of the tri-layer system calculated numerically, with the MF contribution of the tri-layer system, as explained above, the effective anisotropy field is changed from -620 Oe (62 mT) to -261 Oe (26.1 mT). Considering only the first nearest neighbors yields a considerable change in predicted effective field for a sample with thin non-magnetic (spacer) layer. We have also extended the contribution of neighbors up to 5 nearest neighbor disks which results in changing the effective field to $+99$ Oe. However, from the 6_{th} neighbors we did not see any further change. A summary of all results for sample 500 (Ni20/Cu10) is presented in table 4.1.

2. we have used the notation 1-x NN to show 1 to x nearest neighbor magnetic disks. For example, 1-3 NN means 3 magnetic disks above the target disk and 3 magnetic disks below the target disk. For a review of geometrical definitions see Sec.1.1 and .

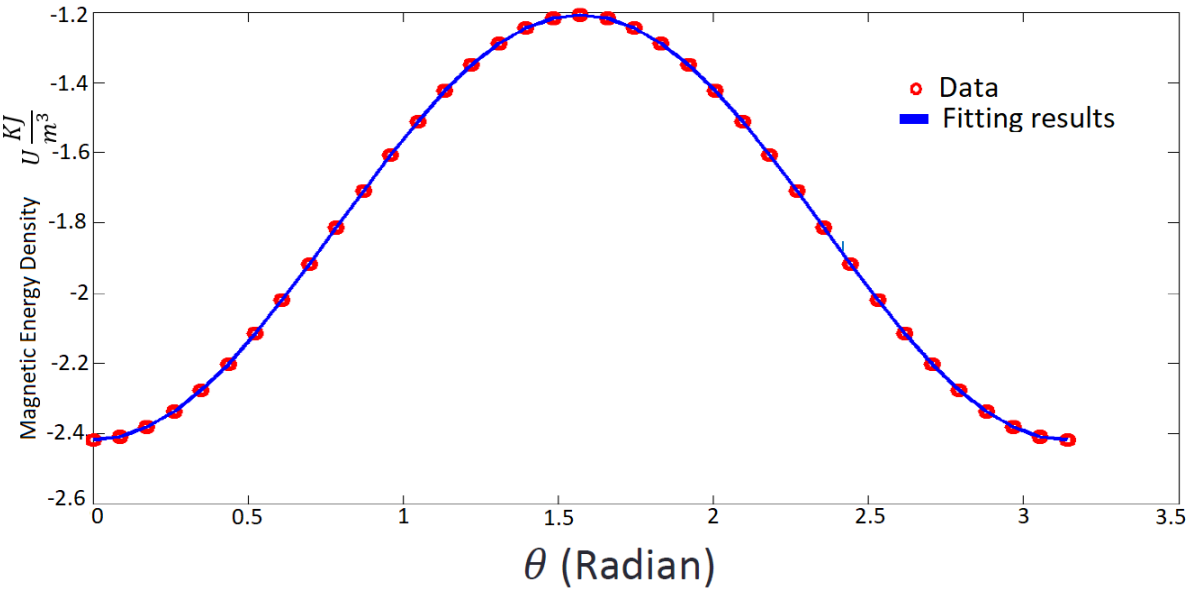

Figure 4.7 Magnetic energy density as a function of θ (angle between dipoles and wire axis) for the sample 500(Ni20/Cu10) introduced in reference (Carignan *et al.*, 2007). Red circles are calculated data from the code (Appendix A) and the blue curve is the fitting result using equation 4.15 to obtain anisotropy constant K.

In order to better understand these result we have also plotted the normalized effective field vs the magnetic to non-magnetic thickness ratio in figure 4.8 for the effective field model (without considering the contribution of nearest neighbors) and for the contribution of the first five neighboring disks. As we can see, for the sample 500(Ni20/Cu10) which is matched with $h_m/h_{nm} = \frac{20}{10} = 2$ in this figure. Including first to fifth neighboring disks, the effective field is changed from -620 to $+99$ (the cyan line). Here the saturation magnetization is assumed to be 460 emu/cm^3. As one can notice in this example, the effective field has changed its sign from negative to positive when we use NNMF model. This means that the NNMF model predicts easy axis (along the wire) rather than easy plane (perpendicular to the wire).

Table 4.1 This table summarizes the effect of contributions of 1, 2 ,3 and 5 nearest neighbors on total effective field for sample 500 (Ni20/Cu10), with geometrical detail in the text. The first column corresponds to the effective field model without including the numerical NN calculation. The next columns show how the total effective field is changed after we replace the NN contributions with numerical calculation for up to 5 neighboring disks. Note that using the NNMF model, the effective field has changed its sign from negative to positive meaning a prediction from easy plane to easy axis.

	effective field model (without numerical NN conri-bution)	1NN inclu-ded	1-2NN inclu-ded	1-3NN inclu-ded	1-5NN inclu-ded
Anisotropy Constant K (J/m^3)	-14252	-6017	-2192	19	2275
Total effective field $H_{eff}(Oe)$	-620	-261	-95	0	99

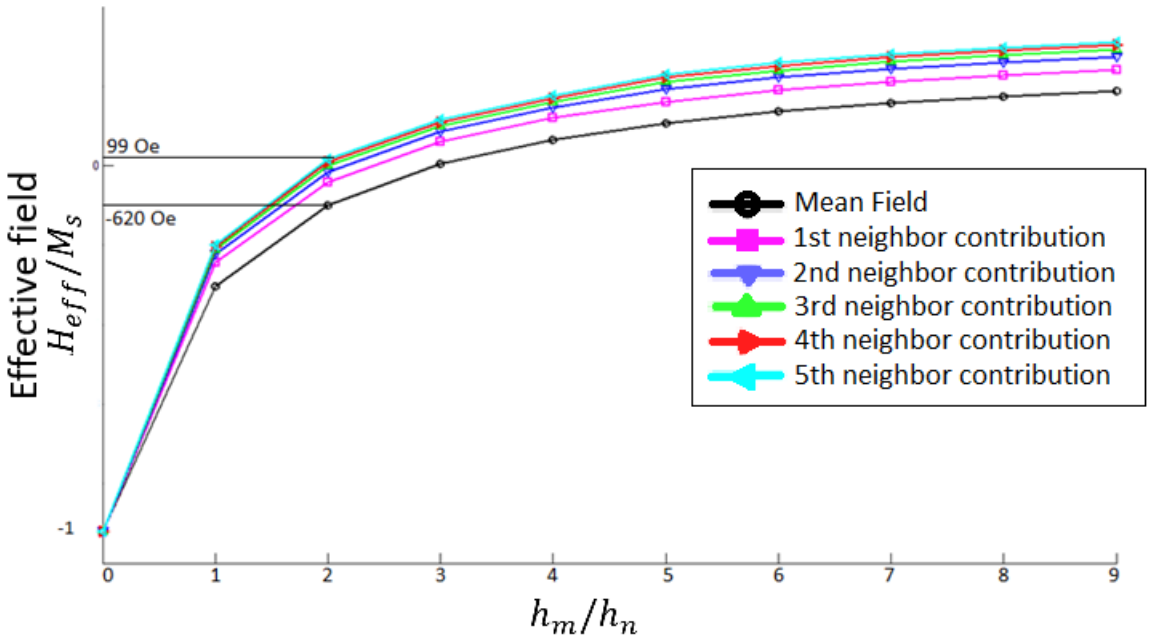

Figure 4.8 Effect of including different numbers of nearest neighbors in calculating the effective field in the sample of Figs. 4.5 and 4.6. Here the wire radius and template porosity is assumed constant while the ratio h_m/h_n is varied. The saturation magnetization is assumed to be 460 emu/cm^3 as suggested in Carignan *et al.* (2007) for Ni.

So far, we have demonstrated the effect of nearest neighbor dipolar interaction only on a specific sample. In order to present it in a more general situation, we have performed our numerical calculation on a range of different samples with various geometrical structures and compare the effective field in each case with and without including the nearest neighbor contribution. The results are presented in chapter 5.
The simplified expressions of the effective field model depends principally upon saturation magnetization, M_s, filling factor of the individual wire, $f = h_m/h$, and porosity (filling factor of the of the array), P. The dependence of this model upon wire radius is hidden in the estimation of demagnetization using Ozborn formula (see Eq. 4.18). However, one can expect a modified contribution from the mutual interaction field between each magnetic layer, depending on the wire radius, a. The NNMF model however depends on wire radius. We have compared the dependence of this model upon the various parameters with and without the nearest neighbor contributions.

Figure 4.9 presents the dependence of the two models on porosity, P. As we expect, since the nearest neighbor calculation depends only upon intrawire interaction, changing the porosity (while other parameters are kept constant) does not change the nearest neighbor interactions. As shown in figure 4.9, for all porosities, the change of effective field is constant (in this example 577.23 Oe). Note that the extreme values for porosity are not realistic and are only numerically calculated to see the dependence of the model to the porosity. In reality we expect the porosity to be more or less around 0.1. One can use Eq. 4.21 along with corresponding values for $M_s = 460$ emu/cm^3, $h_m = 20$ nm, $h_n = 10$ nm and $P = 0.1073$ to recover -620 Oe as shown in Fig.4.9 :

$$\begin{aligned} H_{eff} &= \frac{M_s}{2}\{1 - 3[1 - f(1 - P)]\} \\ &= -620 \text{ Oe} \end{aligned} \tag{4.26}$$

where we have multiplied the M_s with 4π to convert the units to Oe. This value of effective field corresponds to $K = -14252$ J/m^3. Using the NNMF model however, as explained above, one can fit the magnetic energy density vs θ as (see Fig. 4.7) to calculate the anisotropy constant, K, using the computer code in Appendix A. By doing so, considering only the first NN contribution, one can deduce that $K_{NN} = 14271$ J/m^3 which after adding up with $K = -14252$ J/m^3 will recover $H_{eff} = -43$ Oe as shown in Fig. 4.7.

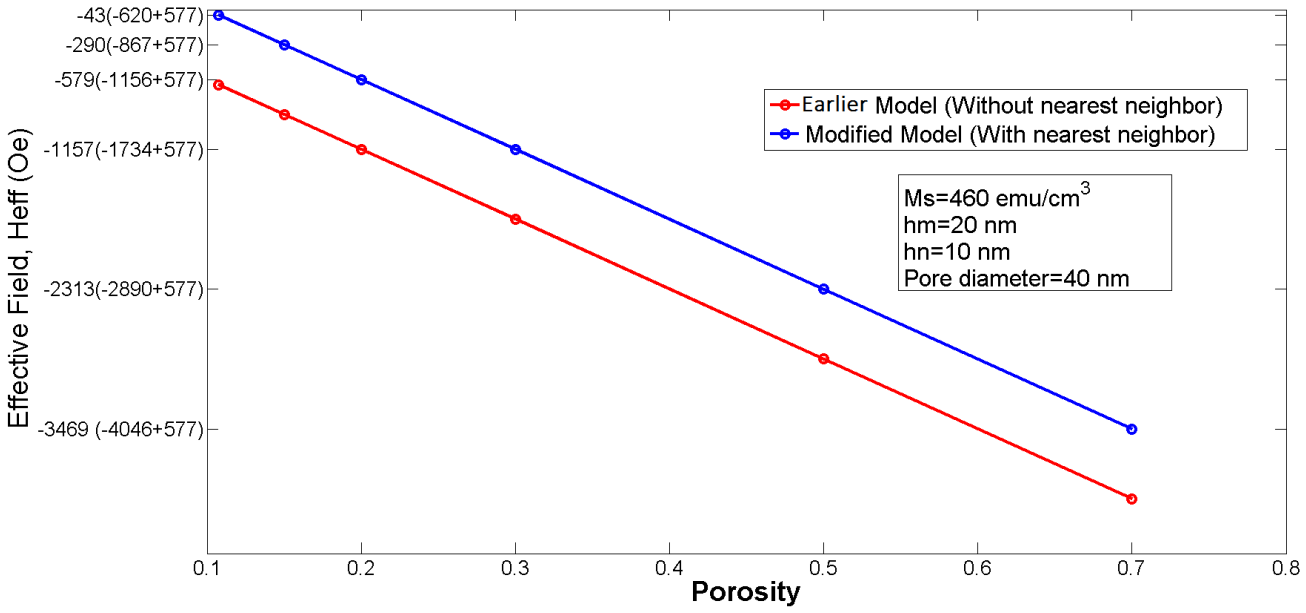

Figure 4.9 Comparison of the effective field between the effective field model and NNMF model (with 1 NN included) for various values of porosity.

Figure 4.10 presents the dependence of the two models upon saturation magnetization, M_s. In contrast to porosity, the NNMF model is very dependant to saturation magnetization as one can expect the higher the saturation magnetization, the greater the dipolar interaction between nearest neighbors. Figure 4.10 clearly shows that in cases we are dealing with magnetic materials with higher saturation magnetization, the effect of nearest neighbor interaction is not negligible at all.

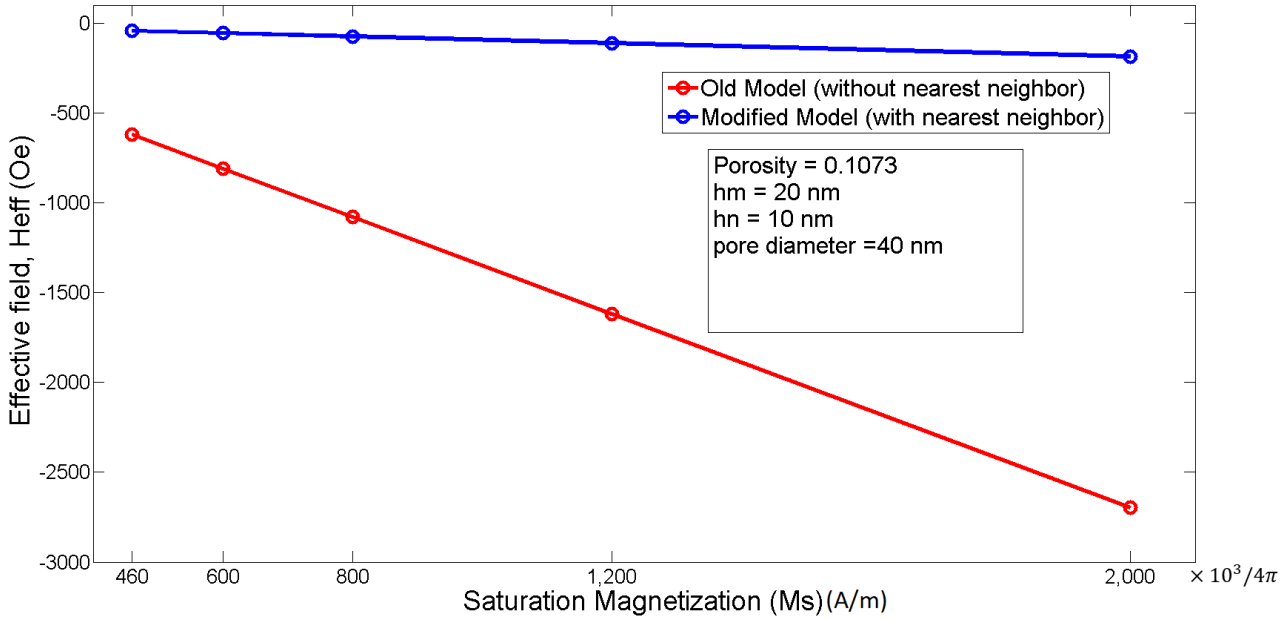

Figure 4.10 Comparison of the effective field between effective field model and NNMF model for various saturation magnetizations.

In figure 4.11 the effect of wire diameter, a, upon nearest neighbor interaction is shown. There is a maximum of importance for wires with diameter around $a = 30$ nm. This figure is created based on our numerical calculation for a system with $P = 0.1073$, $h_m = 20$ nm, $h_n = 10$ nm and $M_s = 460$ emu/cm^3. For different settings we will get different maxima with different diameters. However, the behaviour of the nearest neighbor interaction with respect to wire diameter is the same, that is as we grow the diameter larger, the effect of nearest neighbors becomes less important. Since the effective field model does not directly depend on wire diameter[3], for all diameters in figure 4.11 the effective field model gives us the same value for the effective field.

One should notice that the diameter in Fig. 4.11 starts at 30 nm. This is because in both models we have used an estimation of $c^{'} = h_m/2a \ll 1$ or in other words, we have assumed that the diameter is relatively large so that we can estimate each magnetic disk with an oblate ellipsoid. Below 30 nm, we need to assume prolate ellipsoids, which result in axial anisotropy. However, for a very small diameters, we expect that the effect of nearest neighbor becomes less important and the prediction of the effective field model and the NNMF model

3. Note that there is in principle a radius dependence for the effective field model given by the Ozborn formula 4.18, but that here we assumed the limiting case for which the demagnetizing factor is 1.

approach the same value as one can expect that there is no inhomogeneity for a disk of near zero diameter. Note that the value of 30 nm is not a general value for all systems. This is only the case for the specific simulation presented here, that is for $h_m = 20$ nm, $h_n = 10$ nm, $P = 0.1073$ and $M_s = 460$ emu/cm^3.

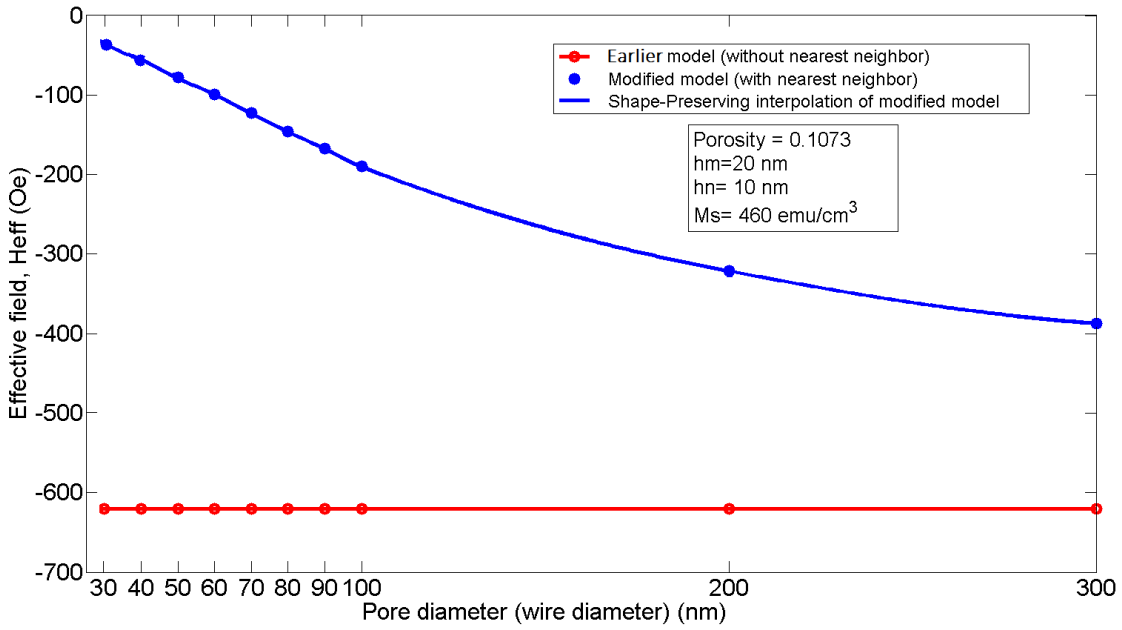

Figure 4.11 Comparison of the effective field between the effective field model and NNMF model for various pore (wire) diameters.

In fact, this behaviour of nearest neighbor interaction is because as we make the diameter larger and larger, the magnetic field produced by one magnetic layer over the neighboring disk becomes more homogeneous, so the inhomogeneity which is the source of the problem in the effective field model, becomes less important. In order to demonstrate the inhomogeneous field over the magnetic disks, we have used OOMMF to show the magnetic field over the neighboring disks for two different diameters, 30 nm and 300 nm. In figure 4.12, the field over the magnetic disk for $a = 300$ nm is relatively homogeneous compared with a disk with $a = 30$ nm. In this simulation, we have assumed that the dipoles are behaving in a rigid magnetization fashion.

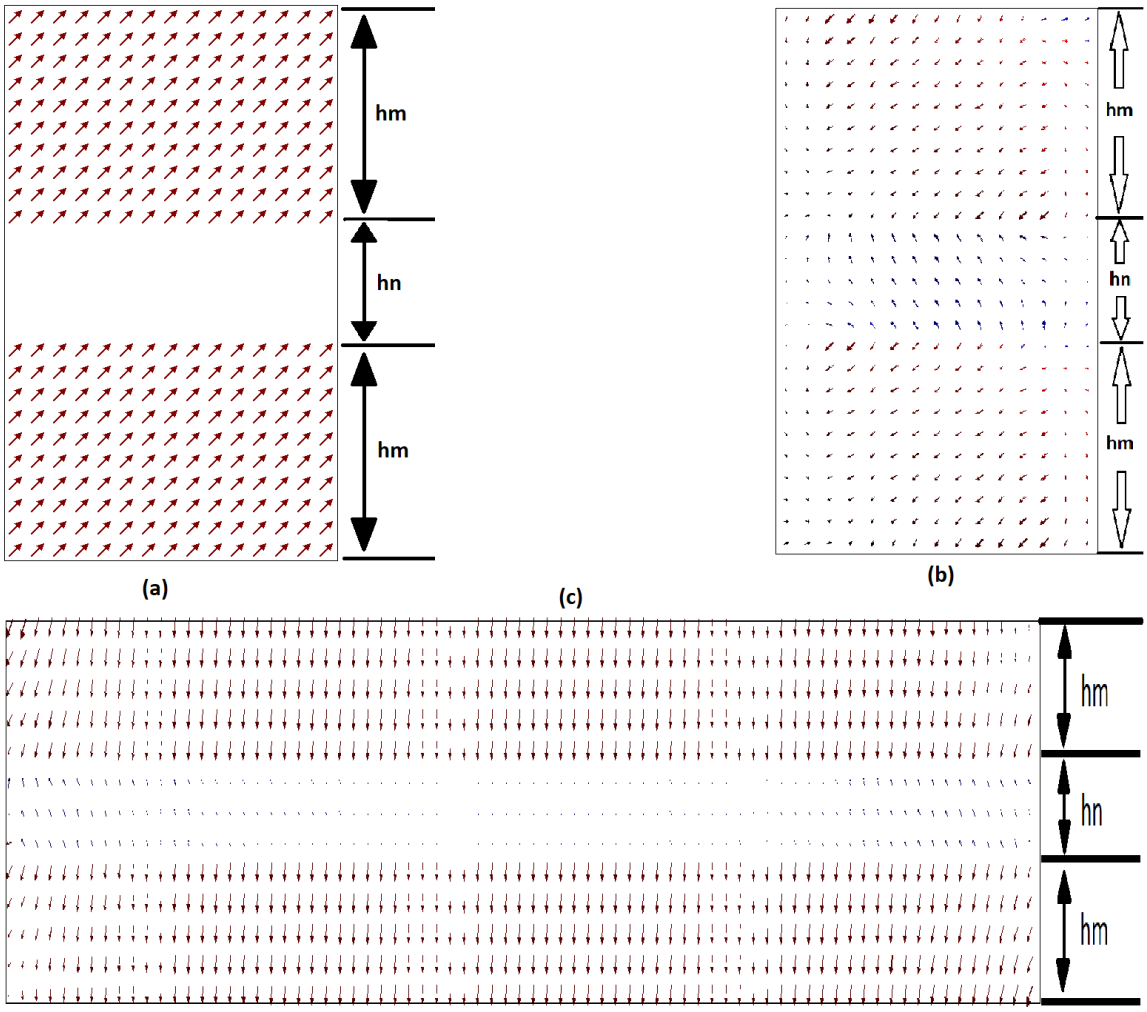

Figure 4.12 (a) Dipoles distribution in this simulation (b) Magnetic field over the disk with diameter $a = 30$ nm. As illustrated, the field is quite inhomogeneous over the disk (c) Magnetic field over the disk with diameter $a = 300$ nm and the same layer thickness as (b). As illustrated, the field is relatively homogeneous over the disk.

4.4.2 Non uniform magnetization

So far, we have assumed that the magnetization as a function of an external applied field is uniform in amplitude and orientation both in the effective field model and NNMF model. However, OOMMF simulations (Donahue, 1999) of exact distribution of dipoles have shown that, for certain dimensions of the disks, vortex distributions are obtained over the magnetic disks within a wire. In this section we have demonstrated that depending on geometrical and physical settings of the system, the magnetization of each layer in our multilayer systems is not rigid. We are not going to study the effect of exact distribution of dipoles in this

thesis. However, considering the exact distribution of dipoles may affect the results of NNMF model and further improve the model prediction. All related OOMMF codes are available in Appendix A. The following is the results of our simulation for various geometrical and physical conditions. However, before performing the simulations we need to have an estimation of the exchange stiffness, A, since it will determine the exchange interaction between dipoles. The total free energy of our system can be written as :

$$\epsilon_{tot} = \epsilon_{ex} + \epsilon_a + \epsilon_d + \epsilon_{stress} + \epsilon_{ms}. \tag{4.27}$$

In NNMF model, we have neglected the magnetocrystalline anisotropy, ϵ_a, applied stress, ϵ_{stress} and magnetostriction, ϵ_{ms} as described before. In this section, we are including the ϵ_{ex} which has been neglected before. In fact, exchange stiffness, A, will appear in ϵ_{ex} energy term as :

$$\epsilon_{ex} = \int A[(\nabla\theta)^2 + \sin^2\theta(\nabla\phi)^2]d^3r. \tag{4.28}$$

in which the term in bracket is the gradient of unit vector in the local direction of magnetization (θ, ϕ) relative to the z axis (Coey, 2010). The best way to estimate A which will be used in following simulations, is from the spin-wave stiffness D_{sw} in the low-energy magnon dispersion relation $\epsilon_d \approx D_{sw}q^2$, since the energy of the long-wavelength spin waves is associated with a gradual twist of the magnetization (Coey, 2010). It can be shown that this relation is :

$$A(T) = \frac{M_S(T)D_{sw}}{2g\mu_B}. \tag{4.29}$$

where $D_{sw} = 2JSa^2$. The value of D_{sw} is given in many magnetism text books (see for example (Coey, 2010)). This value is $6.3 \times 10^{-40}\text{Jm}^2$, $8 \times 10^{-40}\text{Jm}^2$ and $4.5 \times 10^{-40}\text{Jm}^2$ for Ni, Co and Fe respectively. So the exchange stiffness A for Ni for example is :

$$A = \frac{(488 \times 10^3) \times (6.3 \times 10^{-40})}{2g \times 9.274 \times 10^{-24}} \approx 9 \text{ pJ/m}$$

In order to have an idea of how the real reversal mode is, we need to consider a large number of wires with a large number of magnetic and non-magnetic layers. However, this will need a super computer to manage this problem. So in this example, we have simulated only 11 wires with 5 magnetic and non-magnetic layers for each wire and we are looking at the middle disk of the middle wire. The geometry of this simulation is illustrated in figure 4.13 below. The initial distribution of dipoles are random in this simulation. Interested reader is encouraged to read the appendix A for the details of the simulation.

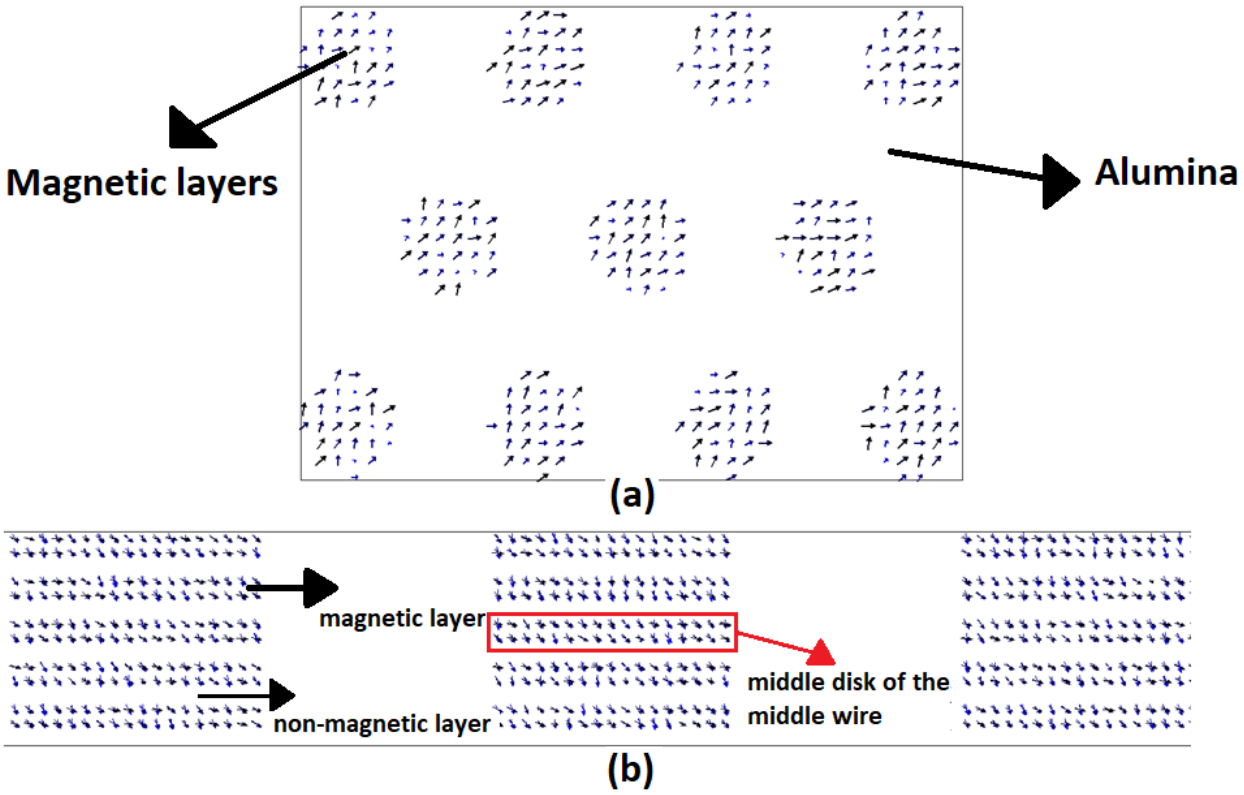

Figure 4.13 (a) Top view of the geometry of OOMMF simulation in order to see the reversal mode. (b) the cross section of the simulated arrays of nanowires.

After applying an external field we can see in figure 4.14 how the dipoles will distribute over the middle disk of the middle wire. In this figure, the external applied field is increasing 0.5 (kOe) towards X direction in each step. As it is shown, the dipoles will create non-uniform distribution before they all get aligned with external field.

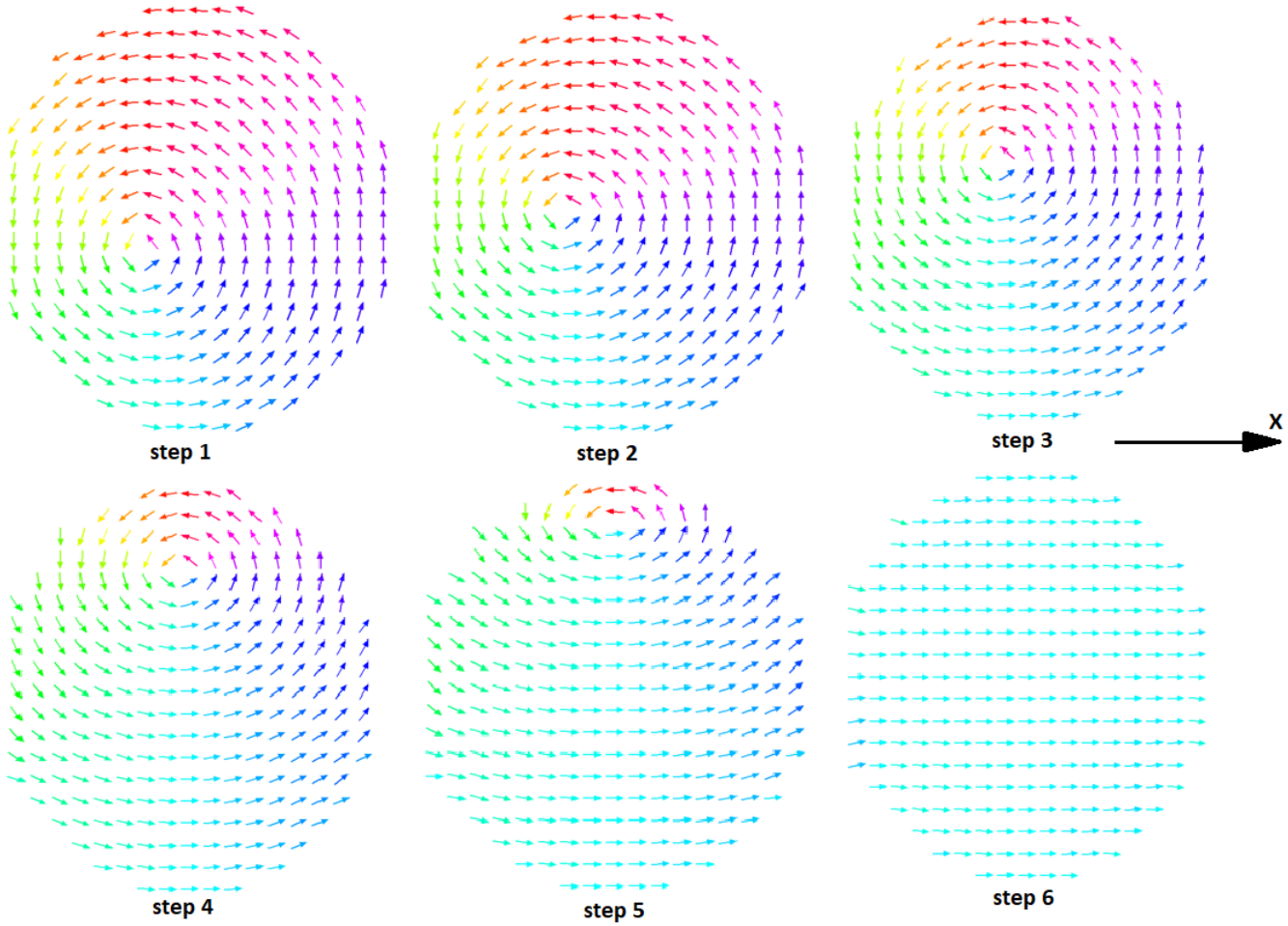

Figure 4.14 Steps 1 to 6 of applying external field. In each step the field increases 0.5 (kOe) in X direction. In this simulation the diameter of the wires are 170 nm, the interpore distance is 330 nm, the exchange stiffness $A = 9$ pJ/m and the saturation magnetization is $M_s = 490 \times 10^3$ A/m.

Figure 4.15 illustrates that only at very small diameters (less than 15 nm) the rigid magnetization can be a realistic approximation. Above this diameter, we will see vortex mode in our system. In this figure all physical settings are the same as figure 4.14 except the diameter which is increasing and the external field which is 1 (kOe) for all diameters.

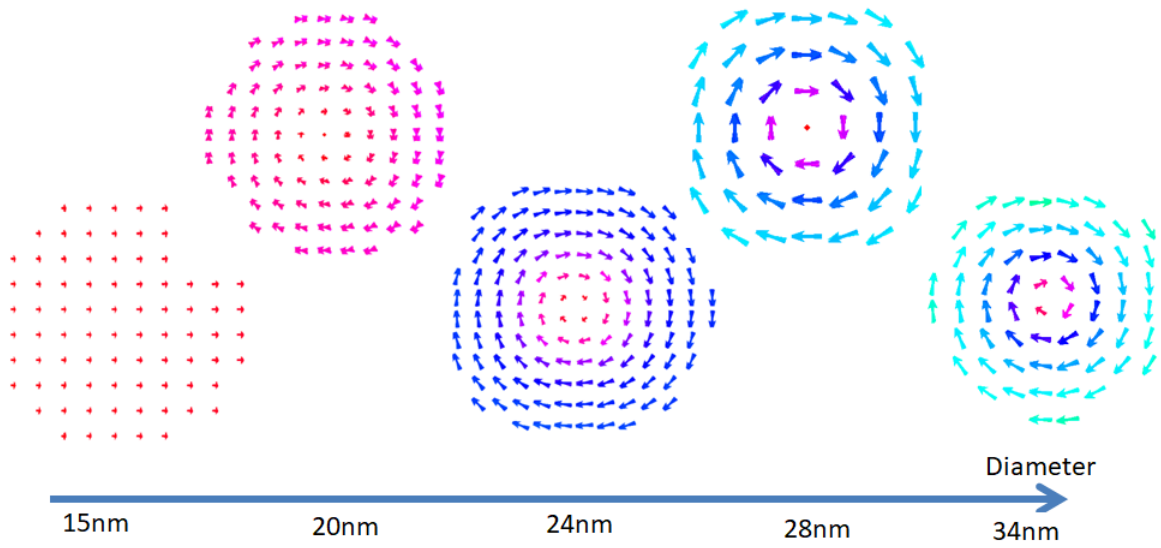

Figure 4.15 magnetic dipole distribution for applied external field of 1 (kOe) for different diameters. In this simulation, the interpore distance is 330 nm, the exchange stiffness $A = 9$ pJ/m and the saturation magnetization is $M_s = 490 \times 10^3$ A/m.

Here we showed that for wires with diameters sufficiently large compared to the exchange length, submitted to magnetic a field smaller than the saturation field, we expect a breakdown of the rigid magnetization approximation. The average of the non uniform field would result in a smaller effective dipolar field as compared to that of the rigid magnetization model. For even larger diameter, we expect a multi-domain magnetic configuration which would result in similar conclusions.

Here, we are not going into detail of this subject more than this. However, the interested reader can perform many different simulations for a variety of physical, chemical and geometrical compositions. All source code of these simulations are provided in appendix A for further investigation.

CHAPTER 5 EXPERIMENTAL RESULTS

5.1 Introduction

In this chapter we examine our fabricated samples from different aspects. First, we test our alumina templates for their geometrical and morphological consistency. We use some statistical test to make sure their consistency is statistically meaningful.
Then we examine the chemical composition of our nanowires. Auger spectroscopy was used to measure the purity of each magnetic and non-magnetic disk to examine the purity of each layer. The benefit of Auger spectroscopy is that the compositional and spatial resolution is very high compared to alternative methods such as XPS, Raman, or EDS in SEM for example. One can use EDS in TEM, however, sample preparation is time consuming in this method. Either the sample has to be thinned to become electron transparent, or individual nanowires has to be transferred onto a TEM grid. Another advantage of Auger spectroscopy is that it allows to study many nanowires at the same time. However, this method is relatively slow and expensive.
Last, we present some vibrating sample magnetometry (VSM) and ferromagnetic resonance (FMR) measurements to experimentally measure the effective field to compare with our model (NNMF model) presented in Chapter 4.

5.2 Morphology and structural analysis : SEM results

In this section we analyse the geometrical properties of our AAO templates to see how reproducible our template is. Essentially we perform some statistical *t-test* analysis on different samples to see if we can confirm that the pore diameter and interpore distance of our samples are consistent. In order to do so, we analyse two different samples which were fabricated under the same conditions. All our templates were fabricated under the same conditions so we can assume the rest of our samples, which were used in electrodeposition, have the same geometrical features. Usually, in *t-test*, we would like to compare the mean of two different data sets to see if there is a significant difference between the two groups by changing one (or more) factors. However, in this study, our desired result is when we see no significant difference for pore diameter and interpore distance so we can conclude that our samples have the same pore diameter and interpore distance at least with some level of confidence.

5.2.1 Preparing the data sets and performing the hypothesis testing

Here we compare two samples, A1 and A2 (fabricated under the same condition) as shown in Figure 5.1 to confirm that our samples are consistent and reproducible.

Using ImageJ 1.52a software, a powerful open source image processing software, we detect our pores and estimate their area. In order to do so, we have calibrated our measurements based on a known length in the original SEM images. Having the area, A, of each pore and assuming the pores are perfect circles, we can estimate each pore diameter by $2a = 2\sqrt{A/\pi}$.

In figure 5.2 we have detected all the pore objects corresponding to figure 5.1. Table 5.1 shows the summary of statistical information about pore diameters, i. e. the number of pores in each image, average of pore diameter and variance.

Table 5.1 Sample A1 and A2 pore diameter statistics.

Samples	Pore Count	Average Diameter (nm)	Variance (nm^2)
A1	946	50.55	8.53
A2	890	50.53	6.30

In this analysis, we have ignored the detected diameters which are above 95% or below 5% percentiles. Using the data in table 5.1, we can calculate our *t-score* value as :

$$t_{score} = \frac{\bar{X}_1 - \bar{X}_2}{\sqrt{\frac{v_1}{n_1} + \frac{v_2}{n_2}}} \tag{5.1}$$

where $\bar{X}_1$ and $\bar{X}_2$ are the mean diameter, v_1 and v_2 are the variance, and n_1 and n_2 are the count of data points for samples A1 and A2 respectively. Substitution of our data into the equation 5.1 we can calculate our *t-score* value :

$$t_{score} = 0.251$$

By looking at a student t-table (or using Excel) it is straightforward to find the critical value for the *t-score* with $946 + 890 - 2$ degree of freedom for 80% confidence level. The *t-critical* for the above situation is :

$$t^{80\%}_{critical} = 0.253$$

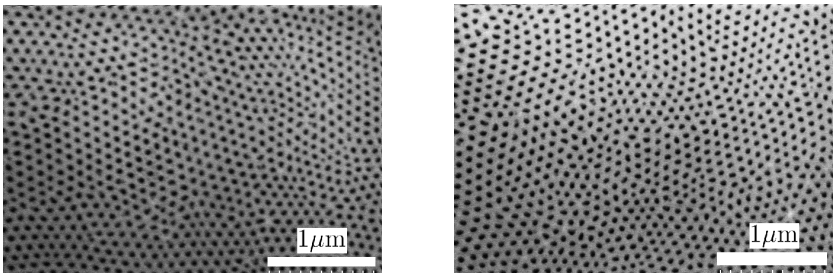

(a) Sample A1 (b) Sample A2

Figure 5.1 SEM top view of two different AAO samples A1 and A2 which were fabricated under the same experimental conditions. The samples were electropolished under the optimized conditions as explained in Chapter 3, Table 3.1, and were anodized based on the conditions explained in section 2.3.1.

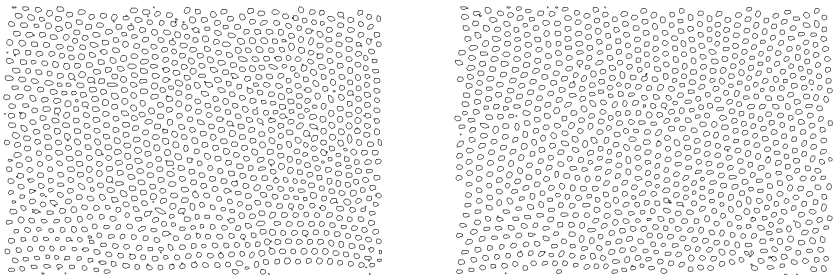

(a) Sample A1 (b) Sample A2

Figure 5.2 Detected pores corresponding to figure 5.1. The dimension scales are the same as in Fig. 5.1

Since our *t-score* is lower than the *t-critical*, we can deduce that our samples are the same with 80% confidence level. Another approach would be the calculation of *P-Value*[1] which will lead to the same conclusion. The *P-Value* for our two sets of data is $P_{Value} = 0.8$ which means we can conclude that our two sets of samples (i. e. pore diameters of two samples) are the same with 80% probability. Generally speaking, a *P-Value* of 1 means the two data sets are exactly the same and a *P-Value* of 0 means there is no overlap between the distribution of two data sets. A common threshold for the *P-Value* in order to consider the two data sets the same, is $P_{Value} > 0.05$.

We can repeat the same analysis for interpore distance. In order to calculate the statistics about interpore distance, we have detected the center of each pore and replaced it with a pixel as shown in figure 5.3. Then we have randomly selected 1000 pairs of pixels which are neighbors and calculate the distance between them to create our two sets of data. Table 5.2 shows the results.

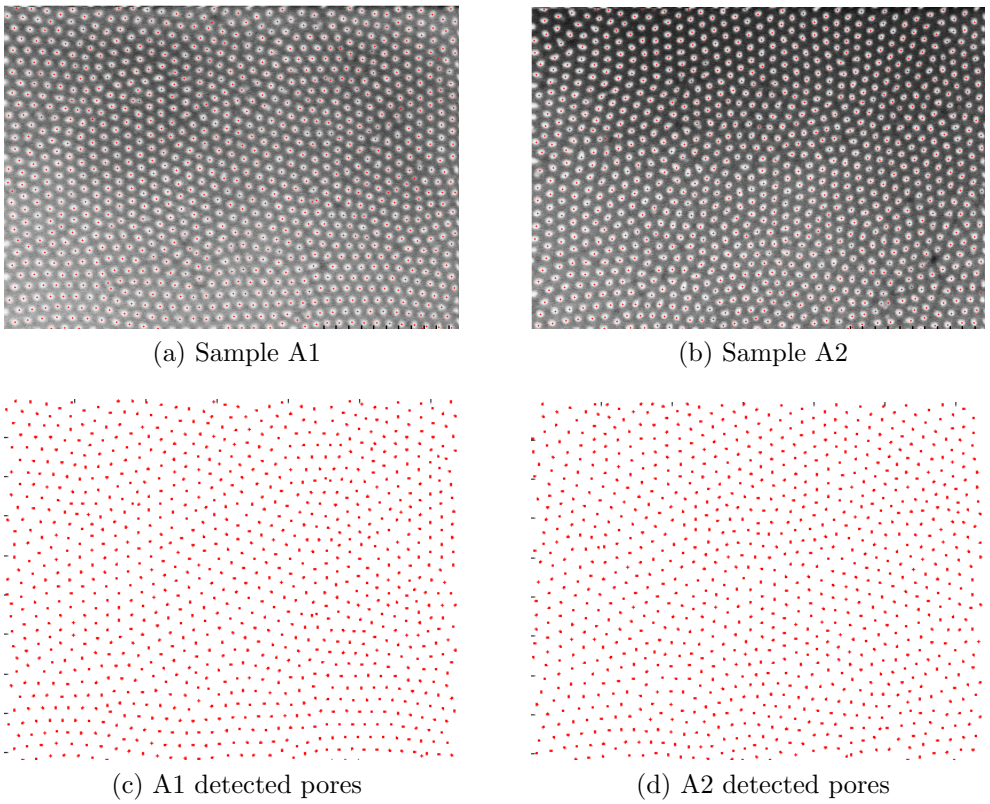

(a) Sample A1 (b) Sample A2

(c) A1 detected pores (d) A2 detected pores

Figure 5.3 Detecting centres of pores corresponding to figure 5.1.

1. *P-Value* can be interpreted as the probability of observing the same (expected) results in an experiment. Often, a *P-Value* less than 5% means the two test sets cannot considered to be equal.

Table 5.2 Sample A1 and A2 interpore distance statistics.

Samples	Pixels Count	Average Distance (nm)	Variance (nm^2)
A1	1000	100.51	103.48
A2	1000	100.40	100.05

By repeating the exact same analysis as we did for pore diameter, we can calculate the *P-Value* for our sample A1 and A2 to compare their interpore distance. By looking at a student-t distribution table, or as we did, using Excel :

$$P_{Value} = 0.81$$

which shows that our interpore distance in our two samples are again the same with at least 80% confidence. There is no statistically significant difference between the two data sets. As we did for previous analysis, we could calculate that the t_{score} and $t_{critical}$ for the two data sets based on Table 5.2 which will result in the same conclusion.

5.3 Chemical analysis

As discussed in Sec. 2.5, one of the challenges in magnetic/nonmagnetic multilayer nanowires, is that the noble metal (in our case Cu) which serves as a nonmagnetic spacer, will codeposit during the electrodeposition process making the Ni layer impure. This happens because the electrodeposition occurs in a single bath of all metal electrolytes and since the required voltage for Ni is lower than for Cu. Therefore, Cu can deposit while the less noble metal is depositing. To minimize this effect, we have done some simple calculations before starting the electrodeposition to measure how much Cu is required for the whole sample and we used just enough Cu so that by the end of electrodeposition, almost all the Cu electrolyte is consumed. In this way, we can make sure that the amount of Cu is dilute enough and the effect of codeposition is minimized.

In order to perform the chemical analysis, we have used Auger Electron Spectroscopy. In this technique, a target is bombarded with X-rays so that a core electron is removed from an atom leaving a vacancy. An electron with a higher energy will fall into that vacancy releasing energy causing an electron ejection from the atom. The relative energy of this secondary ejected electron with respect to the initial electron transition and ionization energy is unique for each atom. This allows us to determine the species from which the Auger electron was ejected.

First, one region of the sample is selected. Then the Auger spectroscopy sweeps the selected region with a very high resolution and determines the amount of each material in that region. The data is processed and the chemical components based on their locations are determined. In Fig. 5.4 we are looking at one single nanowire from sample S6[2]. The light and dark area correspond to Ni and Cu respectively. Then we have swept the rectangle area shown in the figure. The corresponding elemental analysis of this area is shown in Fig. 5.5.

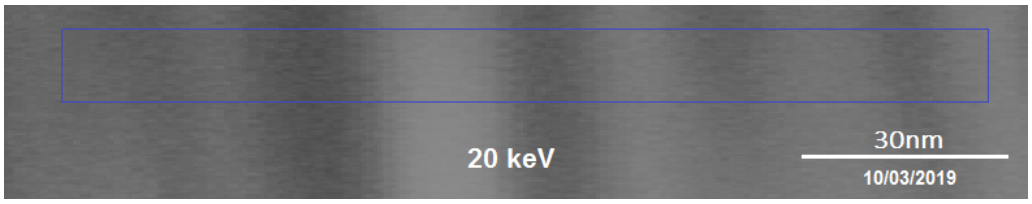

Figure 5.4 The selected region from sample S6 where the Auger Spectroscopy has been performed. The light and dark area correspond to Ni and Cu respectively.

The raw data shows oxygen (O) and some Al impurity as noise in background which is not very surprising. However, after removing the noise, the data corresponding to Cu and Ni shows acceptable purity of Ni and Cu, although there is still some Cu incorporated into Ni. One can notice higher mixture of Cu and Ni at the left side of the region. This can be due to the malfunctioning of the stirrer. Since the deposition of each layer takes place in a fraction of a second, even a small stop in stirrer (which was observed during some experiments) can negatively impact the deposition process.

2. For the details of each sample please see table 5.3 and 5.4

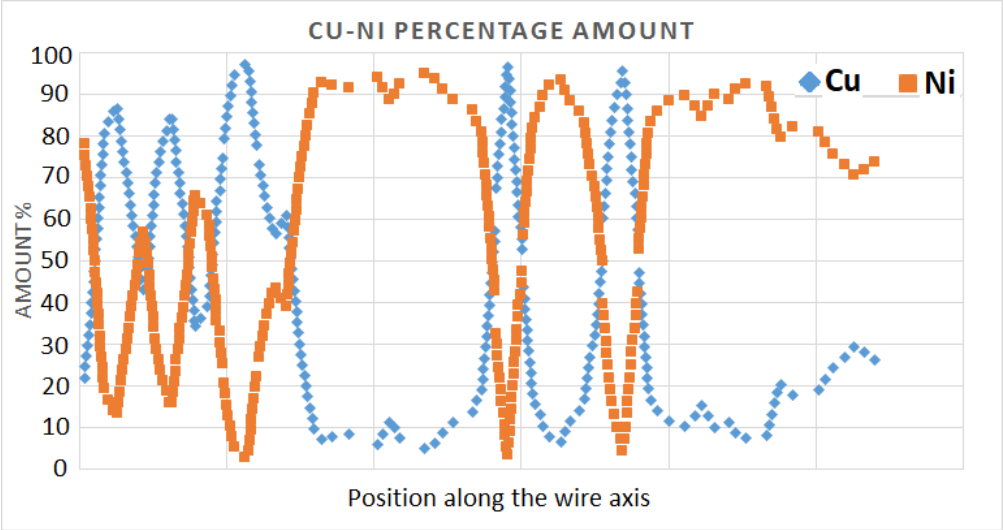

Figure 5.5 The percentage of Cu and Ni in each layer for the selected region of a single wire shown in figure 5.4 from sample S6. The scale of the figure is the same as the scale of Fig. 5.4.

5.4 Effective field measurement

In chapter 4, we discussed the effective magnetic field and our objective of tuning and predicting the effective field in arrays of ferromagnetic nanowires. Here, we examine the experimental results of measurements of the effective field for our samples and we compare those results with our predictions. One should note that, as discussed in chapter 2, we have been able to improve the fabrication of our samples to some extent. However, there are still some discrepancies in our observations which can come from imperfection of samples as discussed earlier. For example, the fact that not all pores are filled during the electrodeposition or that the layer thickness, although was improved, is still not in our full control or the incorporation (co-deposition) of nonmagnetic material into magnetic layers during the electrodeposition.

5.4.1 FMR and VSM results

In order to experimentally measure the effective field, we have taken two different approaches based on Ferromagnetic Resonance (FMR) and Vibrating Sample Magnetometry (VSM). Here, we explain how the effective field has been measured based on these two experimental methods.

Ferromagnetic Resonance (FMR)

In order to measure effective field using FMR, we have adopted the method explained in details in Carignan *et al.* (2007). The sample holder was rotated around its in-plane (IP) axis from 0° to 225° degrees with 15° degrees steps with respect to the applied static field. The applied field is high enough so the rigid magnetization model is justified. Smit and Beljers (Smit and Beljers, 1957) show that from the second derivative of the magnetic energy we can deduce the following :

$$(\frac{\omega_0}{\mu_0\gamma})^2 = [H_0\cos(\theta-\theta_H) + H_{eff}\cos 2\theta] \times [H_0\cos(\theta-\theta_H) + H_{eff}\cos^2\theta] \tag{5.2}$$

where $\omega_0 = 2\pi f$ is the angular frequency of the microwave pumping field, $\gamma = g\mu_B\hbar$ is the gyromagnetic ratio, g is the Lande factor, μ_B is the Bohr magneton, and $\hbar$ is the reduced Planck constant. Here, θ_H is the direction of the applied field and θ is the equilibrium position of the magnetization, calculated by minimizing the free energy. In (Carignan *et al.*, 2007), it is shown that for resonance at sufficiently high frequency such that $\theta = \theta_H$, we can simplify the above equation to the following :

$$H_0 = \frac{\omega_0}{\mu_0|\lambda|} + \frac{H_{eff}(1-3\cos^2\theta_H)}{2} \tag{5.3}$$

we have used this equation in order to measure the effective field in our samples using FMR at 19 GHz frequency. The effective field for samples S5,S6,S7,S8 and S9 (see Table 5.3) are calculated by fitting the data to equation 5.3 using least square fit method. Here, all parameters are known except H_{eff} which is calculated so that the square value of the difference between data points and the fitted curve is minimized. The results are shown in Fig. 5.6. Here we have use the notation Nix/Cuy where x and y are the thickness of Ni and Cu layers in nano meter (nm).

Table 5.3 Geometrical properties of samples. The expected wire diameter for all samples are 50nm.

	no. of magnetic layer disks	nominal magnetic thickness (nm)	nominal non-magnetic thickness (nm)
S5	2880	50	30
S6	600	26	10
S7	2850	12	5
S8	500	14	5
S9	1286	13	5

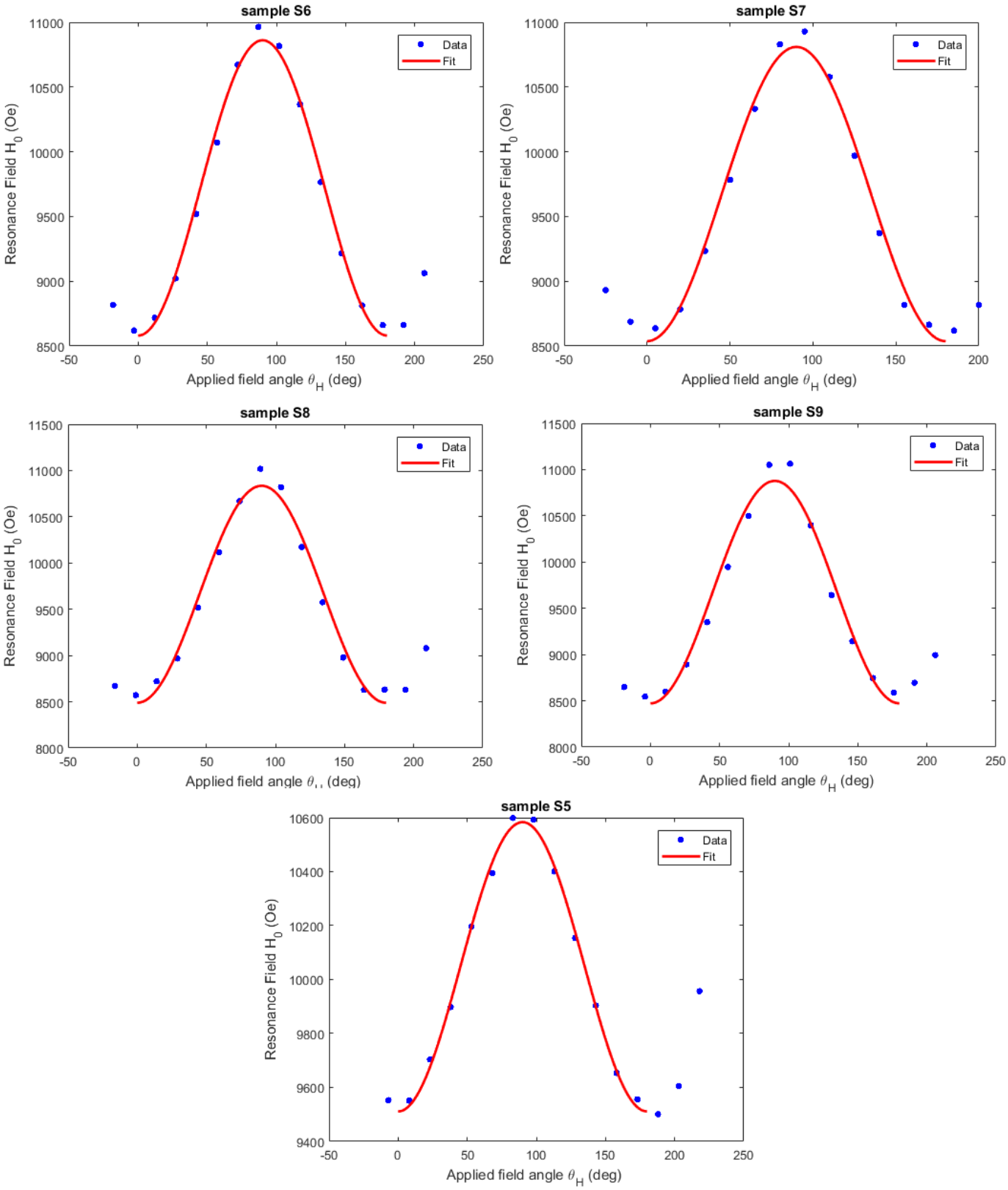

Figure 5.6 Resonance field H_0 as a function of the applied field angle θ_H for NiCu nanowires at $19GHz$ (a) for S6 : Ni26/Cu10 $H_{eff} = 1520$ (b) for S7 : Ni12/Cu5 $H_{eff} = 1514$ (c) for S8 :Ni14/Cu5 $H_{eff} = 1563$ (d) for S9 :Ni13/Cu5 $H_{eff} = 1603$ (e) for S5 :Ni50/Cu30 $H_{eff} = 714$. All fields units are in Oe.

Vibrating Sample Magnetometry (VSM)

In order to calculate the effective field using VSM measurement, each sample was cut in a small piece and placed in the VSM machine to collect the hysteresis curves for them. As we discussed earlier, we have assumed that our samples behave in a rigid magnetization mode, meaning that all magnetic dipoles are coherently in the same direction at all stages. This assumption is well justified in FMR because the sample is saturated and the magnetization is assumed to be uniform. However, in VSM measurements since the sample is not saturated at low fields, rigid magnetization is not justified. However, one can assume that the components of the magnetization perpendicular to the applied field are summed to zero or equivalently $M = M_s \cos\theta$ for out-of-plane (OOP) direction and $M = M_s \sin\theta$ for in-plane (IP) direction. This will lead two different expressions for effective field for IP and OOP configurations. Hence, one can assume that there is an effective demagnetizing field H_{dem} which is $H_{dem} = -\tilde{N}M$ where $\tilde{N}$ is the effective demagnetizing factor and M is the average magnetization. IF we also assume that there is an intrinsic isotropic susceptibility χ_{int} which excludes all dipolar interactions, one can write the macroscopic field H_{mac} as : $H_{mac} = H_{app} + H_{dem}$ where H_{app} is the applied field. Therefore, the magnetization can be written as :

$$M_{ip,oop} = \chi_{int}(H_{app} - \tilde{N}_{ip,oop} M_{ip,oop}) \tag{5.4}$$

Thus :

$$\chi_{ip,oop} = \frac{M_{ip,oop}}{H_{app}} = \frac{\chi_{int}}{1 + \chi_{int}\tilde{N}_{ip,oop}} \tag{5.5}$$

where $\chi_{ip,oop}$ is the slope of the hysteresis curves in the IP and OOP directions and corresponds to the apparent susceptibility in the IP and OOP directions. Since the intrinsic susceptibility is extremely large in the case where magnetic anisotropy is dominated by dipolar field, the intrinsic susceptibility in Eq. 5.4 can be approximated as $1/\tilde{N}$.
Solving Eq. 5.5 for $\tilde{N}_{ip,oop}$ using the fact that $H_{eff} = \frac{M_s}{2}\left(1 - 3\tilde{N}_{oop}\right)$ will result in :

$$H_{eff} = \frac{1 - \tilde{\chi_{ip}}/\tilde{\chi}_{oop}}{\tilde{\chi}_{ip}} \tag{5.6}$$

where $\tilde{\chi}_{ip,oop} = \chi_{ip,oop}/M_s$ is the normalized apparent susceptibility in IP (OOP) directions, obtained from the slope of the VSM hysteresis loops at $M = 0$. Using Eq. 5.6, we can easily estimate effective field for each sample (Carignan *et al.*, 2007). One should notice that the VSM method also requires the knowledge of the total volume of the magnetic components of the samples in order to transform the measured magnetic moment into a magnetization and thus obtain the susceptibility in equation 5.6. As discussed earlier, our estimation of total

magnetic volume might not be very close to reality and that is why we tend to rely on FMR results more than VSM. The expected properties of our samples are listed in Table 5.4. As one can notice, M_s for some samples are extremely high. We speculate that this is due to our underestimation of total magnetic volume.

5.4.2 Applying the nearest neighbor interaction in mean field model and comparison with experimental results

In chapter 4 we provided an example of one of our previous samples and showed how including the nearest neighbor interaction can dramatically change the predicted effective field. Since our nearest neighbor calculation was done numerically here we briefly explain how we incorporate the results of nearest neighbor calculation into the mean field model.
The first step is to calculate the B field due to all dipoles from the nearest neighbor magnetic disks over the desired disk in which we are calculating the field. This is done using the code provided in Appendix B and Eq. 3.17. Once we have the B field, we can calculate the magnetic density energy for different angles for this tri-layer system, i. e. the target disk, the top and the bottom disk. Then we can fit these numerically calculated data with equation 3.9 ($U_{dipolar} = K \sin^2\theta + C$). By fitting our data with this equation we can calculate the K constant corresponding to nearest neighbor dipolar (the tri-layer contribution) and add it to our previous K value calculated from the mean field model (excluding the contribution of nearest neighbors calculated by mean field approach as explained in details in chapter 4 in order to avoid considering the NN contribution twice by both models). We have run the calculation on our different samples set ups (i. e. the layer thickness, diameter and the material which is Ni in our samples) and provided the magnetic density energy diagrams for each case along with their corresponding calculated K values in figure 5.7 and table 5.5. In this figure, we show only the contribution of NN disks based on our numerical calculations. Please note that in figure 5.7 we have demonstrated the data only for the first layer while in practice, we have repeated this procedure for 5 nearest neighbor layers as already explained in chapter 4.

As shown in Table 5.5, the theoretical results are closer to experimental results compared with our previous samples and model (with the exception of sample S5, the NNMF model matches $60\% - 80\%$ with experimental results). Although we were able to improve the sample fabrication to some extent, still part of this discrepancy might be due to imperfection of our samples since we still see some impurities in our magnetic layers and most probably the layer thickness is still not completely match with what we expected. Also, we have ignored some factors in NNMF model which might cause some inaccuracy in our predictions. For example,

Table 5.4 Magnetic properties used for VSM measurements.

	Total magnetic volume (m^3)	M_s (kA/m)	χ_{ip} / χ_{oop}
S5	18.1×10^{-12}	184	1.32 / 1.8
S6	4.73×10^{-12}	1813	9.91 / 21.02
S7	4.14×10^{-12}	828	4.68 / 10.87
S8	1.67×10^{-12}	3126	17.37 / 40.62
S9	1.61×10^{-12}	2479	14.9 / 26.63

Table 5.5 Effect of contribution of 1st and the first 5 neighbors combined.

		Without NN	**1stNN**	**1st to 5th NN**	**VSM**	**FMR**
S5 Ni50/Cu30	$K(J/m^3)$	-1075	15488	26240	10684	16329
	H_{eff}(Oe)	-47	630	1100	467	714
S6 Ni26/Cu10	$K(J/m^3)$	137	14253	23198	27751	34762
	H_{eff}(Oe)	6	629	1020	1213	1520
S7 Ni12/Cu5	$K(J/m^3)$	-277	10386	17867	28940	34625
	H_{eff}(Oe)	-12	442	769	1265	1514
S8 Ni14/Cu5	$K(J/m^3)$	183	11187	16416	29627	35745
	H_{eff}(Oe)	8	497	813	1295	1563
S9 Ni13/Cu5	$K(J/m^3)$	-23	10890	18302	21070	36660
	H_{eff}(Oe)	-1	475	799	921	1603

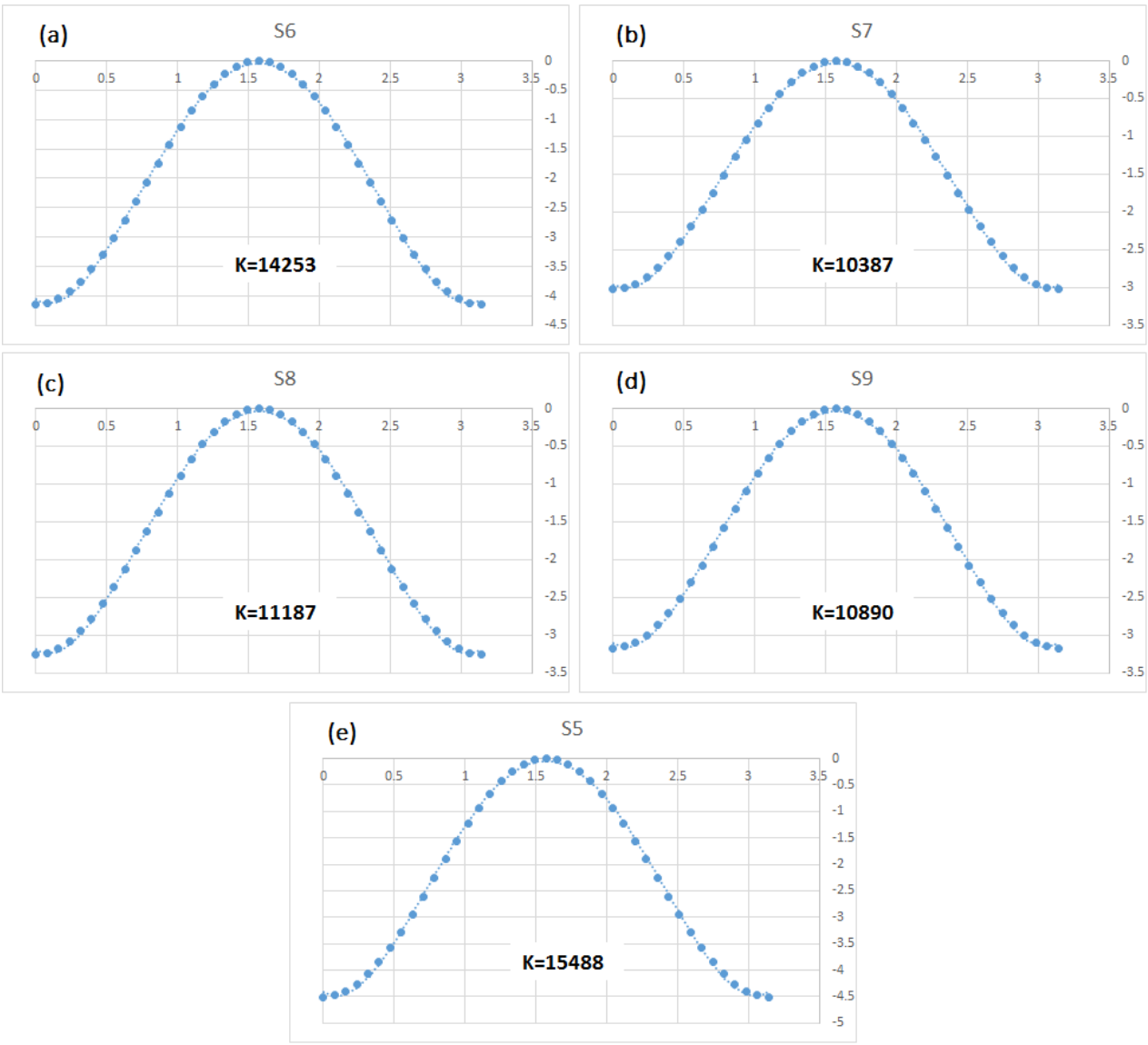

Figure 5.7 Magnetic energy density (J/m^3) as a function of θ (angle between dipoles and wire axis) for samples S6, S7, S8, S9 and S5. The circles are calculated data from the code (Appendix A) and blue dashed lines are the fitting result using equation 3.9 to obtain anisotropy constant K(J/m^3).

we have not considered the unfilled pores or a distribution of wire lengths.

There is much to be discussed from Table 5.5. First, there is a significant discrepancy between the effective field obtained from the FMR and VSM, where FMR systematically yields higher values. It is important to mention that the two methods do not rely on the same assumptions. In FMR, H_{eff} is calculated assuming the material is magnetically saturated by the external field, which is fairly justified for the range of field of up to 2T used to carry the experiment at 19 GHz. The VSM method, however, is based on an assumption that the samples are multidomains, with extremely high DC susceptibility, and exhibit anhysterectic responses no matter what is the direction of the applied field (Carignan *et al.*, 2007). The H_{eff} are calculated from the differential susceptibility of the demagnetized samples and can be quite sensitive to the above assumptions, which are usually justified in soft macroscopic samples, but not with monodomain nanoparticles. Here, we can speculate that our 50 nm diameter nanowires are not strictly monodomain when demagnetized, but rather in a non uniform magnetic configuration that is not yet multidomain. This, to some extend, was observed in our computer simulations with OOMMF software in section 4.3.2. This is likely to be the origin of the difference between the two methods.

Also, the simulated result is sensitively dependent on our priori knowledge of the layer thicknesses and compositions. Unfortunately, in spite of our improvements in the fabrication methodology, we were not capable of assessing how well the actual thicknesses would match the anticipated ones. Beside, we did observe in section 5.3 that the stoichiometry could be off, leading to different magnetization that were assumed in the model. All things considered, we believe that the discrepancy between the simulated and measured values should not be seen as a failure of NNMF model, but rather as an indication that further improvement is needed to control the layer thicknesses and stochiometries.

CHAPTER 6 CONCLUSION AND FUTURE WORKS

6.1 Conclusion

We have studied the fabrication of arrays of multilayer ferromagnetic nanowires. It was shown that by applying a careful preprocessing step prior to anodization of aluminum, highly ordered porous alumina can be obtained. A quantitative analysis was developed and used to measure the correlation of preprocessing steps, i. e. electropolishing in order to eliminate the surface roughness, and the pore regularity. Another quantitative image processing method was developed to evaluate our pore ordering by assigning a regularity number to our porous templates. This way, we can optimize the factors such as applied voltage, temperature and time of anodization in a meaningful statistical manner. The best results for electropolishing were achieved by applying 12V at $80°C$ for 6 minutes. It was shown that the smoother the surface (the better the electropolishing) the higher the pore regularity we can achieve in porous alumina template.

An effective field model based on the mean field approach was then applied to predict the magnetic anisotropy of our samples. In order to improve agreement with experiment, we developed a numerical calculation of the contribution of dipolar interaction of neighbouring magnetic layers up to five nearest neighbours. We were able to predict the effective field of up to 80% accuracy in comparison with experimental results. While we still observe a discrepancy, mostly due to the imperfections of the samples, we have nevertheless achieved a significant improvement in comparison with the mean field model which was inadequate to predict the effective field of the arrays of ferromagnetic multilayer nanowires with certain geometries.

Auger electron spectroscopy was used to do the chemical analysis. Results showed that eventhough there are still impurities in magnetic and nonmagnetic layers, a great improvement has been achieved in comparison with our previous fabrications (see Carignan *et al.* (2007) and Akhtari-Zavareh *et al.* (2014) for instance).

One can notice that the real porosity (effective porosity) of our samples can be quite different from the expected ideal porosity as it was discussed in detail in section 3.3. Since our model is very sensitive to porosity factor, we also proposed an experimental method in order to directly measure the effective porosity factor by an experimental method, which we call the overflow technique. In this technique, due to the change of behaviour of electrical current, and knowing the membrane thickness and the materials deposited, and the number of pores and their diameter, we can estimate how many pores have been really filled during the elec-

trodeposition making it possible to give a better and more realistic estimation of effective porosity factor.
The t-test statistical method was also used to show that the geometric properties of our AAO membranes (pore diameter and interpore distance) are consistent and reproducible in a statistically meaningful sense.

6.2 Future works

As discussed above, there are still possible improvements one can achieve by taking more factors into account in the study of ferromagnetic multilayer nanowires. Below we have proposed some future works which we believe can further improve the effective field model.

6.2.1 Orange peel coupling

For most deposited material like multilayer nanowires, the surface of layers are not perfectly flat. This can results in a new interaction which was not considered in our model. Néel (1962) shows that if the topographies of the two surfaces are in perfect correlation, as shown in Fig. 6.1, the flux closure of the poles on one layer by the poles on the other layer results in a non-negligible interaction (Yelon, 1971). This can be equally important at the interwire level due to the roughness of the wire surfaces along the pore walls. Especially, if we have an array of single composition wires, the impact of the surface roughness of the wires along the pore walls can be more important. This is because if we try to saturate the wires along their axes, we expect to have positive and negative magnetic poles along the surface of each wire. These poles will compete with any effort to saturate the array parallel to the wire axes. This interaction has been referred as "orange-peel" coupling in the literature because of its specific topography.

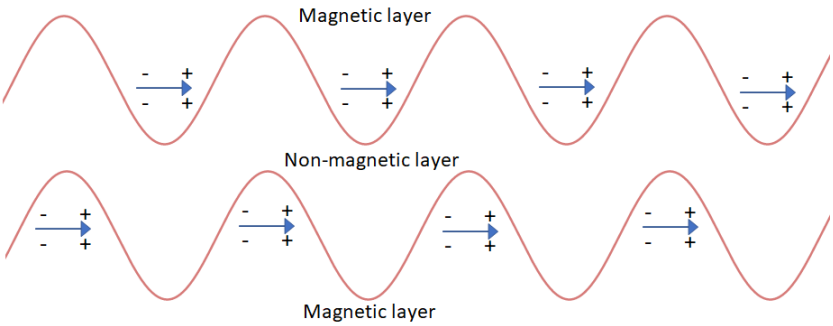

Figure 6.1 Orange peel coupling in magnetic layers of a multilayer nanowire.

6.2.2 Considering the real length distribution

Not all deposited wires have the same length. Due to various reasons, most probably the formation of hydrogen bubbles during the electrodeposition, some pores are filled, some are empty while some are partially filled. One may take into account the length distribution to more realistically estimate the effective field. Probably one can start with bipolar length distribution to see if any improvement can be achieved. Basically, the bipolar length distribution assumes that three kinds of pores. Completely filled, Completely empty and half filled. Then a more general distribution, for example a Gaussian distribution can be considered.

6.2.3 Exact magnetization distribution

As discussed in chapter 4, we have assumed that our samples follow the rigid magnetization state meaning that we have assumed that all magnetic moments are uniformly aligned through out the entire sample. However, we know that depending on the material used, pore diameter and length and aspect ratio of magnetic layer as well as the thickness of the spacer layers can affect the magnetization distribution of magnetic moments. Arange of situations, from vortex to flower states, are possible. This can be incorporated into the dipole-dipole interaction, especially for the numerical calculation of neighbouring magnetic layers.

6.2.3.1 OOMMF simulations

One approach to extract the magnetization distribution is to use the OOMMF simulation framework. We have shown some simple cases and we saw that, in fact, rigid magnetization is unrealistic in many cases. One can further try to take the real magnetization distribution of magnetic dipoles into account for the model.

6.2.4 Considering pore block during the deposition

This was discussed in section 2.4.2 (layer thickness measurement). There we mentioned that because some pores are getting blocked during the deposition, we are depositing the same amount of charge into fewer pore therefore the layer thickness will increase as we get closer to the top of the template. Roughly speaking, we expect to have smaller number of layers but thicker layers as we go from the bottom to the top of the sample.

6.3 Final Word

In this work, we improved control of the fabrication process of multilayer nanowires, particularly the pore regularity of the template (porous alumina), controlling the layer thickness of each disk and purity of magnetic disks. Despite the improvement in each section, we still have considerable room for improvement.

Using the standard two-step anodization, although the pore regularity was improved by maximizing the surface smoothness prior to anodization, still the perfect pore regularity was not achieved. However, this might not be critical in some applications. It seems that Coulometry is the right approach to control the layer thickness, however, more factors can be involved as discussed in the above section. We believe that some impurity (co-deposition of non-magnetic material) is unavoidable in a single bath electrolyte setup. The mean-field approach (inspired by Oguchi model) seems promising to predict the magnetic anisotropy of these systems, however, we speculate that another factor, namely surface anisotropy also plays a non-negligible role in effective field. Therefore, one should take that into account as well.

Above, we have proposed four possible future works to improve this project. The first three (namely sections 6.2.1, 6.2.2 and 6.2.3) deal with the model to describe the magnetic anisotropy. While all three factors could be equally important, one may start by incorporating the orange-peel coupling and the exact magnetic distribution into the model simply because they can be studied faster and are less expensive to study. Considering the real length distribution can be more time consuming and costly if someone wants to collect proper data for that. Finally, one may incorporate the pore blocking into account to improve the Coulometry experiment and thus better control layer thickness during the deposition.

REFERENCES

AKHTARI-ZAVAREH, A., CARIGNAN, L., YELON, A., MÉNARD, D., KASAMA, T., HERRING, R., DUNIN-BORKOWSKI, R. E., MCCARTNEY, M. and KAVANAGH, K. (2014). Off-axis electron holography of ferromagnetic multilayer nanowires. *Journal of applied physics*, 116, 023902.

ARAMESH, M. and CERVENKA, J. (2014). Surface modification of porous anodic alumina for medical and biological applications. *Nanomedicine*, 438, 438.

BELLEMARE, J., CARIGNAN, L.-P., SIROIS, F. and MÉNARD, D. (2015). Etching the oxide barrier of micrometer-scale self-organized porous anodic alumina membranes. *Journal of The Electrochemical Society*, 162, E47–E50.

BELLEMARE, J., SIROIS, F. and MÉNARD, D. (2014). Fabrication of micrometer-scale self-organized pore arrays in anodic alumina. *Journal of The Electrochemical Society*, 161, E75–E80.

BÉRON, F., CARIGNAN, L.-P., MÉNARD, D. and YELON, A. (2008). Magnetic behavior of ni/cu multilayer nanowire arrays studied by first-order reversal curve diagrams. *IEEE Transactions on Magnetics*, 44, 2745–2748.

BÉRON, F., CARIGNAN, L.-P., MÉNARD, D. and YELON, A. (2010). Extracting individual properties from global behaviour : first-order reversal curve method applied to magnetic nanowire arrays. *Electrodeposited Nanowires and their Applications Vienna : IN-TECH*, 167–88.

BÉRON, F., CLIME, L., CIUREANU, M., MÉNARD, D., COCHRANE, R. W. and YELON, A. (2006). First-order reversal curves diagrams of ferromagnetic soft nanowire arrays. *IEEE transactions on magnetics*, 42, 3060–3062.

BISWAS, A., BAYER, I. S., BIRIS, A. S., WANG, T., DERVISHI, E. and FAUPEL, F. (2012). Advances in top–down and bottom–up surface nanofabrication : Techniques, applications & future prospects. *Advances in colloid and interface science*, 170, 2–27.

BLAND, J. (2002). A mössbauer spectroscopy and magnetometry study of magnetic multilayers and oxides.

BOCCHETTA, P., SUNSERI, C., BOTTINO, A., CAPANNELLI, G., CHIAVAROTTI, G., PIAZZA, S. and DI QUARTO, F. (2002). Asymmetric alumina membranes electrochemically formed in oxalic acid solution. *Journal of applied electrochemistry*, 32, 977–985.

BRILL, P. H. (2000). A brief outline of the level crossing method in stochastic models. *CORS Bulletin*, 34, 9–21.

CARIGNAN, L.-P. (2012). *Modélisation, développement et caractérisation de matériaux magnétiques à base de nanofils ferromagnétiques pour les technologies hyperfréquences*. Thèse de doctorat, École Polytechnique de Montréal.

CARIGNAN, L.-P., LACROIX, C., OUIMET, A., CIUREANU, M., YELON, A. and MÉNARD, D. (2007). Magnetic anisotropy in arrays of ni, cofeb, and ni/cu nanowires. *Journal of applied physics*, 102, 023905.

CARIGNAN, L.-P., YELON, A., MÉNARD, D. and CALOZ, C. (2011). Ferromagnetic nanowire metamaterials : Theory and applications. *IEEE Transactions on microwave theory and techniques*, 59, 2568–2586.

CHEN, M., CHIEN, C.-L. and SEARSON, P. C. (2006). Potential modulated multilayer deposition of multisegment cu/ni nanowires with tunable magnetic properties. *Chemistry of materials*, 18, 1595–1601.

CHOU, S. (1997). Quantized magnetic disks. *Chines Journal*, 21, 1023–1032.

COEY, J. M. (2010). *Magnetism and magnetic materials*. Cambridge University Press.

COWBURN, R. and WELLAND, M. (2000). Room temperature magnetic quantum cellular automata. *Science*, 287, 1466–1468.

DA SILVA, M., SHIMIZU, K., KOBAYASHI, K., SKELDON, P., THOMPSON, G. and WOOD, G. (1995). On the nature of the mechanically polished aluminium surface. *Corrosion science*, 37, 1511–1514.

DONAHUE, M. J. (1999). Oommf user's guide, version 1.0. *-6376*.

ENCINAS-OROPESA, A., DEMAND, M., PIRAUX, L., HUYNEN, I. and EBELS, U. (2001). Dipolar interactions in arrays of nickel nanowires studied by ferromagnetic resonance. *Physical Review B*, 63, 104415.

FERT, A. and PIRAUX, L. (1999). Magnetic nanowires. *Journal of Magnetism and Magnetic Materials*, 200, 338–358.

FORMAN, P. F. (1979). The zygo interferometer system. *Interferometry*. vol. 192, 41–49.

ITAYA, K., SUGAWARA, S., ARAI, K. and SAITO, S. (1984). Properties of porous anodic aluminum oxide films as membranes. *Journal of chemical engineering of Japan*, 17, 514–520.

JESSENSKY, O., MÜLLER, F. and GÖSELE, U. (1998). Self-organized formation of hexagonal pore structures in anodic alumina. *Journal of the Electrochemical Society*, 145, 3735–3740.

LEE, W. and PARK, S.-J. (2014). Porous anodic aluminum oxide : anodization and templated synthesis of functional nanostructures. *Chemical reviews*, 114, 7487–7556.

LI, A., MÜLLER, F., BIRNER, A., NIELSCH, K. and GÖSELE, U. (1998a). Hexagonal pore arrays with a 50–420 nm interpore distance formed by self-organization in anodic alumina. *Journal of applied physics*, 84, 6023–6026.

LI, F., ZHANG, L. and METZGER, R. M. (1998b). On the growth of highly ordered pores in anodized aluminum oxide. *Chemistry of materials*, 10, 2470–2480.

LILLO, M. and LOSIC, D. (2009). Pore opening detection for controlled dissolution of barrier oxide layer and fabrication of nanoporous alumina with through-hole morphology. *Journal of Membrane Science*, 327, 11–17.

MASUDA, H. and FUKUDA, K. (1995). Ordered metal nanohole arrays made by a two-step replication of honeycomb structures of anodic alumina. *science*, 268, 1466–1468.

MOVAHED, M. S. and KHOSRAVI, S. (2010). Level crossing analysis of cosmic microwave background radiation : a method for detecting cosmic strings. *arXiv preprint arXiv :1011.2640*.

NAKAMURA, S., SAITO, M., HUANG, L.-F., MIYAGI, M. and WADA, K. (1992). Infrared optical constants of anodic alumina films with micropore arrays. *Japanese journal of applied physics*, 31, 3589.

NÉEL, L. (1962). Cr hebd. seances acad. sci. 255 1545 nèel l 1962. *CR Hebd. Seances Acad. Sci*, 255, 1676.

NIELSCH, K., CHOI, J., SCHWIRN, K., WEHRSPOHN, R. B. and GÖSELE, U. (2002). Self-ordering regimes of porous alumina : the 10 porosity rule. *Nano letters*, 2, 677–680.

NORDQUIST, K., PENDHARKAR, S., DURLAM, M., RESNICK, D., TEHRANI, S., MANCINI, D., ZHU, T. and SHI, J. (1997). Process development of sub-0.5 μm nonvolatile magnetoresistive random access memory arrays. *Journal of Vacuum Science & Technology B : Microelectronics and Nanometer Structures Processing, Measurement, and Phenomena*, 15, 2274–2278.

OGUCHI, T. (1955). A theory of antiferromagnetism, ii. *Progress of Theoretical Physics*, 13, 148–159.

OSBORN, J. (1945). Demagnetizing factors of the general ellipsoid. *Physical review*, 67, 351.

PENG, Y., CULLIS, T., MÖBUS, G., XU, X. and INKSON, B. (2007). Nanoscale characterization of copt/pt multilayer nanowires. *Nanotechnology*, 18, 485704.

PIRAUX, L., GEORGE, J., DESPRES, J., LEROY, C., FERAIN, E., LEGRAS, R., OUNADJELA, K. and FERT, A. (1994). Giant magnetoresistance in magnetic multilayered nanowires. *Applied Physics Letters*, 65, 2484–2486.

POINERN, G. E. J., ALI, N. and FAWCETT, D. (2011). Progress in nano-engineered anodic aluminum oxide membrane development. *Materials*, 4, 487–526.

RASBAND, W. S. (2011). Imagej, us national institutes of health, bethesda, maryland, usa. *http ://imagej.nih.gov/ij/*.

RICE, S. O. (1944). Mathematical analysis of random noise. *Bell Labs Technical Journal*, 23, 282–332.

SANGPOUR, P., JAFARI, G., AKHAVAN, O., MOSHFEGH, A. and TABAR, M. R. R. (2005). Controlling surface statistical properties using bias voltage : Atomic force microscopy and stochastic analysis. *Physical Review B*, 71, 155423.

SCHÖNENBERGER, C., VAN DER ZANDE, B., FOKKINK, L., HENNY, M., SCHMID, C., KRÜGER, M., BACHTOLD, A., HUBER, R., BIRK, H. and STAUFER, U. (1997). Template synthesis of nanowires in porous polycarbonate membranes : electrochemistry and morphology. *The Journal of Physical Chemistry B*, 101, 5497–5505.

SHINGUBARA, S., MARUO, S., YAMASHITA, T., NAKAO, M. and SHIMIZU, T. (2010). Reduction of pitch of nanohole array by self-organizing anodic oxidation after nanoimprinting. *Microelectronic Engineering*, 87, 1451–1454.

SMART, J. S. (1966). *Effective field theories of magnetism*. No. 2. Saunders.

SMIT, J. and BELJERS, H. (1957). Philips res. rep. 10, 113 (1955). *Google Scholar CAS*.

STĘPNIOWSKI, W. J., NOWAK-STĘPNIOWSKA, A. and BOJAR, Z. (2013). Quantitative arrangement analysis of anodic alumina formed by short anodizations in oxalic acid. *Materials Characterization*, 78, 79–86.

SULKA, G. D. (2008). Highly ordered anodic porous alumina formation by self-organized anodizing. *Nanostructured materials in electrochemistry*, 1, 1–116.

SUN, L., HAO, Y., CHIEN, C.-L. and SEARSON, P. C. (2005). Tuning the properties of magnetic nanowires. *IBM Journal of Research and Development*, 49, 79–102.

TANG, X.-T., WANG, G.-C. and SHIMA, M. (2007). Magnetic layer thickness dependence of magnetization reversal in electrodeposited coni/cu multilayer nanowires. *Journal of magnetism and magnetic materials*, 309, 188–196.

VAHABI, M. and JAFARI, G. (2008). Quantitative analysis of privatization. *arXiv preprint arXiv :0803.2388*.

WEISS, P. (1907). L'hypothèse du champ moléculaire et la propriété ferromagnétique.

WU, H., ZHANG, X. and HEBERT, K. R. (2000). Atomic force microscopy study of the initial stages of anodic oxidation of aluminum in phosphoric acid solution. *Journal of The Electrochemical Society*, 147, 2126–2132.

WU, M., LEU, I.-C. and HON, M.-H. (2002). Effect of polishing pretreatment on the fabrication of ordered nanopore arrays on aluminum foils by anodization. *Journal of Vacuum Science & Technology B : Microelectronics and Nanometer Structures Processing, Measurement, and Phenomena*, 20, 776–782.

YANAGISHITA, T. and MASUDA, H. (2015). High-throughput fabrication process for highly ordered through-hole porous alumina membranes using two-layer anodization. *Electrochimica Acta*, 184, 80–85.

YANG, S., ZHU, H., YU, D., JIN, Z., TANG, S. and DU, Y. (2000). Preparation and magnetic property of fe nanowire array. *Journal of magnetism and magnetic materials*, 222, 97–100.

YAZDIZADEH, M., YELON, A. and MÉNARD, D. (2020). Characterizing and optimizing the electropolishing and pore arrangement in porous anodic aluminum oxide (aao). *Journal of Porous Materials*, 1–8.

YELON, A. (1971). Interactions in multilayer magnetic films. *Physics of Thin films*, Elsevier, vol. 6. 205–300.

ZHANG, L., CHO, H., LI, F., METZGER, R. and DOYLE, W. (1998). Cellular growth of highly ordered porous anodic films on aluminium. *Journal of materials science letters*, 17, 291–294.

APPENDIX A Numerical and simulation source code

Matlab Source Code of ImageProcessing Code

Here we have provide all the codes (the main code and all functions and dependencies) of the image processing code we have developed to quantify the pore ordering in AAO (or any hexagonal pattern). The code can be easily modified in order to be used for other patterns other than hexagonal patterns

Main

```
run('ImagePrepare.m');
global d angles xy d_ave d_std angles_ave angles_std n;
p=FastPeakFind(im,0,[1 5 1;5 20 5;1 5 1],2);
x=p(1:2:end);y=p(2:2:end);xy=[x y];
% z=input('');
% [n,d,angles]=NN6(xy,z);
% zz=input('');
ThresholdFind;
```

Image Preprocessing and preparation

```
% By running this code you can select your SEM image and it will be
% modified to be prepared to be analyzed by the rest of the code. Generally
% this code will produce the complement of the image because we need the
% pores to be white in image (or the maxima of the image) to replace them
% with pixels.
[FileName,PathName] = uigetfile({'*.png';'*.*'},'Select the SEM Image in .PNG
format');
Path=strcat(PathName,FileName);
imorig=importdata(Path);
im=imcomplement(rgb2gray(imorig));

%im=imgaussfilt(im);
```

Fast Peak Finder

```
function  [cent, varargout]=FastPeakFind(d, thres, filt ,edg, res, fid)
% Analyze noisy 2D images and find peaks using local maxima (1 pixel
% resolution) or weighted centroids (sub-pixel resolution).
% The code is designed to be as fast as possible, so I kept it pretty basic.
% The code assumes that the peaks are relatively sparse, test whether there
% is too much pile up and set threshold or user defined filter accordingly.
%
% How the code works:
% In theory, each peak is a smooth point spread function (SPF), like a
% Gaussian of some size, etc. In reality, there is always noise, such as
%"salt and pepper" noise, which typically has a 1 pixel variation.
% Because the peak's PSF is assumed to be larger than 1 pixel, the "true"
% local maximum of that PSF can be obtained if we can get rid of these
% single pixel noise variations. There comes medfilt2, which is a 2D median
% filter that gets rid of "salt and pepper" noise. Next we "smooth" the
% image using conv2, so that with high probability there will be only one
% pixel in each peak that will correspond to the "true" PSF local maximum.
% The weighted centroid approach uses the same image processing, with the
% difference that it just calculated the weighted centroid of each
% connected object that was obtained following the image processing.  While
% this gives sub-pixel resolution, it can miss peaks that are very close to
% each other, and runs slightly slower. Read more about how to treat these
% cases in the relevant code commentes.
%
% Inputs:
% d     The 2D data raw image - assumes a Double\Single-precision
%       floating-point, uint8 or unit16 array. Please note that the code
%       casts the raw image to uint16 if needed.  If the image dynamic range
%       is between 0 and 1, I multiplied to fit uint16. This might not be
%       optimal for generic use, so modify according to your needs.
% thres A number between 0 and max(raw_image(:)) to remove  background
% filt  A filter matrix used to smooth the image. The filter size
%       should correspond the characteristic size of the peaks
% edg   A number>1 for skipping the first few and the last few 'edge' pixels
% res   A handle that switches between two peak finding methods:
```

```
%       1 - the local maxima method (default).
%       2 - the weighted centroid sub-pixel resolution method.
%       Note that the latter method takes ~20% more time on average.
% fid   In case the user would like to save the peak positions to a file,
%       the code assumes a "fid = fopen([filename], 'w+');" line in the
%       script that uses this function.
%
%Optional Outputs:
% cent        a 1xN vector of coordinates of peaks (x1,y1,x2,y2,...
% [cent cm]   in addition to cent, cm is a binary matrix  of size(d)
%             with 1's for peak positions. (not supported in the
%             the weighted centroid sub-pixel resolution method)
%
%Example:
%
%   p=FastPeakFind(image);
%   imagesc(image); hold on
%   plot(p(1:2:end),p(2:2:end),'r+')
%
%   Adi Natan (natan@stanford.edu)
%   Ver 1.7 , Date: Oct 10th 2013
%
%% defaults
if (nargin < 1)
    d=uint16(conv2(reshape(single( 2^14*(rand(1,1024*1024)>0.99995) ),[1024 1024])
,fspecial('gaussian', 15,3),'same')+2^8*rand(1024));
    imagesc(d);
end

if ndims(d)>2 %I added this in case one uses imread (JPG\PNG\...).
    d=uint16(rgb2gray(d));
end

if isfloat(d) %For the case the input image is double, casting to uint16 keeps
enough dynamic range while speeds up the code.
    if max(d(:))<=1
```

```
        d =  uint16( d.*2^16./(max(d(:))));
    else
        d = uint16(d);
    end
end

if (nargin < 2)
    thres = (max([min(max(d,[],1))  min(max(d,[],2))])) ;
end

if (nargin < 3)
    filt = (fspecial('gaussian', 7,1)); %if needed modify the filter according
to the expected peaks sizes
end

if (nargin < 4)
    edg =3;
end

if (nargin < 5)
    res = 1;
end

if (nargin < 6)
    savefileflag = false;
else
    savefileflag = true;
end

%% Analyze image
if any(d(:))  ; %for the case of non zero raw image

    d = medfilt2(d,[3,3]);

    % apply threshold
    if isa(d,'uint8')
```

```
        d=d.*uint8(d>thres);
    else
        d=d.*uint16(d>thres);
    end

    if any(d(:))   ; %for the case of the image is still non zero

        % smooth image
        d=conv2(single(d),filt,'same') ;

        % Apply again threshold (and change if needed according to SNR)
        d=d.*(d>0.9*thres);

        switch res % switch between local maxima and sub-pixel methods

            case 1 % peak find - using the local maxima approach - 1 pixel resolution

                % d will be noisy on the edges, and also local maxima looks
                % for nearest neighbors so edge must be at least 1. We'll skip
'edge' pixels.
                sd=size(d);
                [x y]=find(d(edg:sd(1)-edg,edg:sd(2)-edg));

                % initialize outputs
                cent=[];%
                cent_map=zeros(sd);

                x=x+edg-1;
                y=y+edg-1;
                for j=1:length(y)
                    if (d(x(j),y(j))>=d(x(j)-1,y(j)-1 )) &&...
                            (d(x(j),y(j))>d(x(j)-1,y(j))) &&...
                            (d(x(j),y(j))>=d(x(j)-1,y(j)+1)) &&...
                            (d(x(j),y(j))>d(x(j),y(j)-1)) && ...
                            (d(x(j),y(j))>d(x(j),y(j)+1)) && ...
                            (d(x(j),y(j))>=d(x(j)+1,y(j)-1)) && ...
```

```
                            (d(x(j),y(j))>d(x(j)+1,y(j))) && ...
                            (d(x(j),y(j))>=d(x(j)+1,y(j)+1));

                        %All these alternatives were slower...
                        %if all(reshape( d(x(j),y(j))>=d(x(j)-1:x(j)+1,y(j)-1:y(j)+1),9,
                        %if  d(x(j),y(j)) == max(max(d((x(j)-1):(x(j)+1),(y(j)-
1):(y(j)+1))))
                        %if  d(x(j),y(j))  == max(reshape(d(x(j),y(j))  >=  d(x(j)-
1:x(j)+1,y(j)-1:y(j)+1),9,1))

                        cent = [cent ;  y(j) ; x(j)];
                        cent_map(x(j),y(j))=cent_map(x(j),y(j))+1; % if a binary
matrix output is desired

                    end
                end

            case 2 % find weighted centroids of processed image,  sub-pixel resolution.
                   % no edg requirement needed.

                % get peaks areas and centroids
                stats = regionprops(logical(d),d,'Area','WeightedCentroid');

                % find reliable peaks by considering only peaks with an area
                % below some limit. The weighted centroid method can be not
                % accurate if peaks are very close to one another, i.e., a
                % single peak will be detected, instead of the real number
                % of peaks. This will result in a much larger area for that
                % peak. At the moment, the code ignores that peak. If that
                % happens often consider a different threshold, or return to
                % the more robust "local maxima" method.
                % To set a proper limit, inspect your data with:
                % hist([stats.Area],min([stats.Area]):max([stats.Area]));
                % to see if the limit I used (mean+2 standard deviations)
                % is an appropriate limit for your data.
```

```
                rel_peaks_vec=[stats.Area]<=mean([stats.Area])+2*std([stats.Area]);
                cent=[stats(rel_peaks_vec).WeightedCentroid]';
                cent_map=[];

        end

        if savefileflag
            % previous version used dlmwrite, which can be slower than  fprinf
            %             dlmwrite([filename '.txt'],[cent],   '-append', ...
            %                 'roffset', 0,   'delimiter', '\t', 'newline', 'unix');+

            fprintf(fid, '%f ', cent(:));
            fprintf(fid, '\n');

        end


    else % in case image after threshold is all zeros
        cent=[];
        cent_map=zeros(size(d));
        if nargout>1 ;  varargout{1}=cent_map; end
        return
    end

else % in case raw image is all zeros (dead event)
    cent=[];
    cent_map=zeros(size(d));
    if nargout>1 ;  varargout{1}=cent_map; end
    return
end

%demo mode - no input to the function
if (nargin < 1); colormap(bone);hold on; plot(cent(1:2:end),cent(2:2:end),'rs');hold
off; end

% return binary mask of centroid positions if asked for
```

```
if nargout>1 ;  varargout{1}=cent_map; end
```

Applying Avg Filtering

```
clc;
clear all;
close all;

a=imread('cameraman.tif');
figure, imshow(a)
an=imnoise(a,'gaussian');
[m,n]=size(an);
figure, imshow(uint8(an))
b=input('Enter Averaging Mask size: ');
z=ones(b);
[p,q]=size(z);


w=1:p;
x=round(median(w));
anz=zeros(m+2*(x-1),n+2*(x-1));

for i=x:(m+(x-1))
    for j=x:(n+(x-1))
        anz(i,j)=an(i-(x-1),j-(x-1));
    end
end
figure, imshow(uint8(anz))

sum=0;
x=0;
y=0;
for i=1:m
    for j=1:n
        for k=1:p
            for l=1:q
                sum= sum+anz(i+x,j+y)*z(k,l);
```

```
                y=y+1;
            end
            y=0;
            x=x+1;
        end
        x=0;
        ans(i,j)=(1/(p*q))*(sum);
        sum=0;
    end
end
figure, imshow(uint8(ans))
```

Checking if the pattern is Hexagonal

```
function r=IsHexa( i )
%UNTITLED3 Summary of this function goes here
%   Detailed explanation goes here
global xy angles_ave angles_std d_ave d_std ;
[n,d,angles]=NN6(xy,[xy(i,1),xy(i,2)]);
d_min=d_ave-d_std;
d_max=d_ave+d_std;
a_min=angles_ave-angles_std;
a_max=angles_ave+angles_std;
    if ( (any(d>d_max)) || (any(d<d_min)) || (any(angles>a_max)) || (any(angles<a_min))
)
        r=0;
    else
        r=1;
    end
end
```

Find the 6 neighbours of each pore

```
function [ nodes,distance,angles ] = NN6( xy,z )
%NN6 is a function which find the 6 nearest neighbors of a given set of
%points
%   inputs:
```

```
%   z           is a point which has the format of (x,y) as its coordinates
%   Outputs:
%   nodes       is a 1by6 matrix where (x(nodes),y(nodes)) shows the coordinates
%               of the 6 nearest neighbors with respect to the given point z
%   distance    is a 1by6 matrix which shows the euclidean distance of each neighbor
with respect to
%               the given point z
%   angels      is a 1by6 matrix which returns the angle between the given
%               point z with respect to its 6 neighbors. If we lable the
%               neares neighbors in a counterclockwise movement and
%               consider the first point above the x axise and in the first
%               quarter of the coordinates(manzuram ine ke avalin noghte ee
%               ke balaye mehvare x va samte raast gharar migire) as no.1
%               then the first number in matrix angels is the angle between
%               points 1z2 and the second number is the angel between 2z3
%               and so on.

angles=0;
[nodes,distance]=knnsearch(xy,z,'k',7);
% nodes=nodes(2:end);
distance=distance(2:end);
neighbors=xy(nodes(2:end),:);
ref=[10,0];
bordar=neighbors-z;

angles(1)=acos(dot(bordar(1,:),ref)/(norm(bordar(1,:)).*norm(ref)));
if (bordar(1,2)<0)
    angles(1)=-angles(1);
end
angles(2)=acos(dot(bordar(2,:),ref)/(norm(bordar(2,:)).*norm(ref)));
if (bordar(2,2)<0)
    angles(2)=-angles(2);
end
angles(3)=acos(dot(bordar(3,:),ref)/(norm(bordar(3,:)).*norm(ref)));
if (bordar(3,2)<0)
    angles(3)=-angles(3);
```

```
end
angles(4)=acos(dot(bordar(4,:),ref)/(norm(bordar(4,:)).*norm(ref)));
if (bordar(4,2)<0)
    angles(4)=-angles(4);
end
angles(5)=acos(dot(bordar(5,:),ref)/(norm(bordar(5,:)).*norm(ref)));
if (bordar(5,2)<0)
    angles(5)=-angles(5);
end
angles(6)=acos(dot(bordar(6,:),ref)/(norm(bordar(6,:)).*norm(ref)));
if (bordar(6,2)<0)
    angles(6)=-angles(6);
end
angles=rad2deg(angles);

for i=1:6
    if (angles(i)<0)
        angles(i)=360+angles(i);
    end
end
angles=sort(angles);
atemp=angles(1);

angles(1)=angles(2)-angles(1);
if (angles(1)<0)
    angles(1)=360+angles(1);
end
angles(2)=angles(3)-angles(2);
if (angles(2)<0)
    angles(2)=360+angles(2);
end
angles(3)=angles(4)-angles(3);
if (angles(3)<0)
    angles(3)=360+angles(3);
end
angles(4)=angles(5)-angles(4);
```

```
if (angles(4)<0)
    angles(4)=360+angles(4);
end
angles(5)=angles(6)-angles(5);
if (angles(5)<0)
    angles(5)=360+angles(5);
end
angles(6)=atemp-angles(6);
if (angles(6)<0)
    angles(6)=360+angles(6);
end

end
```

Decide to what extend we consider the pattern as ordered

```
function ThresholdFind
global  d angles xy d_ave d_std angles_ave angles_std n x y;

s=size(xy);
s=s(1);
r=round(rand(1,100).*s);
n=zeros(100,7);
d=zeros(100,6);
angles=zeros(100,6);
for i=1:100
    [n(i,:),d(i,:),angles(i,:)]=NN6(xy,[xy(r(i),1),xy(r(i),2)]);
end
d_ave=mean(d);
d_std=std(d);
angles_ave=mean(angles);
angles_std=std(angles);
```

Level Crossing Analysis

Main

```
% In this code the following steps will be done in order to create a sequence
of random numbers with a desired correlation and evaluate the LevelCrossing
% Method to quantitatively measure the roughness of a surface (in our case the
surface is gonna be the electropolished aluminum)
% 1- by entering the l(Length of array), c(the correlation of the first lag),
m(the mean value of the array) and v(the variance of the array) we generate the
simulated surface
% 2- we then determine the LevelCrossing result of the data created in first step
% 3- we draw the results in step 2
% 4- we shuffle the data created in step 1 to show that the difference between
roughness of a correlated sequence, uncorrelated sequence AND a white noise sequence
(shuffled)
% The point is showing the potential of this method to evaluate the roughness
of the surface (quantitatively). We already now that a correlated surface is smoother
than a random surface which is also smoother than an uncorrelated surface


clear all
%close all


% Here we simulate the syrface roughness by creating either Correlcated or
% AntiCorrelated randome numbers. In Case we want to measure the surface
% roughness of real sample we can chenge this section to comment
%% Simulating the surface roughness

% l=input('Enter the Length of the array (surface sample) you want to simulate,
a typical number is 100000? ');
% c=input('Enter the correlation value you want to generate, +0.99 is highly correlated
and -0.99 is highly uncorrelated');
% m=input('The mean value of your array (recommended is 0 in order to ease the
next steps calculation without lossing generality)');
% v=input('The variance of your array, The higher the variance the larger the
```

```
roughness teeth, the smaller the variance the shorter the roughness teeth');
% y1=gencorr(l,c,m,v);


%% Real surface roughness data
% This part is temporarely comments, In Case of examining real sample this
% section should become uncomment and the above section should become
% comment

[FileName,PathName] = uigetfile({'*.txt';'*.*'},'Select the AFM result');
Path=strcat(PathName,FileName);
y1=importdata(Path);
y1_min=min(y1);y1_max=max(y1);y1_lim=y1_max-y1_min;
y1=2*(y1-y1_min)/y1_lim-1;
%%
y2=shuffle(y1);
size_data=size(y1);
size_data2=size(y2);

[x1,lc1]=DistLC2(y1);
[x2,lc2]=DistLC2(y2);

[Width_half_Max_x1_lc1,Width_e2_Max_x1_lc1]=findwidth(x1,lc1);
[Width_half_Max_x2_lc2,Width_e2_Max_x2_lc2]=findwidth(x2,lc2);
max_lc1=max(lc1);
max_lc2=max(lc2);
Rgh_max_to_max=max_lc2/max_lc1;
GF_lc1=fit(x1',(lc1-min(lc1))','gauss1'); %gaussian fit of the level crossing
result
GF_lc2=fit(x2',(lc2-min(lc2))','gauss1');
Rgh_NTotlShfld_dived_NTotl=GF_lc2.a1*GF_lc2.c1*sqrt(pi)/(GF_lc1.a1*GF_lc1.c1*sqrt(pi));
%total number of shuffles LC divided by total number of the original data LV as
measure of roughness(i. e. area under the gaussian fit)
Rgh_NTotl_dived_size=GF_lc1.a1*GF_lc1.c1*sqrt(pi)/length(y1);
Rgh_NTotl=GF_lc1.a1*GF_lc1.c1*sqrt(pi);
Roughness_shuffle=GF_lc2.a1*GF_lc2.c1*sqrt(pi)/length(y1);
```

```
newFileName=strrep(FileName,'.txt','');
res=strcat('C:\Users\Lab Magnétisme\Dropbox\PhD\MatlabProjects\LevelCrossing\PrepareData
res2=strcat('C:\Users\Lab Magnétisme\Dropbox\PhD\MatlabProjects\LevelCrossing\PrepareDat
%clearvars -except res2 res max_lc1 max_lc2 Rough_value_lc1 Rough_value_lc2 x1
x2 lc1 lc2 Width_half_Max_x1_lc1 Width_e2_Max_x1_lc1 Width_half_Max_x2_lc2 Width_e2_Max_
plot(x1(1:15:length(x1)),lc1(1:15:length(lc1))-min(lc1),'o','color',[.35 .35 .75],'LineW
hold on
%plot(x2,lc2-min(lc2),'color',[0 .75 0]);
plot(GF_lc1,'.r');legend('LC data','Gaussian Fit');
strNtotl=['N_t_o_t^+(0)=',num2str(round(Rgh_NTotl))];
text(-.9,max(lc1)*.6,strNtotl,'FontSize',12,'FontWeight','bold');
xlabel('\alpha','FontSize',16,'FontWeight','bold');
ylabel('LC','FontSize',16,'FontWeight','bold');
print(newFileName,'-dpng');
%plot(GF_lc2,'b');
savefig(res2)
save(res)
%hold off
```

Function Cross N ND

```
%% this function takes two variable:-
%    x: vector of real values
%    L: Level of crossing
% this function returns two variables:-
%    CN_ND: crossing number in negative direction
%    CNV  : vector denoting the location of xrossing at negative direction

function  [CN_ND, CNV]= Cross_N_ND(x,L)
b=double((x<L));
c=b;
for k=1:length(b)-1

    if b(k)==1 && b(k+1)==1
       c(k+1)=0;
    end
end
```

```
%temp begin\------------------------------

bb=double((x>L));
cc=bb;
for k=1:length(bb)-1

    if bb(k)==1 && bb(k+1)==1
       cc(k+1)=0;
    end
end


%temp End\--------------------------------
c_sum=(sum(c)+sum(cc));


CN_ND=c_sum;
CNV=c;
```

Function Shuffle

```
function [s,myorder]=shuffle(x,varargin)
%SHUFFLE    Shuffles vectors or matrices.
%   SHUFFLE(X) shuffles the elements of a vector or matrix X.
%
%   SHUFFLE(X,DIM) shuffles along the dimension DIM.
%
%   [Y,I] = SHUFFLE(X) also returns an index matrix I. If X is
%   a vector, then Y = X(I). If X is an m-by-n matrix, then
%       for j = 1:n, Y(:,j) = X(I(:,j),j); end
%
%   Input arguments:
%      X - the vector or matrix to shuffle (array)
%      DIM - the dimension along which to shuffle (integer)
%   Output arguments:
%      Y - the vector or matrix with the elements shuffled (array)
```

```
%      I - the index matrix with the shuffle order (array)
%
%   Examples:
%      X = [10 25 30 40]
%      [Y,I] = SHUFFLE(X)
%      Y = 30    25    10    40
%      I =  3     2     1     4
%
%      X = [10 25 ; 3.2 4.1 ; 102 600]
%      [Y,I] = SHUFFLE(X)
%      Y =   3.2000  600.0000
%           10.0000   25.0000
%          102.0000    4.1000
%      I =  2     3
%           1     1
%           3     2
%
%      X = [10 25 50 ; 3.2 4.1 5.5 ; 102 600 455 ; 0.03 0.34 0.01]
%      DIM = 1
%      [Y,I] = SHUFFLE(X,DIM)
%      Y =  10.0000   25.0000   50.0000
%            0.0300    0.3400    0.0100
%          102.0000  600.0000  455.0000
%            3.2000    4.1000    5.5000
%      I =  1     4     3     2
%
%      X = [10 25 50 ; 3.2 4.1 5.5 ; 102 600 455 ; 0.03 0.34 0.01]
%      DIM = 2
%      [Y,I] = SHUFFLE(X,DIM)
%      Y =  10.0000   50.0000   25.0000
%            3.2000    5.5000    4.1000
%          102.0000  455.0000  600.0000
%            0.0300    0.0100    0.3400
%      I =  1     3     2
%
%   See also ORDERBY
```

```
%
%   Created: Sara Silva (sara@itqb.unl.pt) - 2002.11.02

rand('state',sum(100*clock)); % (see help RAND)

switch nargin
case 1
   if size(x,1)==1 | size(x,2)==1
      [ans,myorder]=sort(rand(1,length(x)));
      s=x(myorder);
   else
      [ans,myorder]=sort(rand(size(x,1),size(x,2)));
    for c=1:size(x,2)
       s(:,c)=x(myorder(:,c),c);
      end
   end
case 2
   d=varargin{1};
   switch d
   case 1
      [ans,myorder]=sort(rand(1,size(x,1)));
s=x(myorder,:);
   case 2
      [ans,myorder]=sort(rand(1,size(x,2)));
      s=x(:,myorder);
   otherwise
      error('SHUFFLE: Unknown command option.')
   end
end
```

OOMMF parent source code of most simulations

In this section we provided the source code of OOMMF we have used for simulating most of our simulations in this projects. The user should change the parameters due to their own desired structures. In order to define different geometrical structures, you can create a visual

file with various colors and then refer to the images in your code and assign each color to a specific material. For example Red is Ni , Blue is Copeer and so on. The thickness and the number of layers will be defined in the .mif source code. For further assistance please see the OOMMF documents in their website. This code was also adopted from on of the provided samples and then modified in order to be used for our own purposes.

```
# MIF 2.1
# MIF Example File: diskarray.mif
# Description: Example file using an Oxs_ScriptAtlas to define an array
#  of disks.
#
set pi [expr {4*atan(1.0)}]
set mu0 [expr {4*$pi*1e-7}]

RandomSeed 1

Parameter cellsize        10    ;# Discretization cell size, in nm
Parameter thickness      20    ;# Film thickness, in nm

Parameter disk_diameter  50    ;# Dimension of disks, in nm
Parameter disk_spacing   75    ;# Spacing between disk centers
Parameter disk_xcount     5    ;# Number of disks in x-direction
Parameter disk_ycount     3    ;# Number of disks in y-direction

# Convert parameter dimensions from nm to m
set cellsize      [expr {$cellsize*1e-9}]
set thickness     [expr {$thickness*1e-9}]
set disk_diameter [expr {$disk_diameter*1e-9}]
set disk_spacing  [expr {$disk_spacing*1e-9}]

set xrange [expr {($disk_xcount-1)*$disk_spacing+$disk_diameter}]
set yrange [expr {($disk_ycount-1)*$disk_spacing+$disk_diameter}]
set zrange $thickness

# Proc that assigns raw point coordinates to regions.  There
# are 3 regions.  Region 0 is the encompassing matrix/universe.
# Regions 1 and 2 form a checkerboard pattern on the array of
```

```
# disks, with the disk in the lower lefthand corner being in
# region 1.
proc DiskRegion {x y z} {
   global disk_diameter disk_spacing
   set rx [expr {fmod($x,$disk_spacing) - $disk_diameter/2.}]
   set ry [expr {fmod($y,$disk_spacing) - $disk_diameter/2.}]
   if {$rx*$rx+$ry*$ry>$disk_diameter*$disk_diameter/4.} {
      return 0;
   }
   set xindex [expr {int(floor($x/$disk_spacing))}]
   set yindex [expr {int(floor($y/$disk_spacing))}]
   return [expr {1+($xindex+$yindex)%2}]
}

proc VortexInit { x y z } {
   global disk_diameter disk_spacing

   set coresize 0.5

   # Compute position relative to center point of nearest disk
   set rx [expr {2*fmod($x,$disk_spacing)/$disk_diameter - 1.}]
   set ry [expr {2*fmod($y,$disk_spacing)/$disk_diameter - 1.}]

   # Compute mz component
   set rsq [expr {$rx*$rx+$ry*$ry}]
   if {$rsq>=$coresize*$coresize} {
      set mz 0.0
   } else {
      set rn [expr {sqrt($rsq)/$coresize}]
      set mz [expr {(2.*$rn-3.)*$rn*$rn+1}]
   }

   # Compute checkboard code, to determint chirality
   set xindex [expr {int(floor($x/$disk_spacing))}]
   set yindex [expr {int(floor($y/$disk_spacing))}]
   set chiral [expr {2*(($xindex+$yindex)%2)-1}]
```

```
   # Compute mx, my
   set scale [expr {sqrt((1.0-$mz*$mz)/$rsq)}]
   set mx [expr {$chiral*$ry*$scale}]
   set my [expr {-1*$chiral*$rx*$scale}]

   return [list $mx $my $mz]
}

# Atlas
Specify Oxs_ScriptAtlas:atlas [subst {
   xrange {0 $xrange}
   yrange {0 $yrange}
   zrange {0 $zrange}
   regions { Adisks Bdisks }
   script  DiskRegion
   script_args rawpt
}]


Specify Oxs_RectangularMesh:mesh [subst {
  cellsize {$cellsize $cellsize $cellsize}
  atlas :atlas
}]

Specify Oxs_UniaxialAnisotropy {
   K1  { Oxs_AtlasScalarField {
      atlas :atlas
      default_value 0
      values {
         Adisks 520e3
         Bdisks 520e3
      }
   }}
   axis { Oxs_AtlasVectorField {
      atlas :atlas
```

```
      default_value {0 0 1}
      values {
         Adisks {1 0 0}
         Bdisks {0 1 0}
      }
   }}
}

# Exchange is automatically 0 in regions where Ms = 0.0.  See definition
# of Ms in the Oxs_MinDriver Specify block.
Specify Oxs_UniformExchange {
  A  13e-12
}

Specify Oxs_UZeeman [subst {
  multiplier [expr {0.001/$mu0}]
  Hrange {
     {0    0 0    1000  0 0    1000}
     {1000 0 0    -800  0 0    1800}
     {-800 0 0    1000  0 0    1800}
     {1000 0 0    -700  0 0    1700}
     {-700 0 0    1000  0 0    1700}
     {1000 0 0    -600  0 0    1600}
     {-600 0 0    1000  0 0    1600}
     {1000 0 0    -500  0 0    1500}
     {-500 0 0    1000  0 0    1500}
     {1000 0 0    -400  0 0    1400}
     {-400 0 0    1000  0 0    1400}
  }
}]

Specify Oxs_Demag {}

Specify Oxs_CGEvolve {}

Specify Oxs_MinDriver {
```

```
basename diskarray
evolver Oxs_CGEvolve
stopping_mxHxm 1
mesh :mesh
Ms { Oxs_AtlasScalarField {
   atlas :atlas
   default_value 0.0
   values {
      Adisks 1400e3
      Bdisks { Oxs_RandomScalarField {
           range_min 600e3
           range_max 800e3
      }}
   }
}}
m0 { Oxs_ScriptVectorField {
   atlas :atlas
   script VortexInit
   script_args rawpt
   norm 1.0
}}
comment {m0 { Oxs_AtlasVectorField {
   atlas :atlas
   default_value {0 0 1}
   values {
        Adisks { Oxs_RandomVectorField {
             min_norm 1.0
             max_norm 1.0
        }}
        Bdisks {0 1 0}
   }
}}}
comment {m0 { Oxs_RandomVectorField {
   min_norm 1.0
   max_norm 1.0
}}}}
```